

THE ADVANCED CONTROL OF TRIBOELECTRICALLY CHARGED FUEL
USING ELECTRIC FIELDS UNDER HIGH PRESSURE

by

Alzarrio Rolle

A thesis submitted to the faculty of
The University of North Carolina at Charlotte
in partial fulfillment of the requirements
for the degree of Master of Science in
Applied Energy and Electromechanical Systems

Charlotte

2017

Approved by:

Dr. Maciej A. Noras

Dr. Wesley Williams

Dr. Mesbah Uddin

ABSTRACT

ALZARRIO ROLLE. The Advanced Control of Triboelectrically Charged Fuel Using Electric Fields Under High Pressure (Under the direction of DR. MACIEJ A. NORAS)

This research provides preliminary results of electrospraying in elevated surrounding pressures of 40, 50 and 60 psi. Investigations were correspondingly detailed regarding the process of designing and acquiring a manufactured custom pressure chamber for experimental analysis. SolidWorks was used to model and simulate multiple design iterations based on Finite Element Analysis (FEA) and manufacturability cost. The pressure vessel has an internal diameter of 5.50” with a length of 22.5”, a top lid capable of detaching from the body with five ¼” NPT treaded holes and a 1” NPT plug with a 0.52” thru hole counter sunk 0.600” at a depth of 0.58”. The working pressure of this chamber is 3 MPa (435 psi) at a temperature of 300°F (149°C).

The fuel system transporting 87 octane ascertained results of 0.034, 0.035 and 0.038 for the average mass per injection of the corresponding pressures at 40, 50 and 60 psi respectively. The R-squared values were 0.992, 0.9943 and 0.9961 with 40 psi as the bottommost value and 60 psi at the utmost value. The average net charge density values per injection were 1.265, 1.286 and 1.368 along with the standard deviations of 0.019, 0.004 and 0.004 for the consequent pressures of 40, 50 and 60 psi were calculated respectively. From this data, the experiments conducted at 60 psi ascertained both the maximum prevailing accumulation of mass as well as the greatest net electric charge density.

The COMSOL Multiphysics simulations produced a particle diameter distribution of values with a large concentration between 9.5 and 11 μm . Whereas, the Rayleigh limit

distribution for the charge on a droplet values were commonly between 1.2 and 1.6×10^{-13} C. A contraction on the particle trajectories were observed when all three pressures were compared without an electric field and with the presence of a 10kV electric field. The tightening of the particle trajectories were intensified when the electric field was amplified to 20kV. However, there appears to be no substantial change between the pressure of 40, 50 and 60 psi when compared to simulations executed at atmospheric pressure.

ACKNOWLEDGMENTS

I would like to take the opportunity to thank the Graduate school as well as the William States Lee College of Engineering at the University of North Carolina at Charlotte for admission into the Applied Energy and Electromechanical Systems program. I would also like to thank the Engineering Technology Department for providing funding and other resources for me to construct a test setup. I wish to thank Dr. Maciej A. Noras for giving me an opportunity to continue the existing research. Without his continued persistence, dedication and constant encouragement, this research would not have reached this milestone.

My sincere thanks to my committee member Dr. Wesley Williams for his constant advice in a wide range of engineering and professional topics as well as, all of the numerous years of guidance and inspiration which had begun from the inception of my undergraduate studies. His mentorship throughout my years of studies has played a pivotal role in my achievement and success, for which I am evermore grateful.

I would like to thank Dr. Mesbah Uddin for participating on my thesis committee and providing his knowledge on Computational Fluid Dynamics (CFD) along with fluid flow simulation and analysis in numerous computer programs. I would also like to thank Professor Daniel Hoch for the verification of some very preliminary initial volume and thermodynamic calculations for a starting point with the size of the pressure chamber design.

I wish to thank Mr. Richard Graley for providing several power supplies, wire and cables as well as electrical components and other miscellaneous equipment. I am thankful

to Mr. Parks Davidson for granting me access to the stress lab to make use of the hood with a blower while conducting experiments of gasoline.

I am very appreciative to Ms. Crystal Green for all she has done by issuing course permits as well as mediating along with ordering approved equipment for the fuel system and constant communications regarding the manufactured pressure chamber. I am grateful to Mr. Cornell Constantinidis at Fabrication Associates Incorporated for his continuous patience and willingness to work with me on the final design of the pressure chamber before the delivery of the final product.

I would like to thank Robert Logan Garris for all his previous hard work on this research and sharing all of his information with me which in turn gave me an excellent starting point and made my research abundantly easier and time efficient. I would like to thank the recent UNCC Graduates Brett Cockerham and Andy Gould who are now employees at Schweitzer Engineering Laboratories (SEL) for their help in setting up, communicating and programming SEL products.

My thanks to Kirtan Davda, Luis Benitez-Peralta, Ashtosh Phatak and Ansovinus Akumawah whom I shared a research lab and workspace with. They all were available at any time to answer any questions or concerns I expressed.

Last but not least, I would like to thank Gissella and Ivan Cabrera along with their entire family as well as my friends and family for all of their support, especially my parents for their unrelenting assistance both emotionally and financially.

Table of Contents

LIST OF TABLES	x
LIST OF FIGURES	xi
CHAPTER 1: INTRODUCTION	1
CHAPTER 2: LITERATURE REVIEW	7
2.1 Basics Overview of an Internal Combustion Engine	8
2.2 Fuel Injection System.....	14
2.3 Electro spraying and Triboelectric Charging Technology	19
2.4 Pressure Chamber Development	31
2.5 Previous Research by Logan Garris	45
CHAPTER 3: METHODOLOGY	51
3.1 Entire System Overview.....	51
3.2 Pressure Chamber Design	53
3.2.1 Parr Instruments Design.....	54
3.2.2 Australian Maritime College Design	58
3.2.3 Sight Glass Design.....	62
3.2.4 Cylindrical Design	66
3.2.5 North Carolina Administrative Code	69
3.2.6 Final Pressure Chamber Design.....	71
3.3 Fuel Injection System.....	79

3.3.1	Fuel Injectors	80
3.3.2	SEL PLC	82
3.4	Existing Pressure Vessel Assembled Test Setup.....	85
CHAPTER 4: RESULTS		87
4.1	Experimental Results.....	87
4.1.1	Dielectric Fluid Mass Evaluation.....	87
4.1.2	Dielectric Fluid Charge Spray Analysis	90
4.2	Simulation Results.....	93
4.2.1	COMSOL Multiphysics Simulations at 10kV	93
4.2.2	COMSOL Multiphysics Simulations at 20kV	99
CHAPTER 5: CONCLUSIONS		103
5.1	Discussion	103
5.2	Potential Future Work	105
BIBLIOGRAPHY		107
APPENDIX A: PARR INSTRUMENT COMPANY QUOTE		110
APPENDIX B: SOLIDWORKS DRAWINGS FOR PRESSURE CHAMBER DESIGN		111
APPENDIX C: FUEL SYSTEM BILL OF MATERIALS		116
APPENDIX D: DIMENSIONED DRAWING FOR EV 14 LONG FUEL INJECTOR.....		117

APPENDIX E: FINANCIAL QUOTE FROM FABRICATION ASSOCIATES INC.....	118
APPENDIX F: CERTIFIED DRAWING OF THE PRESSURE CHAMBER	119
APPENDIX G: RAW MASS DATA FOR SPRAYING EXPERIMENTS IN GRAMS	120
APPENDIX H: CALCULATED VOLUME DATA FOR SPRAYING EXPERIMENTS IN KILOGRAM PER CUBIC METER.....	121
APPENDIX I: RAW ELECTRICAL CHARGE DATA FOR EACH SPRAY IN [nC]	122
APPENDIX J: COMSOL MULTIPHYSICS PARAMETERS FOR MODEL DISTRIBUTIONS AND PARTICLE TRAJECTIONS	123
APPENDIX K: PRESSURE CHAMBER AND RELATED EQUIPMENT BILL OF MATERIALS.....	124

LIST OF TABLES

Table 1: SEL-2411 Pickup Time Results.....	84
Table 2: Average Mass per injector shot for 40, 50 and 60 psi	87
Table 3: Calculated Average Volume per injector shot for 40, 50 and 60 psi.....	89
Table 4: Average Net Charge Density values per injector for 40, 50 and 60 psi	90
Table 5: List of Bill of Materials for the fuel injection system	116
Table 6: Spray Mass for 40, 50 and 60 psi	120
Table 7: Calculated Spray Volume for 40, 50 and 60 psi.....	121
Table 8: Electric Charge Values for 40, 50 and 60 psi	122
Table 9: COMSOL Multiphysics model parameter definitions.....	123
Table 10: List of Remaining Bill of Materials for the Pressure Chamber	124

LIST OF FIGURES

Figure 1: Visual illustration of each phrase for a 4-stroke spark ignition engine [1]	8
Figure 2: Octane number and boiling point relationship for hydrocarbons [2]	11
Figure 3: Start Of Injection (SOI) for different fuel quantities with Mass Burn Fraction (MBF) variations at Fuel Injection Pressure (FIP) of 500 bars [3].....	12
Figure 4: Illustration of a common high pressure rail system[4].....	14
Figure 5: Diagram representation of a constant volume combustion chamber system [5].....	16
Figure 6: Diagram schematic of different nozzles for the experimentation (a) single-hole (b) multi-hole [6]	17
Figure 7: Schematic illustration of bi-component equipment setup for electrospaying [7].....	19
Figure 8: Electro spray system schematic [8]	21
Figure 9: Illustration of electrode generalized geometry with spray dispersion representation [9]	22
Figure 10: (a) Sharpened tip of silica tube (b) Electrode grounded needle made of silica with a stainless steel plate located between 3 and 5 mm away (c) Deionized water in a steady cone-jet [10].....	23
Figure 11: Contact prints of magnified collected droplets samples with a tick marking representing 200 micrometers [11]	24
Figure 12: Fabrication of Nanofiber and Nanoparticles while (A) Electrospinning and (B) Electrospaying [12]	25
Figure 13: (a) Stern model using double layer electrical (b) flow of electrification schematic [13].....	26
Figure 14: Electrostatic free-fall separator [14].....	27
Figure 15: Correlation between the acceptor (α) and the donor (β) parameters [14].....	28
Figure 16: Display of a graham cracker coated with food powder [16]	30
Figure 17: Assembled of high pressure diesel chamber [17].....	32

Figure 18: Illustration of pressure vessel for subsea blowout preventers [19]	33
Figure 19: Finite element model of a pressure vessel used for hydrogen [21]	35
Figure 20: Illustration of the Von Mises stresses under the internal pressures (a) 40 MPa, (b) 80 MPa and (c) 120 MPa [22]	36
Figure 21: Dimensioned illustration of horizontal pressure vessel under test conditions [23]	37
Figure 22: Finite Element Analysis with grids for windows [24]	39
Figure 23: Cylindrical pressure vessel cross sections with four tapered sapphire windows [25]	41
Figure 24: Illustration of stress distribution for optical design at 5, 10 and 20 bar respectively [26].....	42
Figure 25: Course finite element sub-model meshing revealing center crack [28]	44
Figure 26: Image measurement calibration for fuel profile analysis [29]	46
Figure 27: Y direction measure of fuel to determine the width [29]	47
Figure 28: Fuel injection comparison with and without an Applied Electric Field [29].....	48
Figure 29: COMSOL model of fuel droplet particles without an Electrical Field Applied [29].....	49
Figure 30: COMSOL model of fuel droplet particles with an Electrical Field Applied [29].....	50
Figure 31: Entire System Overview.....	52
Figure 32: Parr Instruments Custom Reactor Design [30].....	55
Figure 33: Initial Cylindrical Pressure Vessel Design.....	57
Figure 34: Pressure Chamber Design based on Research from The Australian Maritime College	59
Figure 35: Von Mises Stress Simulation	60
Figure 36: Aluminum Alloy Sight Glass Design.....	63

Figure 37: Aluminum Sight Glass Simulation.....	64
Figure 38: Plain Carbon Steel Pressure Chamber Model	67
Figure 39: Plain Carbon Steel Pressure Chamber Simulation	68
Figure 40: Final Design of Pressure Vessel Model	72
Figure 41: Cross Sectional View of Final Pressure Vessel Design	73
Figure 42: Final Design von Mises Stress Default Mesh	74
Figure 43: Final Design von Mises Stress Fine Mesh	75
Figure 44: Factor of Safety Study for Final Design.....	76
Figure 45: Displacement Study of Final Design.....	77
Figure 46: Strain study of Final Design.....	78
Figure 47: Fuel Injection Characterization Summary [32].....	80
Figure 48: Battery Offset in Milliseconds [32].....	81
Figure 49: Programmable Automation Controller SEL - 2411	82
Figure 50: SEL PLC Code for activating the fuel injector	83
Figure 51: Existing Equipment and Test Setup	86
Figure 52: Graph of Cumulative Mass as a function of each Spray	88
Figure 53: Graph of Electrical Charge for each Spray	91
Figure 54: Boxplot graph of Electric Charge data distribution.....	92
Figure 55: Defined cylindrical geometry with global and model parameters	94
Figure 56: Mesh representation of defined parameters for simulations	94
Figure 57: Distribution of particle diameters.....	95
Figure 58: Rayleigh limit distribution of charge.....	95
Figure 59: Particle Trajectories at 40 psi with no electric field applied	96

Figure 60: Particle Trajectories at 40 psi with an electric field of 10kV applied	96
Figure 61: Particle Trajectories at 50 psi with no electric field applied	97
Figure 62: Particle Trajectories at 50 psi with an electric field of 10kV applied	97
Figure 63: Particle Trajectories at 60 psi with no electric field applied	98
Figure 64: Particle Trajectories at 60 psi with an electric field of 10kV applied	98
Figure 65: Electric potential for 20kV when time = 0.0195	99
Figure 66: Particle Trajectories at 40 psi with an electric field of 20kV applied	100
Figure 67: Z-axis of symmetry for deflection of droplets with an electric field of 20kV applied at 40 psi	100
Figure 68: Particle Trajectories at 50 psi with an electric field of 20kV applied	101
Figure 69: Z-axis of symmetry for deflection of droplets with an electric field of 20kV applied at 50 psi	101
Figure 70: Particle Trajectories at 60 psi with an electric field of 20kV applied	102
Figure 71: Z-axis of symmetry for deflection of droplets with an electric field of 20kV applied at 60 psi	102
Figure 72: Initial Quote from Parr Instrument Company [30].....	110
Figure 73: SolidWorks drawing for the body for the pressure chamber.....	111
Figure 74: SolidWorks drawing for the top lid of the pressure chamber.....	112
Figure 75: SolidWorks drawing for the bottom of the pressure chamber.....	113
Figure 76: SolidWorks drawing for connecting rods of the pressure chamber	114
Figure 77: SolidWorks drawing for the flange of the pressure chamber	115
Figure 78: Dimensions of EV 14 Long fuel injector from Bosch Engineering [35]	117
Figure 79: Fabrication Associates Inc. financial quote for custom pressure chamber [34].....	118
Figure 80: Certified Drawing from FAB Inc. of constructed Pressure Vessel [34]	119

CHAPTER 1: INTRODUCTION

The basic overview of an Internal Combustion Engine (ICE) will be the first item introduced in the subsiding Literature Review. This section will describe why an ICE is referred to as a reciprocating engine and the process which occurs inside to produce useful work. Different reference positions inside an ICE will be identified and an explanation of why it is important will ensue. Each phase of a 4-stroke spark ignition engine will be elaborated upon and the significance stated. The device used to control the entire 4-stroke process of the Otto cycle and the precision required for optimal operating conditions as well as the consequences of the resulting from time synchronization deficiencies.

A brief analysis of different fuels will then ensue after this point. This will include the chemical and physical properties as well as the specific applications and the effects of different fuel profiles. Different chemical elements combining to produce unique compounds and the impacts on the environment will also be evaluated. The definition and importance of knocking will also be examined. This comprises of the numerical assessment of the combustion process as well as the scale and the range along with the fuel types which are applicable. Once the properties of fuel are understood, a further investigation will ensue related to the injection process of different types of fuel at varying injection pressures for distinct timing results for increased fuel performance. This leads into details about the components and functionality of the fuel injection system in particular, the High Pressure Common Rail Injection System (HPCRIS) along with a brief list of critical sensors installed on the ICE of today. Experimentations with the fuel

injector nozzle geometry were also considered which included the use of injectors with multiple holes. This impacted the droplet size distribution, fuel spray profile and dispersion volume.

The process of the electro spraying is explained along with the industrial applications and the component details required to perform this technique. An outline of the produced results as well as the substances and materials which are used in conjunction with this process is described. The effects exhibited by the surface of the test specimen are similarly assessed. The Rayleigh limit was also used to represent the distribution of particles in order to determine the operational useful range. A discussion of typical conductivity values of different materials and at which values represents an insulator and a nonconductive resistance to electricity. Correspondingly, triboelectrically charging is detailed and the usefulness to produce an electrical charge for multiple applications. Comparison of corona and triboelectric charging occurred in relation to coating along with the effects of a Faraday cage and Ionization.

Next in the Literature review are the developments and requirements for a pressure chamber. One of the first relevant articles came from the Australian Journal of Mechanical Engineering and the pressure chamber was used for dynamics of diesel spraying. This leads into the size specifications for the entire vessel along with the construction material as well as the maximum and working pressures. This research was particularly beneficial due to the installation of high pressure specialized windows. Other research outlines pressure vessel which are used in deep subsea condition which means the vessel is capable of withstanding both enormous internal and external pressure simultaneously. At this point, the introduction of the Finite Element Analysis (FEA)

simulation process occurs and the invaluable usage which allow for a construction of a 3-D model representation without having to build a physical depiction. This can be done in a software called ANSYS which allows for specification as well as adjustment of the mesh parameters and is frequently used industrially. Investigation into composite layers for pressure chamber was additionally evaluated. Maximum failure stress criterions for pressure vessels of different types and presentations were also accomplished. The importance of Von Mises, displacements, strain and factor of safety are likewise outlined. FEA was additionally used to evaluate and analyze different types of windows such as fused silica, fused quartz, tapered sapphire and Pyrex glass. O-ring seals were also explored as a method to ensure no leakage of pressure.

The final section of the literature review discusses the prior experimental work done by Logan Garris. The research revolved around conducting fuel spray injections inside a chamber which was open to the atmosphere and maintained at room temperature. Four experiments were conducted with two operating with an applied electric field voltage of 10kV while the remaining two operated without any electric field applied. A high speed camera was used to capture the images of the injected fuel for analysis. Fuel profiles were generated and the results of the non-electric field test were compared with the applied electric field test. A simulation model was moreover developed in COMSOL Multiphysics and compared to the experimental data.

The methodology begins by outlining the entire system overview with an initial plan and vision based on the literature review and prior research. In order to future investigate the effects of electrospraying and tribocharging, it was evident a pressure vessel would be required. This was because additional evaluations of higher pressures

were compulsory. The next step was to develop a 3-D pressure vessel model in SolidWorks. After a very prolonged search, Parr Instruments Company stated a financial quote following a very substantive discussion concerning specifications. It was ascertained that this quote was outside of the allotted economical resources to fund this research. The exploration of a more feasible design for construction was pursued at this point. Next, an approach was taken to modify the design of the high pressure chamber used in Australia which was previously referred. Once again, even without identifying the itemized bill of materials for this project, after careful considerations it was apparent this proposal was not a possibility monetarily.

The fundamental justification for beyond budget pricing was due to the windows. Not only would the installation of windows amplified the final design price, the intended specified windows were to be oblong and constructed from fused silica or sapphire. This window design was exchange for sight glasses which were to be mounted on opposite faces of the rectangular pressure vessel. Although, the viewing area and the rated operational pressure for experiments would be decreased, the proposal was contained in the apportioned financial statement. Nevertheless, even with the SolidWorks simulation verification, manufacturing companies were not engrossed in fabricating a unique square pressure vessel. The design was then altered back to a cylindrical chamber.

Once this was completed, the North Carolina Administrative Code for uniform boilers and pressure vessels were referenced to ensure all safety as well as regulation requirements were met followed. As a result of the North Carolina Administrative Code, the internal diameter of the pressure chamber along with the maximum working pressure

was reduced. After intense communications with Fabrication Associates, Inc. a pressure chamber design was finally agreed upon and production commenced.

Subsequently, the fuel injection system was designed and developed after the required equipment was purchased. The equipment encompasses fuel lines, a fuel tank, a fuel pump, a fuel regulator, a fuel filter and a four set of fuel injectors. A Schweitzer Engineering Laboratories (SEL) PLC which was implemented in prior research by Logan Garris was similarly employed to control the activation of the fuel injector. After the delivery of the custom pressure vessel from Fabrication Associates, Inc. the pressure vessel was mounted to an available mobile 80/20 cart. Wood and strategically located cardboard bestowed a barrier amongst the aluminum surface and the faces of the bolts on the chamber as to not produce abrasions.

The results include both experimental and simulation results. The experimental findings include the investigation of the cumulative mass as well as the electric charge density for each of the 20 sprays performed at the pressures of 40, 50 and 60 psi. These outcomes generated the computations of the average mass per injector, the average volume per injector and the average net charge density values per injector for the three pressures. Whereas, the simulation results was modeled in COMSOL Multiphysics and illustrates both the distribution results for both the particle diameters and the charge for a droplet when an electric field was applied. The particle trajectories were compared for evaluations with and without the presence of an electric field for the internal pressures of 40, 50 and 60 psi for the cylindrical geometric model. The consequences of intensifying the potential difference which generates the electric field were correspondingly examined.

Finally, the results were interpreted and discussed for both the analysis of the experimental and simulation results at the pressures of 40, 50 and 60 psi. The regression trend and the statistical data distributions were examined for both the cumulative mass and electric charge density respectively. The preliminary results for the simulation models without an electric field, with an electric field and with an increased electric field were all considered. A list of six potential future work descriptions were furthermore identified for possible guidelines in order to further the research in to electro spraying and advance manipulation of dielectric fluids.

CHAPTER 2: LITERATURE REVIEW

This Literature Review section will outline a summary of previously explored information regarding the overall research. The beginning of this literature review proceeds with a discussion on the basics of an Internal Combustion Engine (ICE). A discussion on the fuel injection system ensues which details former use of equipment throughout the years and specifications of data acquisition software along with the corresponding results. The effects of various nozzle geometries as well as changing spray angles are also explained and yield different outcomes depending on the application. The effectiveness of electrospraying which is used in many disciplines of science is likewise described subsequently. Electrospraying is a process of passing a dielectric fluid through a high potential difference source. When combined with triboelectric charging, which occurs when an electric charge is produced by the contact of a travelling dielectric fluid inside a solid tube or pipe. The results of these practices produce a reduction in droplets size as well as charged droplets. Similar experimental equipment is also discussed and outlined related to the relevant research.

Pressure Chamber Development was also considered in order to achieve test conditions with elevated pressures. Based on the literature review, stainless steel is a common material used for the construction of pressure chambers. The knowledge of 3-D modeling software is correspondingly evaluated using different parameters to determine various failure conditions. The final discussion which occurs in this literature review is the synopsis of the previous research work done by Robert Logan Garris. These results include experimental and simulation investigative outcomes.

2.1 Basics Overview of an Internal Combustion Engine

Reciprocating Engines are the most commonly used form of Internal Combustion Engine (ICE) used today commercially which consist of both gasoline and diesel fuel operations. Work is produced by movement of a piston inside a cylinder connected to a crank shaft. Expectedly, the piston is restricted to finite displacements inside the surrounding cylinder. When the piston is at the very extreme top of the cylinder which is closest to the inlet and exhaust valves, this is known as the Top Dead Center (TDC). Whereas, when the piston is the furthest distance away from the same inlet and exhaust along with the nearest distance to the crank shaft is referred to as the Bottom Dead Center (BDC) [1]. The displacement of an ICE can be determined by dividing the cylinder diameter by two, squaring the result then multiplying by two π and the crank radius. The volumetric compression ratio is achieved by dividing the volume when the piston is at BDC by the volume when the piston is at TDC. Figure 1 below demonstrates a pictorial representation of each phase for a 4-stroke spark ignition engine which occurs in most consumer driven vehicles during modern times.

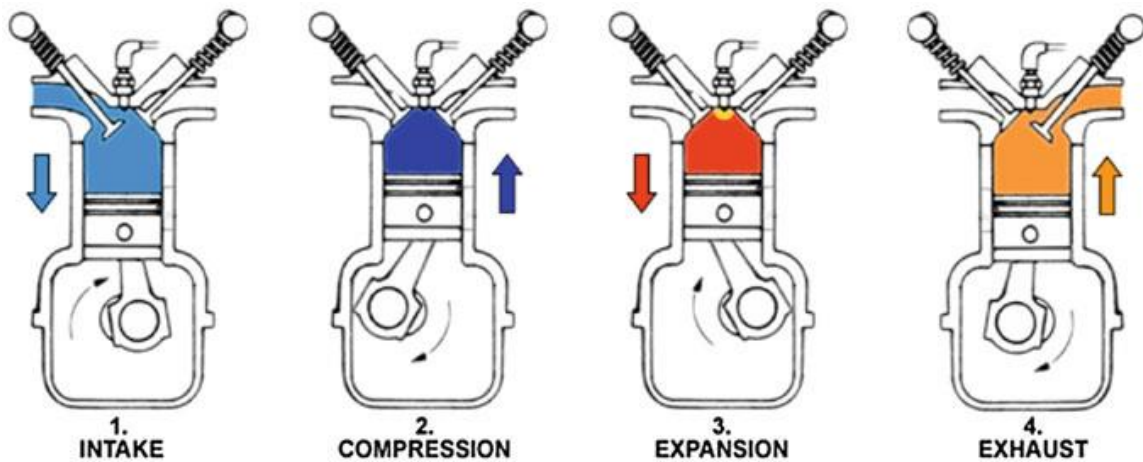


Figure 1: Visual illustration of each phrase for a 4-stroke spark ignition engine [1]

In order for the combustion to ensue, the first procedure which must transpire is intake. During the intake phase denoted by 1, the piston travels from TDC all the way to BDC while fuel and fresh air is drawn into the cylinder through the inlet valves by a change in pressure which creates a vacuum like effect. At this point, the compression sequence at 2 begins by the closing of the intake valve and the fuel along with the fresh air is pushed upwards towards TDC. When TDC is established, an electronic device which is indicated as spark plug receives an electrical signal from a distributor or the Electronic Control Unit (ECU) and introduces a spark into the combustion chamber in order to ignite the mixture of air and fuel. This in turn rapidly increases the pressure as well as the temperature inside the cylinder. A resulting explosion occurs which subsequently forces a violently expansion of the piston to BDC. During this expansion process designated by 3, work is done for the only time on the piston by the ignited air and fuel mixture. The final process at 4 initiates with the opening of the exhaust valve as the piston starts to travel upwards towards TDC. This retroactively thrusts the spent and burnt gases dynamically out of the combustion chamber and into the exhaust port. Once the piston reaches TDC at this point, the entire process launches again at 1 with the opening of the intake valves.

Different fuels have different physical and chemical properties which determine the affect or profile of an ICE. Each type of fuel has unique characteristics which allow for favorable operating applications but also impact the environment distinctively. Typical everyday commercially used gasoline grades are made mostly from a mixture of hydrocarbon, paraffins, olefins and aromatics [2]. Hydrocarbons are simply alkane compounds which consist of the two elements hydrogen and carbon. While, paraffins are

derived from crude oil which is a saturated or concentrated version of the same hydrocarbons and are not adept to undergo any further reactions. On the other hand, olefins are alkenes and an unsaturated form of the hydrocarbon compound. Although, aromatics are arenes along with nitrogen and sulfur produces a compound which is organic. After all of these substances are combined, the resulting gasoline mixture can contain more than 500 organic compounds.

The hydrocarbons refined for the gasoline mixture are very volatile and range widely in properties. This means it is vital for the gasoline mixture to be blended in a balance and correct way to adhere to engine performance over the entire operating parameter range. The properties of fuel affect the fuel storage conditions, the fuel delivery and injection system, circumstances under which the fuel will ignite, the combustion process, the emission by products and the overall fuel efficiency of the engine.

One of the most significant ways to identify the properties of a specific fuel is by the Octane Number (ON). This number precisely relates to the combustion process and indicates the numerical value for relative antiknock. Knocking or auto ignition is a tinkling sound which can be heard from an engine which reveals a disruption from the normal combustion process. Auto ignition transpires when the mixture of fresh air and fuel ignites the flame front ahead of the unburned mixture. Reduction of performance along with decreased fuel efficiency can occur when a wave of high pressure results from an explosion of high temperature and engine damage may also be a consequence.

Meanwhile, the ON typically only refers to automotive and aviation fuel of rating below 100 and is a comparison of isooctane, normal-heptane and reference fuels ranging

between 100 and 0 respectively on the scale for knock-rating. When an engine is operating under conditions considered to be mild, the two reference fuels are blended with an isooctane volume percentage matching fuel sample knocking tendencies, is better known as the Research Octane Number (RON). Figure 2 below shows the relationship between the boiling point of the volatile hydrocarbons and the octane number.

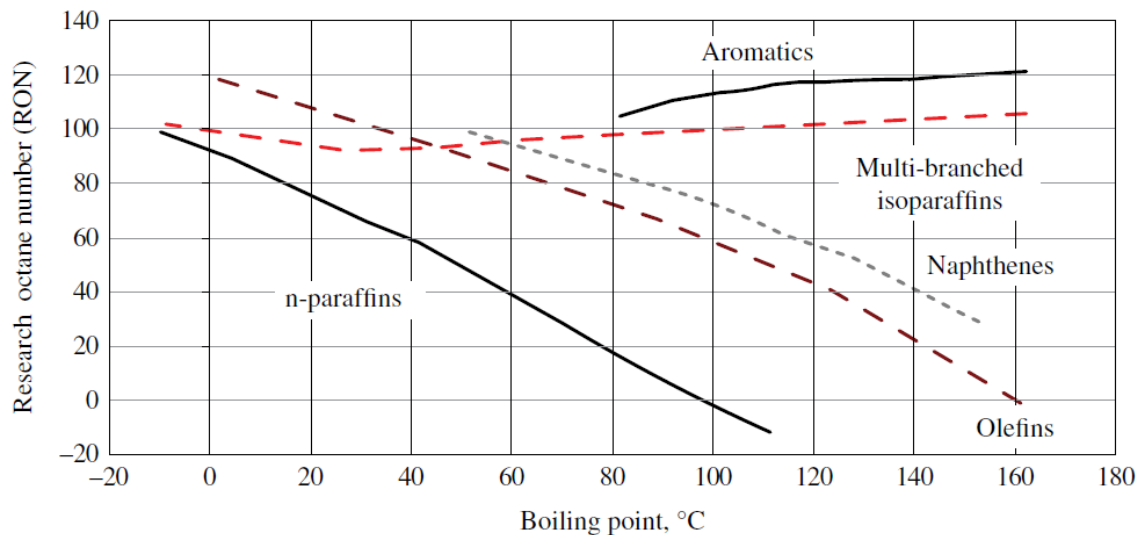


Figure 2: Octane number and boiling point relationship for hydrocarbons [2]

It is worth noting based on the graph above, aromatics such as xylenes, benzene and toluene have the most resistance to auto ignition while n-paraffins qualifies for the least resistance to knocking. The auto ignition inclination intensifies as the operating condition temperatures of the engine escalate. On the other hand, the compression inside the combustion chamber has the greatest influence on the knocking resistance.

Further research on pressure combustion related to the timing of fuel injections were conducted by Agarwal et al. in India [3]. This investigation was done using a one cylinder diesel which is a Compression Ignition (CI) engine for the evaluation of the performance characteristics and emissions by products. The rate of heat released (ROHR)

during rapid combustion at high cylinder pressures was also assessed with advanced timings for fuel injections.

Experiments were conducted at different Fuel Injection Pressures (Fuel Injection Pressure) of 500 and 1000 bars. After about 200 combustions, an examination of the ROHR and the Mass Burn Fraction (MBF) durations were executed. The Start of Injection (SOI) timings were also varied from three intervals of 9.375, 12.750 and 15.000 respectively all from Before Top Dead Center (BTDC). While the Fuel Quantity Injected it was 9, 12 and 15 per Stroke. Figure 3 below displays the outcomes of the tests operated at 500 bars.

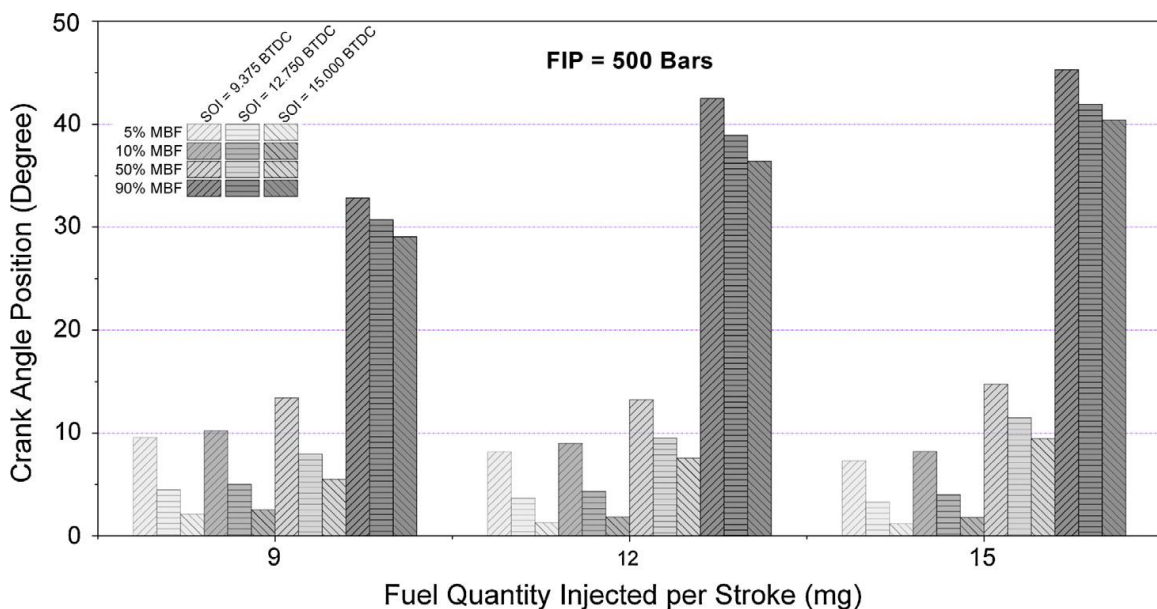


Figure 3: Start Of Injection (SOI) for different fuel quantities with Mass Burn Fraction (MBF) variations at Fuel Injection Pressure (FIP) of 500 bars [3]

The angle of the crank experienced values between -40° and 45° while the cylinder pressure yielded data from 0 to 70 bars for both FIP of 500 and 1000 bars. It is worth noting, as the fuel quantity injected is increased the combustion duration also improved. This is primarily due to the extended time for the combustion to diffuse.

Premixing of the combustion occurred for the most part at the same rate for each experiment. This resulted in a rapid burn of the fuel and very minute distinctions of the position of the crank angle at 50% MBF. These results conclude that when the timings for the fuel injections are advanced, the characteristics of the engine emissions undergo an improvement. It is also worth noting, as the engine load increases so does the concentration of the particulate number inside the CI engine.

2.2 Fuel Injection System

For the fuel to be at an appropriate level for evaluation in the high pressure chamber, a high pressure common rail system is required. Wang et al. have devised a setup which delivers fuel from a high pressure pump to a common rail and then to the injection [4]. This system is controlled by an Electronic Control Unit (ECU) which pulses when a negative voltage (ground) is applied. Leakage is also accounted for by the installation of a return line. The fuel injector nozzle geometry has an impact on the volume, droplet size distribution and determines the fuel spray profile. Figure 4 below shows a schematic representation of the test setup for a diesel internal combustion engine.

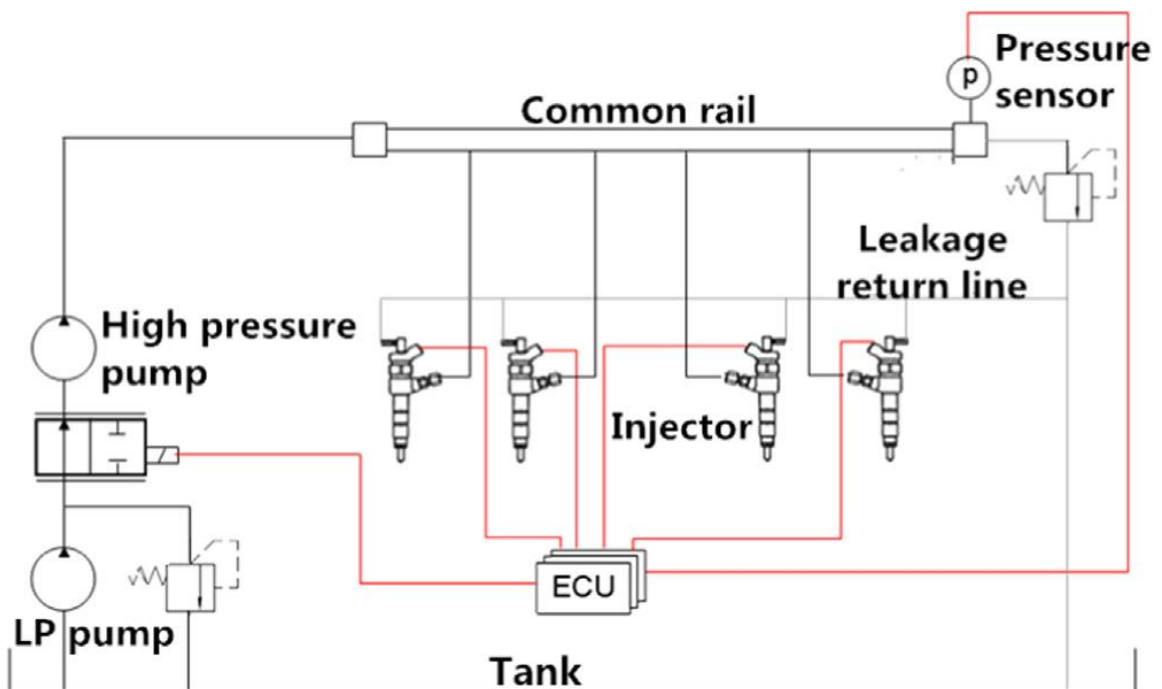


Figure 4: Illustration of a common high pressure rail system[4]

The main component in the High Pressure Common Rail Injection System (HPCRIS) is the ECU. This controls and determines when the injector is supplied with ground to the negative terminal to complete the circuit in order for fuel to exit the injector

and enter the cylinder. To accomplish this, the ECU is intertwined and receives input from other sensors on the engine such as the Air-fuel Ratio, Engine Speed Sensor, Throttle Position Sensor, Crank and Cam Position Sensors, Manifold Absolute Pressure, Mass Air Flow Sensor, Oxygen Sensor and Fuel Pressure Sensor.

Yao et al have done extensive research on the Sauter Mean Diameter (SMD) of the fuel [5]. Experiments were conducted by alternating the injection pressure, decreasing the orifice diameter and the results were captured using time resolved images from a high speed camera. This setup is similar to the previous setup however, this setup contains a constant volume combustion chamber of size 80 mm inside diameter and 268 mm internal depth and a maximum operating pressure of 10 MPa. This arrangement is focused more on the data acquisition. Figure 5 shows the more sophisticated system design. The high speed camera has a maximum shutter speed of 2 microseconds and 675,000 frames per second for capturing images. The sampling frequency for the Data acquisition (DAQ) can achieve 70 kHz.

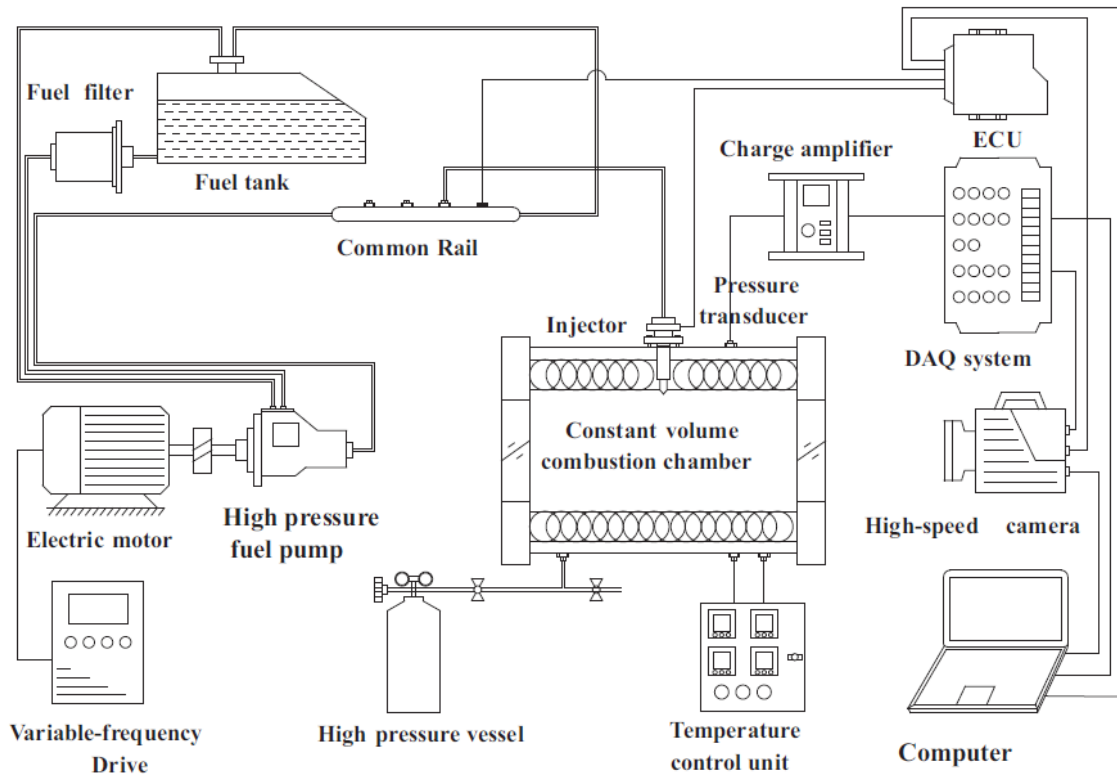


Figure 5: Diagram representation of a constant volume combustion chamber system[5]

This schematic layout allows for fuel injection experiments to be conducted between the ranges of 40 MPa and 120 MPa with 40 MPa intervals. The lengths of injections were designated to be 3 milliseconds. In order to capture the injection, the DAQ was engaged as soon as the signal was delivered to the injector. This allowed for the recording of the droplet size on the computer connected to the high speed camera.

Another method which is used to manipulate the fuel as it leaves the injector is to increase the amount of holes in the injector. Characteristics of the internal flow of the fuel were evaluated by Dong et al. [6]. The rail pressures for the diesel fuel injector during the experiments were observed to be as low as 80 MPa and as high as 180 MPa with a baseline of 120 MPa. The results revealed a lower injection rate, a shorter spray tip penetration, a wider spray angle and a longer injection duration for the multi-hole injector. Figure 6 demonstrates the two types of nozzles of two different types of fuel injections during experimentation.

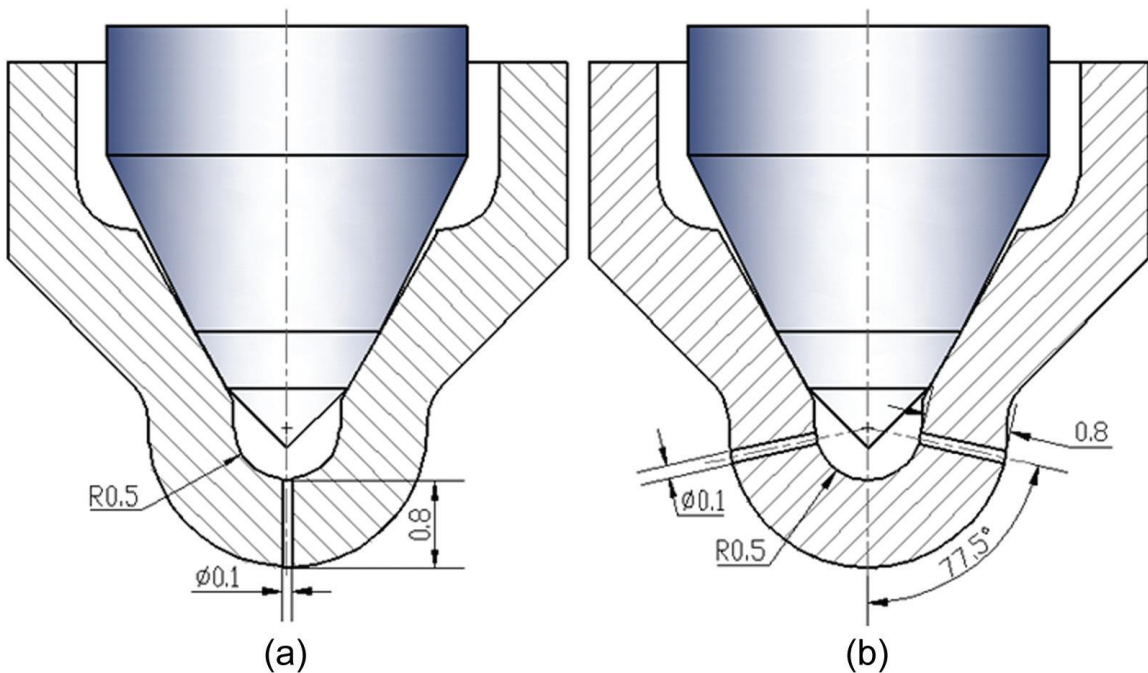


Figure 6: Diagram schematic of different nozzles for the experimentation (a) single-hole (b) multi-hole [6]

The fuel injectors were both solenoid operated however, the multi-hole nozzle is 0.1 mm in diameter with 10 holes. To represent a comparable version, the 10 holes were placed in a pattern which yielded the same sac configuration with cut sizes of the

equivalent length and diameter as the referenced singular hole. The included angle for each hole is 155 degrees.

2.3 Electro spraying and Triboelectric Charging Technology

Electrospraying is a technique which utilizes electrostatic charging and produces a fine mist which uses a nozzle for liquid to pass through as very high voltage is applied. This results in a no droplet coagulation when these charged droplets are self-dispersed in space [7]. Electro spraying can be used for both liquids and very fine powders. Electro spraying is used in both the scientific and instrumentation industries. However, electro spraying is also used in medical technology for manipulation of micro and nanoparticle production on films as thin as nanometers. Figure 7 below indicates a visual representation of some equipment required for electro spray testing.

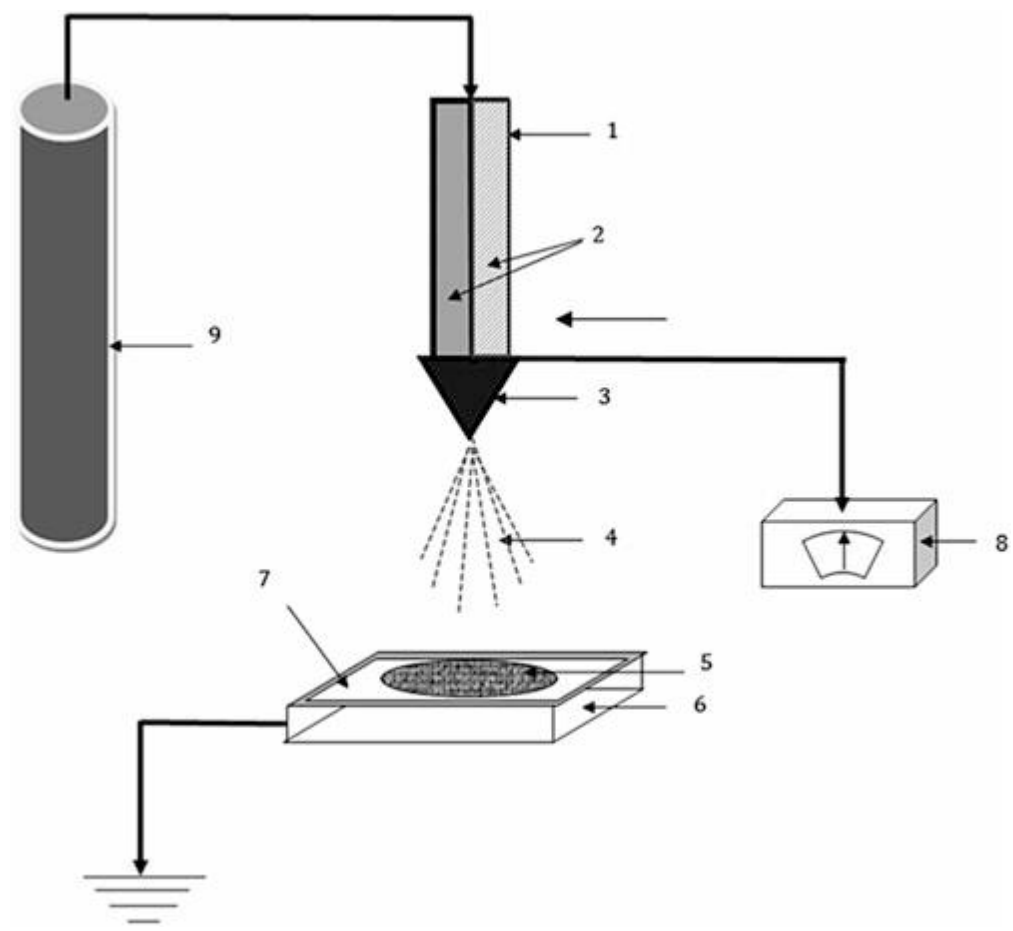


Figure 7: Schematic illustration of bi-component equipment setup for electro spraying [7]

This equipment includes a container which stored the substance to be tested is listed at number 1 with the polymer solutions indicated at number 2 and is connected to a nozzle at number 3 with a positive terminal. A power supply is used to achieve the high voltage required to charge the droplets before dispersion is represented at number 8. After dispersion, the droplets travel downwards towards the metal collector plate at number 6 which is coated with a polymeric solution while on the fabric substrate detailed at number 5. Compressed nitrogen gas specified at number 9 is used to pressurize and help force the test polymeric solution out of the nozzle.

Gomez and Tang constructed a similar test setup as displayed in Figure 8 at Yale University in 1992 in order to experiment with the charge and fission of droplets in electrostatic sprays [8]. Coulombic repulsion occurs when there is a net charge present on the surface of a droplet. This causes a reduction in binding forces due to the tension at the surface of the droplet which holds it together.

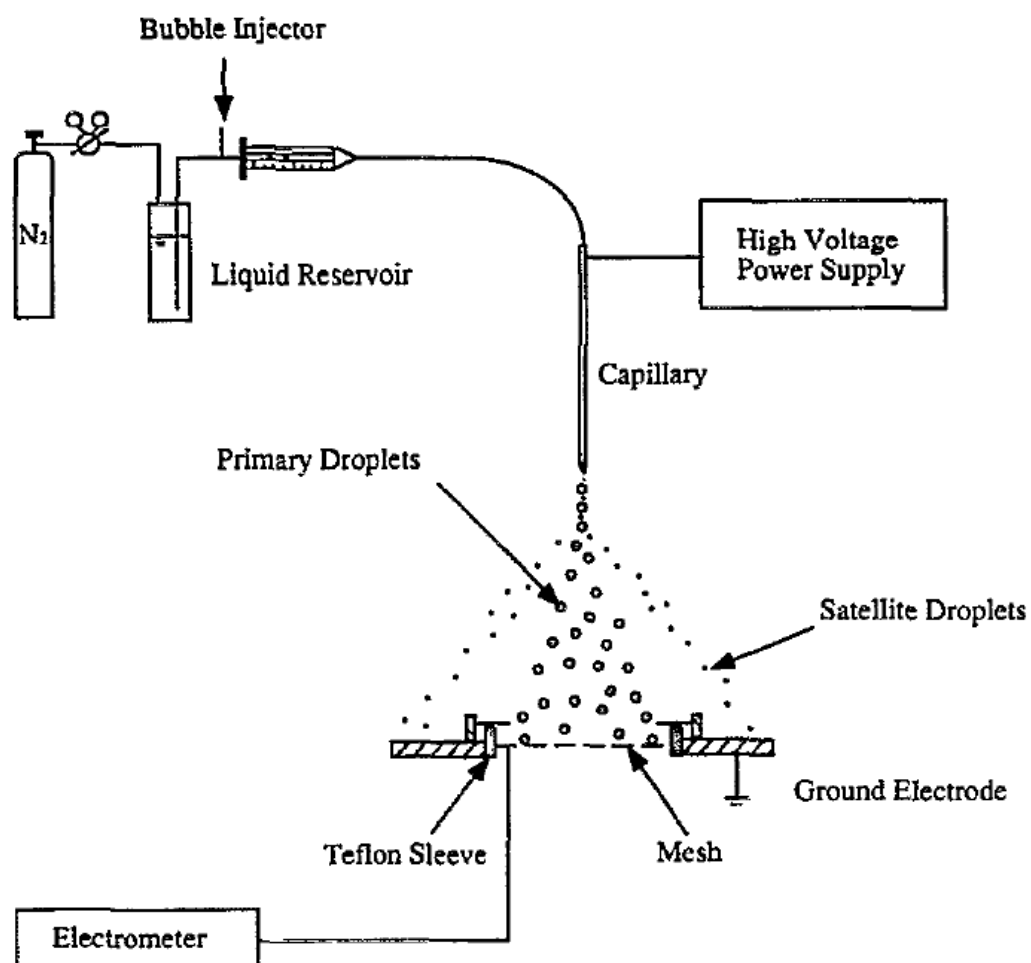


Figure 8: Electro spray system schematic [8]

The results of testing indicate that there is a decreasing function of size as related to the droplet charge to volume ratio. There was also a manifestation that droplets would be closer to the Rayleigh limit the larger they were once the electro spray operation useful range was maintained.

Different liquids have different physical as well as chemical properties and these properties determine the conductivity of the liquid. A liquid is considered to be a conductor when the conductivity is larger than $10^{-12}/\Omega\text{m}$. Whereas, a liquid will be classified as a nonconductive and an insulator if there is a resistance of electricity above $10^{10}/\Omega\text{m}$ [9]. Figure 9 expresses the basis for engineering design as well as operation of liquid electrostatic atomizers for both semi-conductive and conductive liquids.

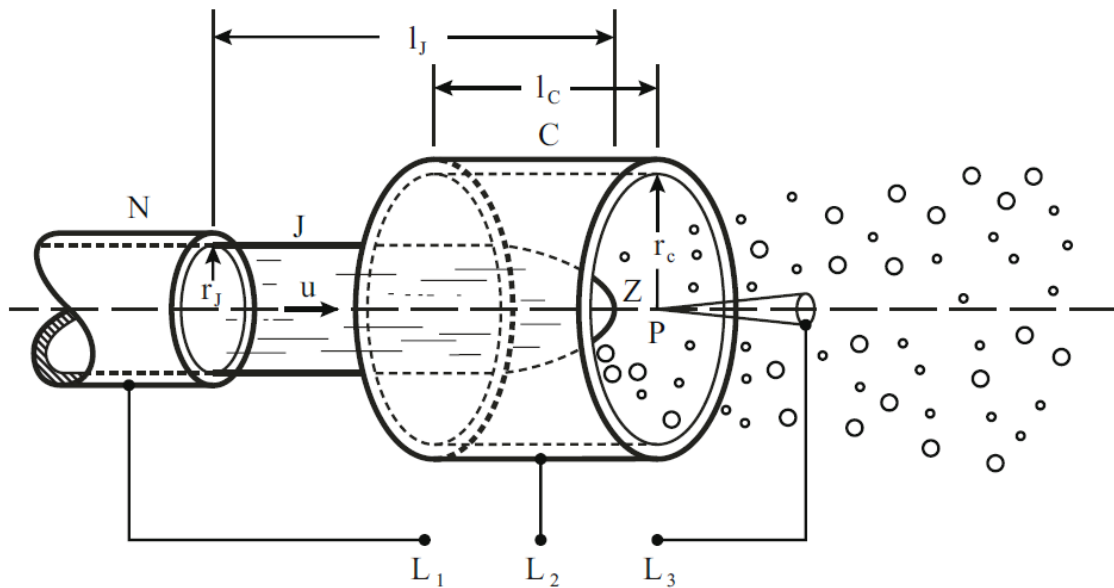


Figure 9: Illustration of electrode generalized geometry with spray dispersion representation [9]

It was observed that the liquid jet with a velocity from the nozzle travels towards the sharp electrode before it is discharged. L_1 , L_2 and L_3 represent the positioning of the liquid along the nozzle, cylindrical and discharge electrodes respectively.

Water was electro sprayed in at atmospheric pressure into air through narrow silica tubes by Lopez-Herrera et al. in Spain at the Universidad of Sevilla [10]. Figure 10 below shows a silica tube with a sharpened tip as well as an electrode made from silica with a grounded needle and the display of a steady cone jet of deionized water.

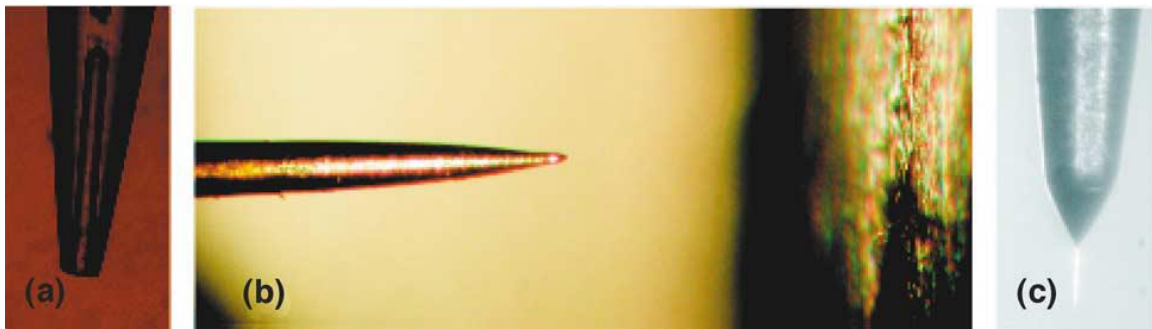


Figure 10: (a) Sharpened tip of silica tube (b) Electrode grounded needle made of silica with a stainless steel plate located between 3 and 5 mm away (c) Deionized water in a steady cone-jet [10]

The experiments were conducted with the water and the electro sprayed air environment at ambient room temperature. The results from numerous testing, indicate there was no corona discharged which is consistent with the laws related to cone jet and independent spraying of current in atmospheric air when water is electro sprayed.

Elghazaly and Castle conducted research on the breakup of charged liquid droplets [11]. An external electric field is applied to the tip of the capillary tube with a high potential where charged droplets of water exits. Water sensitive paper was used to collect the droplets which broke up as they were ejected from the nozzle. Figure 11 demonstrates liquid breakup of the droplets using a microscope to make observations on a scale of hundreds of micrometers.

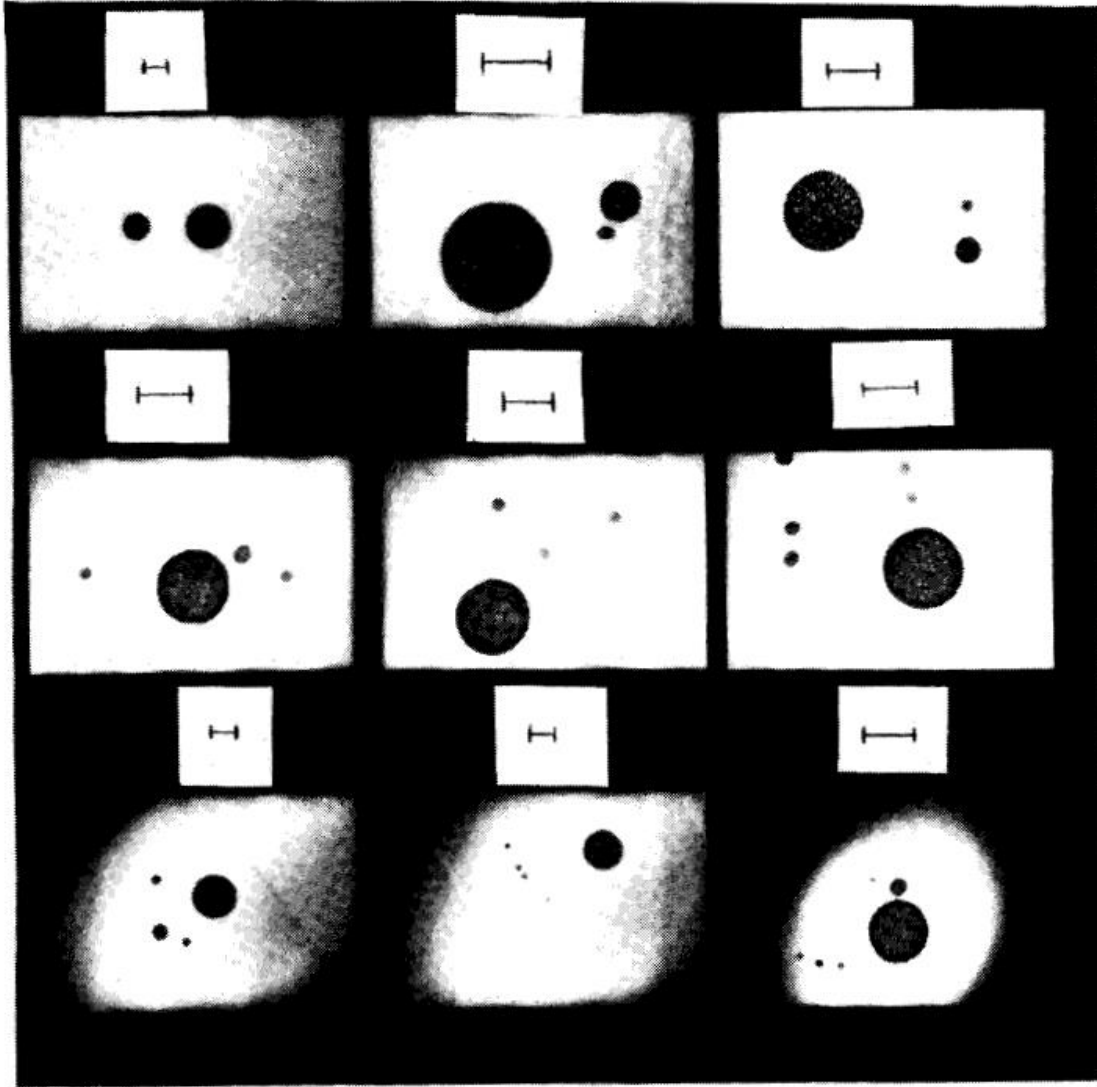


Figure 11: Contact prints of magnified collected droplets samples with a tick marking representing 200 micrometers [11]

The results indicated a tree like secondary breakups between the range of 5 and 50 percent of the ratio sibling mass. This also verifies and validates previously derived models.

Electrospraying is also sometimes coupled with the application of electrospinning depending on the application. Electrospinning can be used for operations which requires construction of microscale fibers and even nanoscale fibers [12]. High fields of electricity

are applied between a melt contained in a syringe which has a capillary tip or with a polymer solution and a collector which is electrically conductive. A liquid jet is expelled from the tip of the syringe when opposing forces are overcome from the generated electric fields. Figure 12 below shows this dispersion of the jet for both electrospinning and electro spraying.

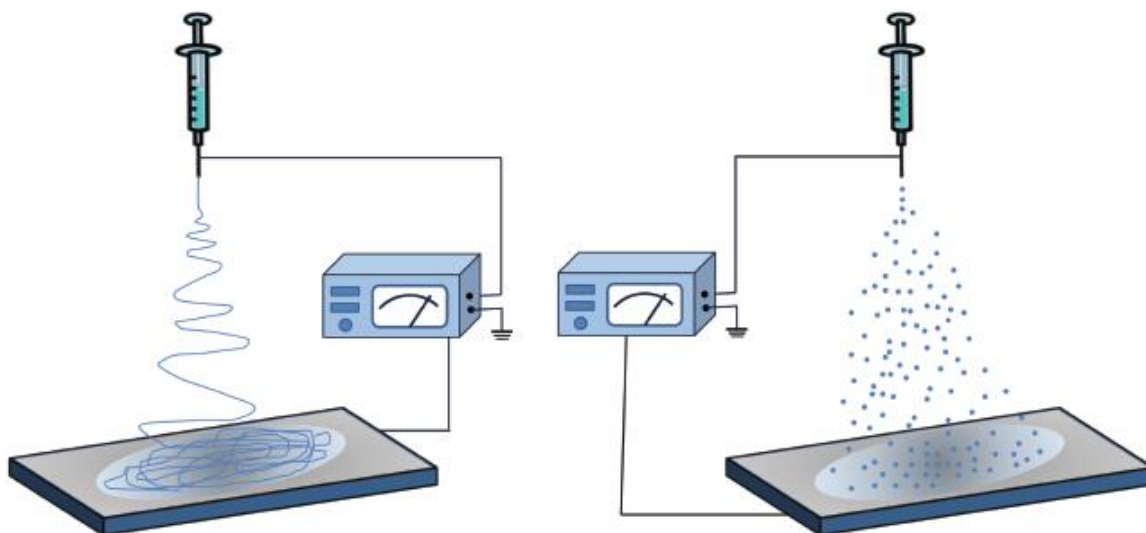


Figure 12: Fabrication of Nanofiber and Nanoparticles while (A) Electrospinning and (B) Electro spraying [12]

It is observed that the jet which is now electrically charged, leaves the tip of the syringe and travels relatively vertical downwards before becoming more unstable while scattering.

A current of streaming is generated whenever a liquid flows through a porous medium or a pipe[13]. Dielectric fluids contains electrostatic when contact is made with a solid pipe or tubing which results in the solid induction of an electrical double layer. Part (a) of Figure 13 represents two distinct sections of the Stern model which consist of the compact and the diffuse layer. On the other hand, Part (b) denotes the electrification of liquid flow into a collecting vessel in the illustration below.

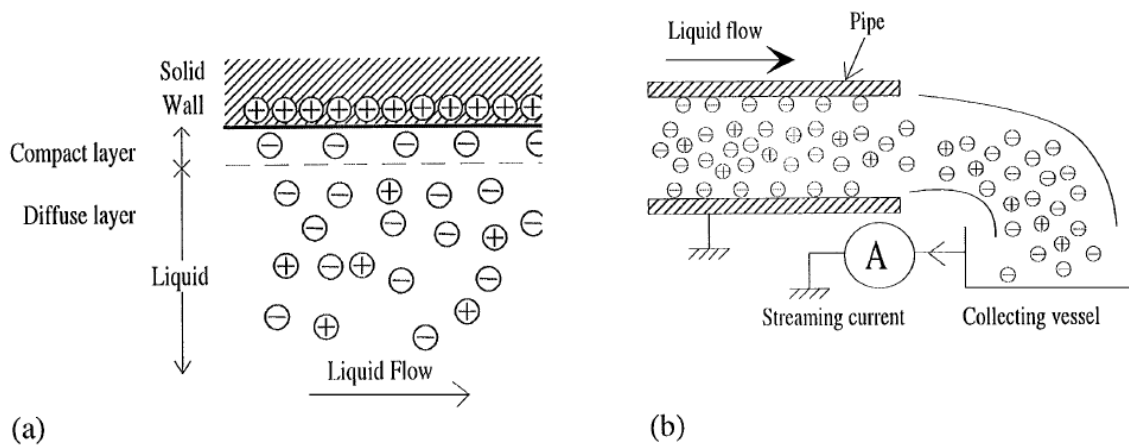


Figure 13: (a) Stern model using double layer electrical (b) flow of electrification schematic [13]

The compact layer is the layer which is closest to the wall and has no effect on the charge of the fluid. Although, the diffuse layer experiences a decrease in space charge density as the distance from the wall increases where the density is at maximum. Results introduced the velocity of the dielectric fluid at the wall (compact layer) which determines the development time of the charge density and the relaxation time inside the fluid (diffuse layer) are essential parameters.

Research was done on polymer triboelectric charging which dependence relies on thermodynamic surface properties and relative humidity by Nemeth et al. [14]. The goal of this research was to investigate polymer samples which for technological processes are represented as waste. Figure 14 below schematically represents the free fall electrostatic separator which includes the charging unit, the free fall separator, electrodes, Faraday cups, an electrometer, a high voltage power supply, an air-conditioning system, a sensor for in-stream charge measurements and a personal computer.

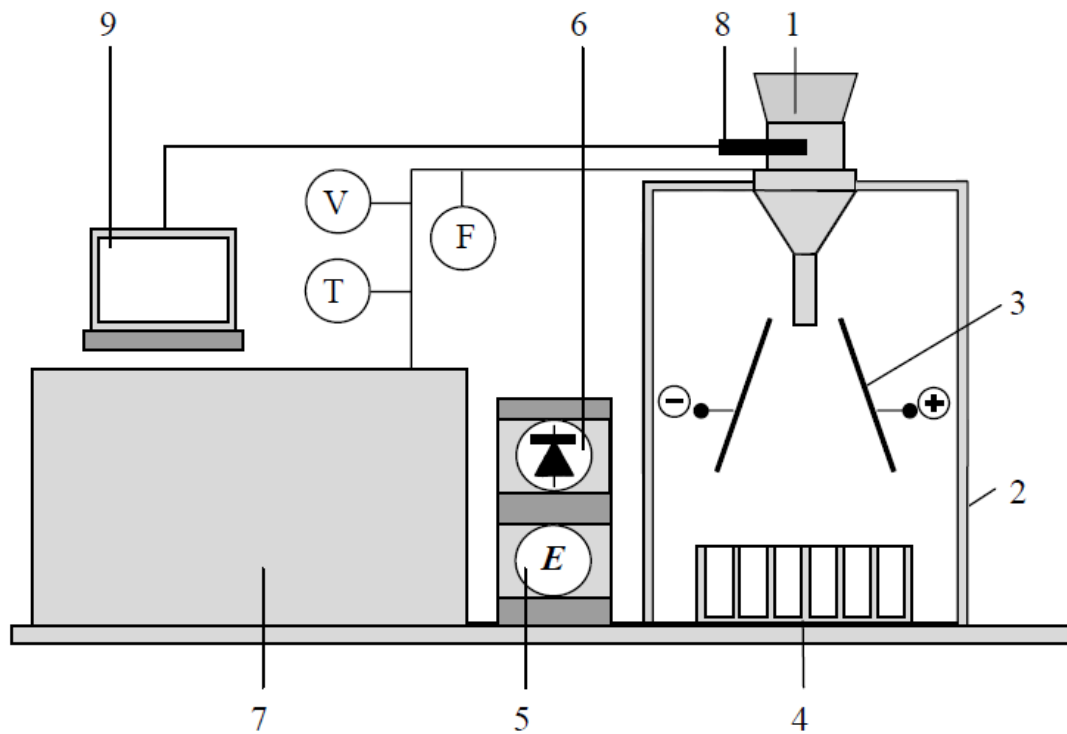


Figure 14: Electrostatic free-fall separator [14]

This setup has a few similarities to the system which will be fully detailed in the proceeding chapter. There is a fuel injector which supplies some charge to the working fluid and acts as a charging unit or a fluidized bed indicated by number 1. Furthermore, a Faraday cup acts as a collection tank and connects to an electrometer just like the devices

denoted in numbers 4 and 5 respectively. Electrodes which are designated by number 3 are also connected to a high voltage power supply represented in number 6 to produce a high electric field. Finally, Data Acquisition equipment was used to record the results from the experiments similarly to the personal computer specified in number 9.

The results in Figure 15 below shows an exceptional linear correlation between the surface charge amount and the acceptor and donor parameters related to the electron pair.

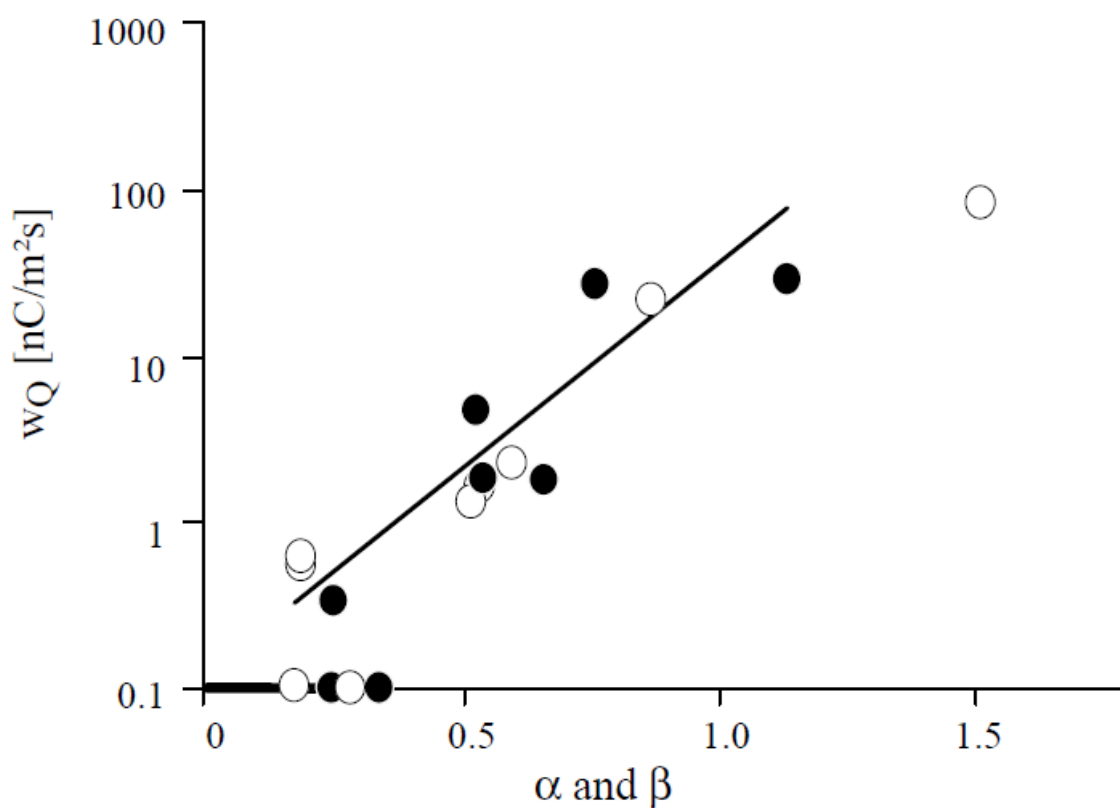


Figure 15: Correlation between the acceptor (α) and the donor (β) parameters [14]

When two particles interface with each other, a transfer of electrical charge occurs between the electron pair. The results also indicate an overlap of electron orbits transpires

while producing a new orbital. During this process, an electron is stripped off and exhibits a positive charge on the resulting negatively charged surface.

Triboelectric charging can also be used with powder as the working fluid in pneumatic applications. This involves the impact and collisions of powder particles of various shapes and sizes as researched by Bailey related to the science and technology of electrostatic powder spraying transport and coating [15]. There were three regions of powder coating the systems which were evaluated. The first region relates to the charged powder source. The second region correlates to the transportation of charged powder particles and the determination of aerodynamics, space charges and gravitational forces. The electric field of particles deposition is the final region for the experimentations.

Mayr and Barringer experimented with the charging for the electrostatic powder coating and compared the corona with triboelectric charging [16]. This was done in an attempt to evaluate the coating between non-electrostatic and electrostatic to determine improvements for triboelectric charging and corona. Nylon or Teflon can be used as the transportation medium in aiding with the tribocharging process. Figure 16 shows the graham cracker coated with salt along with the effect of the Faraday cage and the Ionization on the back.

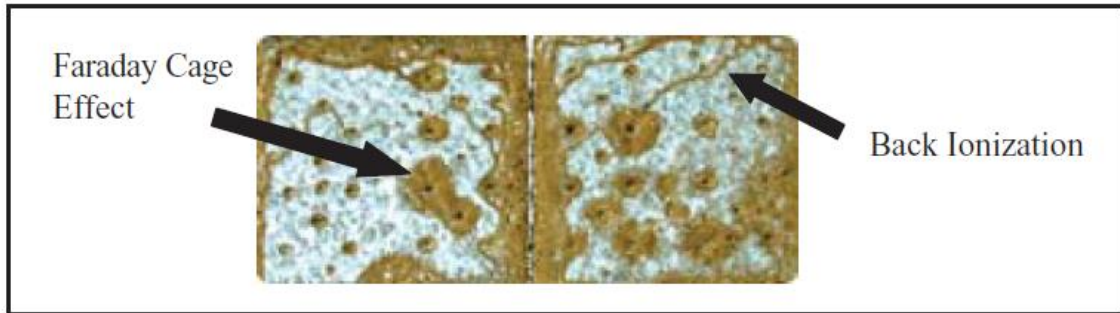


Figure 16: Display of a graham cracker coated with food powder [16]

The results displayed an increase in Transfer Efficiency (TE) of 27% as well as an adhesion improvement and a 99% reduction in dust over the non-electrostatic coating. It is also worth noting as the particle size increased, the amount of dust decreased.

2.4 Pressure Chamber Development

Pressure vessels are used for many different applications and functions. In order to replicate a high pressure environment that more closely matches the parameters within an IC engine, the design and construction of a high pressure chamber capable of operating at 6 MPa or 870 psi was required. Fortunately, pressure vessels are used in many applications for a variety of functions, so there are ample examples in the literature. Similar research involving spraying of fuel in a high pressure environment was done in Australia by Goldsworthy et al [17]. This research required the development of a high pressure chamber for diesel spraying. The material used for the pressure chamber was ASTM A479 316 stainless steel forgings. At 50°C, this material has a tensile strength of 130 MPa. As with all engineering designs where safety is a concern, a factor of safety must be determined. For this design, a factor of safety 7 was determined to be appropriate based on prior research done by Doyle and Kahan related to the optical glass design strength [18].

A window was installed for each of the rectangular faces on the pressure chamber as shown in Figure 17 below, which details the assembly. Due to high operational pressure, these windows were constructed out of UV quality quartz (high quality fused silica). A Double O-ring was used to seal all four windows to ensure a tight seal without applying clamping forces.

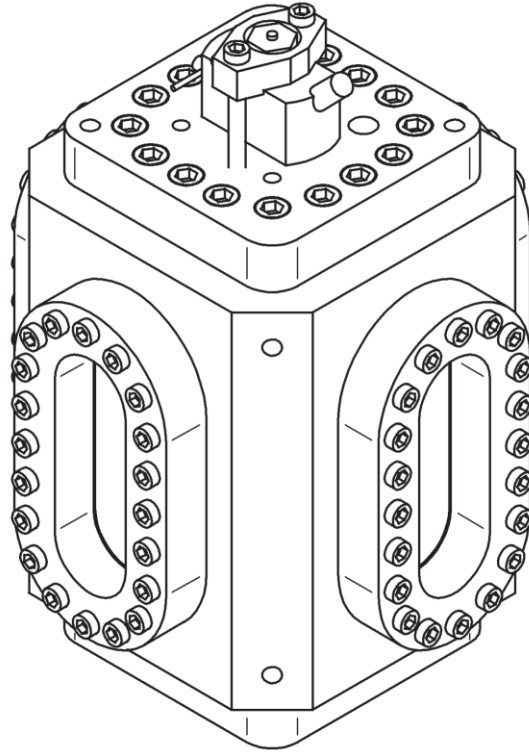


Figure 17: Assembled of high pressure diesel chamber [17]

This chamber has overall dimensions of 505 mm high x 300 mm square. The installed windows consist of a viewing area of 70 mm x 200 mm. The internal volume of the chamber is about 4 L. The dimensions of the internal cross-section for the rounded square are 120 mm x 120 mm, with 23 mm fillets.

Cai et al. at the China University of Petroleum conducted research related to pressure vessels [19]. The research entailed designing a pressure vessel for deep subsea conditions in order to prevent blowouts and catastrophic disasters. These pressure vessels are designed for an operational ultra-depth of 3000 m below sea level while the prototype external diameter is around 1000 mm and a thickness of 160 mm. The pressure vessel comprises of a hemispherical head attached to a cylindrical shell with an external functioning pressure of 29.4 MPa (4264 psi). The test materials were UNS S31603 (AISI

316L) austenitic stainless steel and UNS S31803 duplex stainless steel. Figure 18 below shows the representation of this pressure vessel with the designated elastic and plastic regions.

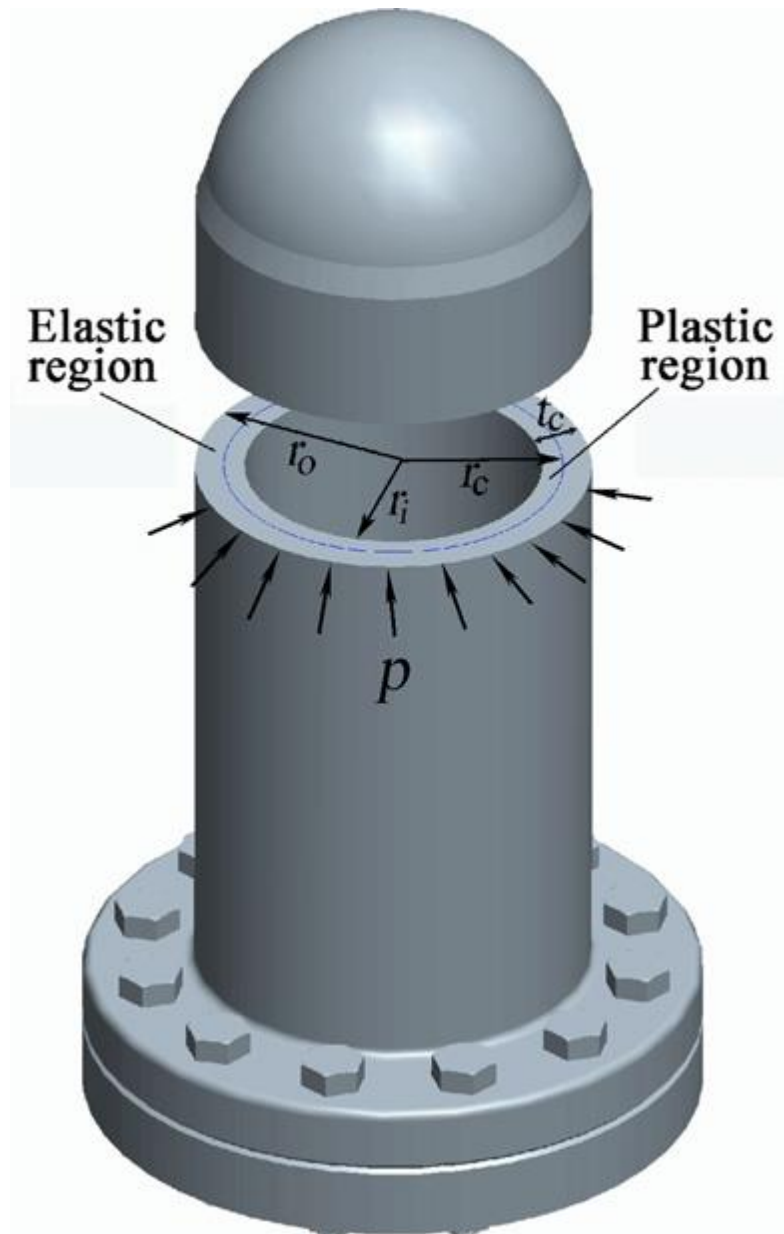


Figure 18: Illustration of pressure vessel for subsea blowout preventers [19]

Results indicate the Load and Resistance Factor Design (LRFD) method is more reliable for the cylindrical shell and hemispherical head with explicitly defined safety factors. This method is also referred to as the Limit States Design (LSD) and is based on the prediction of pile loads along with resistance to pile capacity, while using statistical probability or expressions for safety validation [20]. On the other hand, the Working Stress Design (WSD) method shows different reliability methods for the different components [19]. This procedure is likewise referred to as the Allowable Stress Design (ASD) and consists of estimating the actual forces which are directly applied to a test specimen. In order to determine the safety factor, the ratio of all resistances are evaluated with all of the loads influencing the examination samples [20]. Therefore, the bottom of the cylindrical shell in the vertical direction and the top of the hemispherical head in the horizontal direction were both restrained for the definition of boundary conditions. When the 29.4 MPa of external hydrostatic pressure was applied to the design, the UNS S31603 stainless steel exhibited a Young's modulus of 200 GPA and a yield stress of 170 MPa with a Poisson's ratio of 0.3. The method used to determine the forces on the entire chamber was Finite Element Analysis (FEA) in the software ANSYS. This was done to confirm the numerical analysis and validation of the design results [19].

Son et al. at Chung-Ang University have conducted experiments regarding storing hydrogen inside pressure vessels for fuel cells of a vehicle[21]. These pressure vessels are designed to operate at a high capacity at 70 MPa. FEA with preset winding patterns were used to determine the forces experienced by the pressure vessel with relative precision. Figure 19 outlines the shape of the 113 Liter geometry with aluminum 6061-T6 liner and carbon epoxy composite layers.

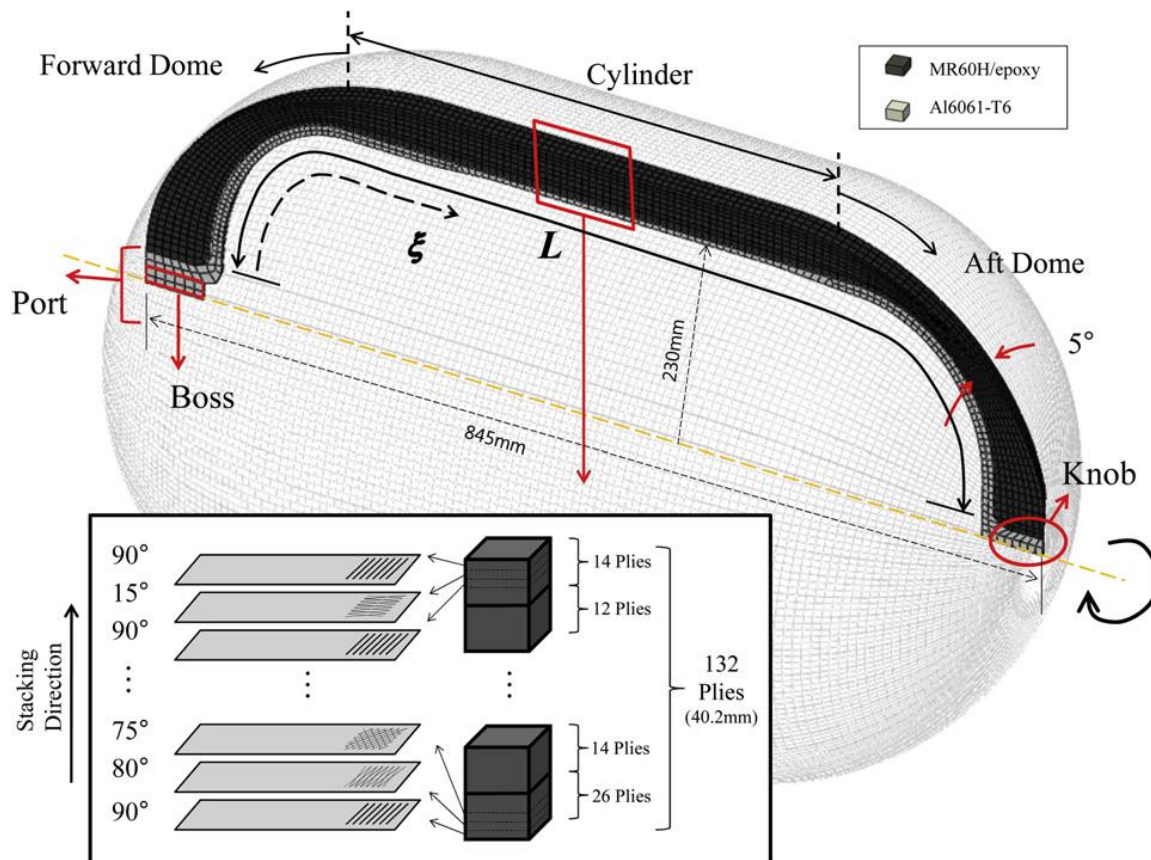


Figure 19: Finite element model of a pressure vessel used for hydrogen [21]

The results from FEA shows the pressure vessel will still be operating under safe conditions when the minimum burst pressure of 164.5 MPa is applied. This is due to the fact that this minimum burst pressure is 2.35 times greater than the service or working pressure of 70 MPa. Fracture will also not occur because the maximum stress of 314.9 MPa is less than the ultimate strength of 333.72 MPa for the aluminum liner.

Evaluation of hydrogen pressure vessel storage using FEA was similarly conducted by Xu et al. at Zhejiang University in China [22]. The idea was to create a lightweight high pressure vessel to be used as a fuel cell inside a vehicle. The cylindrical portion of the pressure vessel is constructed from 6061-T6 aluminum liner layer with 10

carbon fiber epoxy composite layers. This makes the yield strength 246 MPa and the tensile strength 324 MPa while the shear modulus is 600 MPa. Figure 20 indicates the results of an evaluation of the pressures inside the pressure vessel of 40 MPa, 80 MPa and 120 MPa based on the maximum failure stress criterion.

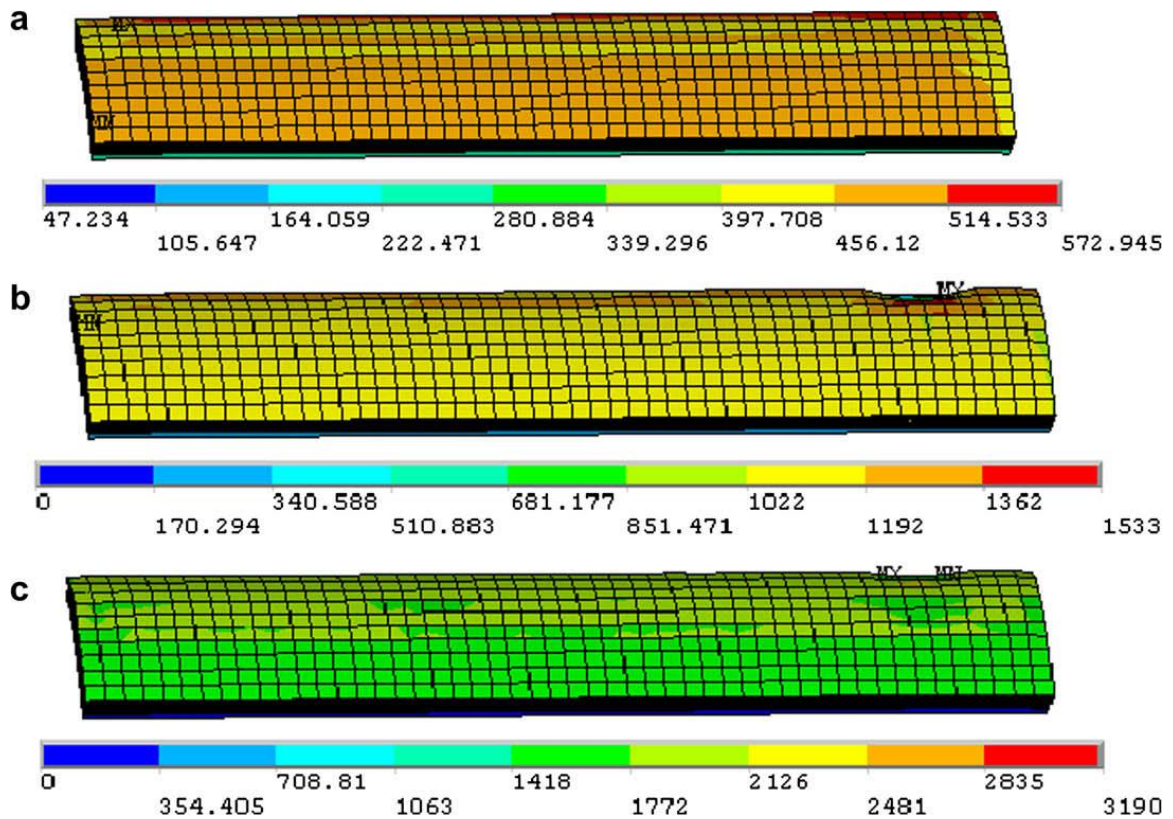


Figure 20: Illustration of the Von Mises stresses under the internal pressures (a) 40 MPa, (b) 80 MPa and (c) 120 MPa [22]

After analysis of the experimental results, a nonlinear relationship developed between the Von Mises stresses and the radial displacements. This was primarily due to the plasticity properties of the material as it began to fail due to the degradation of the stiffness of the elements of the carbon fiber/epoxy composite. It was determined failure occurred at 120.6 MPa under maximum stress. When the failure occurred, the test

A full size pressure vessel constructed from steel plate P355NL1 (EN 100283) was used for four structural comprehensive investigations regarding fatigue stresses were conducted. A pressure between 1 and 35 bars were applied during the experiments with a frequency of roughly 1 cycle per minute. The data obtained allowed for the generation of S-N curves which allowed for generation of untested points through extrapolation. These indicate precaution should always be taken when designing these S-N curves established by high cycle fatigue data to predict low cycle regimes through extrapolations.

FEA can be used to determine the strains for the optical windows of high pressure chambers. Soga, et al. used finite element calculations and holographic interferometry to accomplish this for internal pressures up to 483 bars (48.3 MPa) [24]. Two different shapes of windows were divided into grids and are shown in Figure 22 below.

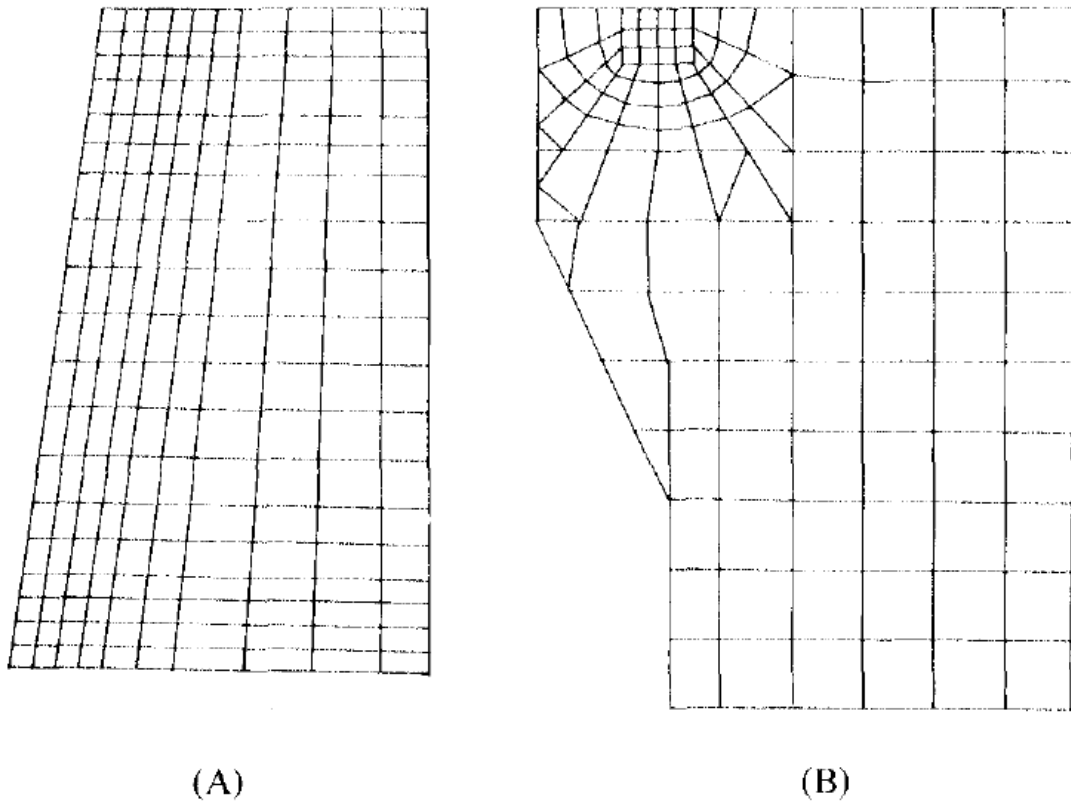


FIG. 4. Grids for windows (A) and (B) used in the finite element analysis.

Figure 22: Finite Element Analysis with grids for windows [24]

Window (A) was grounded on the conical surface side in order to achieve a contact which is uniformed at the end plate and connection to the bore surface. This window is a typical optical design made from fused quartz. Whereas, window (B) interfaced with the grounded face of the end plate, while using a thin Teflon sheet and a standard Neoprene O-ring which intersects with the internal surface of the pressure chamber. This window was fabricated from Pyrex glass.

This analysis revealed a small defect on the surface of the glass which would escalate to a high stress concentration point or worst, the origin of the development of a propagating crack. However, it would be difficult to determine the exact moment in time

when a failure would occur. But, in most cases a determination of a failure is all that will be required.

The related calculations for the windows in a pressure vessel design are critical by virtue of these locations are considered to be among some of the weaker areas for the design. To minimize failure, stress concentrations around a design with multiple windows were calculated. Some of the stresses include radical stress, hoop stress and yield stress. An article by Field and Kirkwood illustrates these calculations in abundant detail [25]. Figure 23 displays the cross sections for a 1 GPa cylindrical pressure vessel.

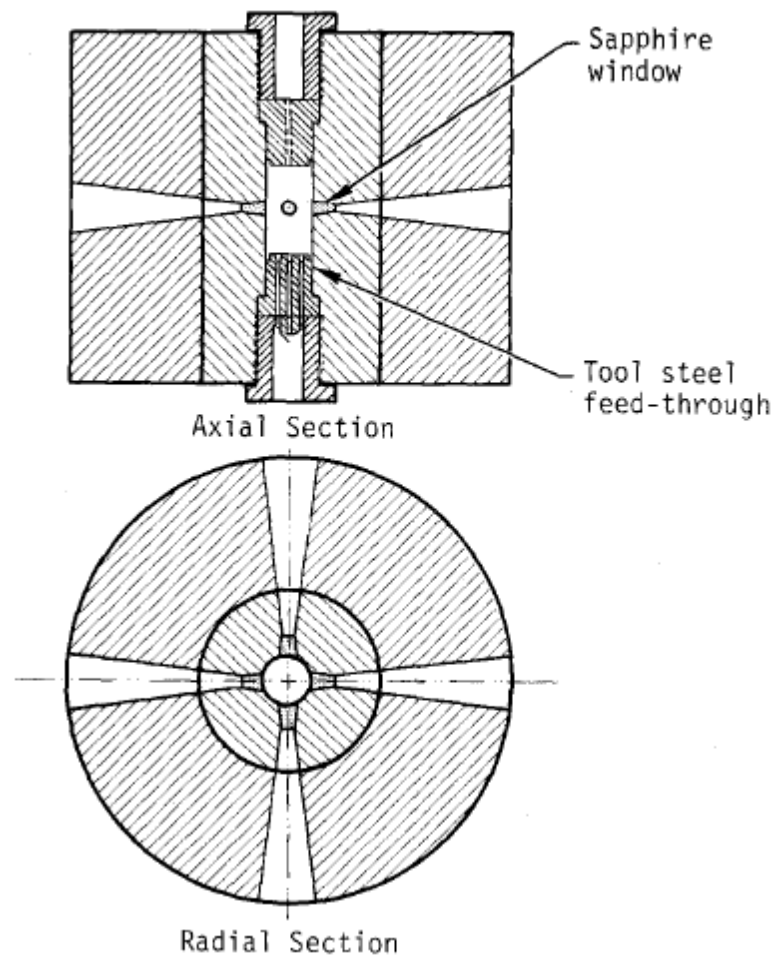


Figure 23: Cylindrical pressure vessel cross sections with four tapered sapphire windows [25]

Tapered sapphire windows were implemented due to its large compressive strength, flexural strength and Young's Modulus in order to obtain the test condition of 145,000 psi (1 GPa).

Soda lime glass, borosilicate, quartz, Fused silica, Sapphire and Magnesium fluoride were all tested as sight windows under high loads for mechanical designs. This was done by Ihracska et al. in August 2016 [26]. Based on the material properties of these optical materials, Sapphire exhibits the highest Young's modulus, Tensile strength,

Vickers hardness and maximum continuous operating temperature when compared to all previously listed materials. Figure 24 below shows the results when a simulated load was applied to a 3D model representing an optical viewing port. 144 mm is the internal diameter of the optical section while the external diameter is constrained by supporting rods.

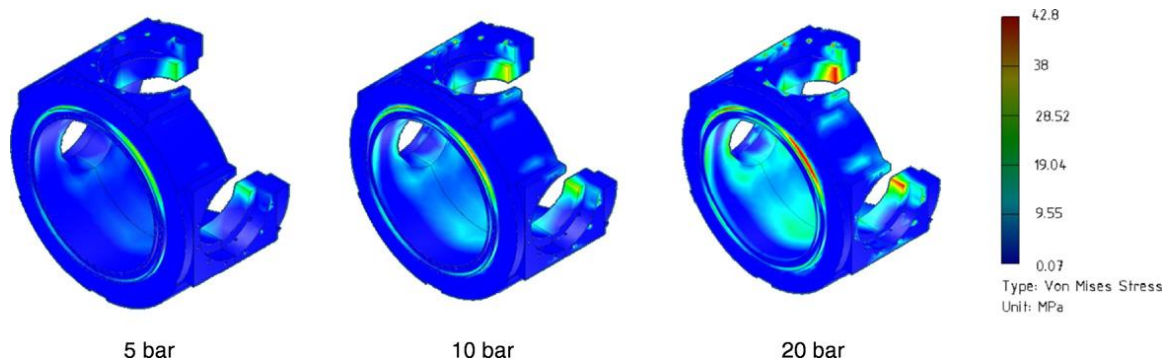


Figure 24: Illustration of stress distribution for optical design at 5, 10 and 20 bar respectively [26]

The results indicate more of the assembly experienced Von Mises Stresses below 19.04 MPa. As expected, the most Von Mises Stresses occurred when 20 bar (2 MPa) was applied. However, the largest stresses were observed at the intersection and sealing of the O-grooves and at the back near the opening. For the O-ring grooves, this is due to the size of the axial forces pushing on the contacting surfaces together against the pressure. However, the reduction of material volume and reduced inertia is the cause of the high stress rate of the back openings. Based on the materials properties previously described, three sapphire sight windows were used for the final design. The sapphire sight windows also positively contribute to increasing the safety factor of the entire design which normally varies between two and five depending on the operating, manufacturing and environment conditions.

In most cases, it is not efficient to build a physical representation of the desired research equipment without validation of a successful fabrication specimen. Technologies advancements in software allow for the evaluation of stresses in a 3-D model before resources are committed to producing a physical prototype. One of the most common ways is to conduct Finite Element Analysis (FEA). As stated in a thesis by Chen, this process can be used to optimize the design of an Ultra-High Pressure Vessel [27]. In FEA, the mesh density can be adjusted based on the desired application and memory resources. Finer mesh control selections tend to give a level of accuracy for illustration of the Von Mises stress as well as the overall displacement and strain values. This allows for a quick determination of structurally weak areas and areas with high stress concentrations. Most importantly of all, the determination of whether a product will fail can be established without it ever building a physical interpretation.

Guerrero et al. used these FEA techniques and methods to analyze fracturing in a high strength steel pressure vessel at the University of Oviedo in Spain[28]. High strength steel P500 with a yield strength of 500 MPa was used to evaluate the pressure vessel using FEA in the software ANSYS. After conducting a simulation with course mesh parameters, a crack appeared in the center of the sub-model and is shown in Figure 25. Boundary conditions were specific as the calculated displacement values were obtained by subroutines in ANSYS which also stated there were 48188 elements and 54858 nodes.

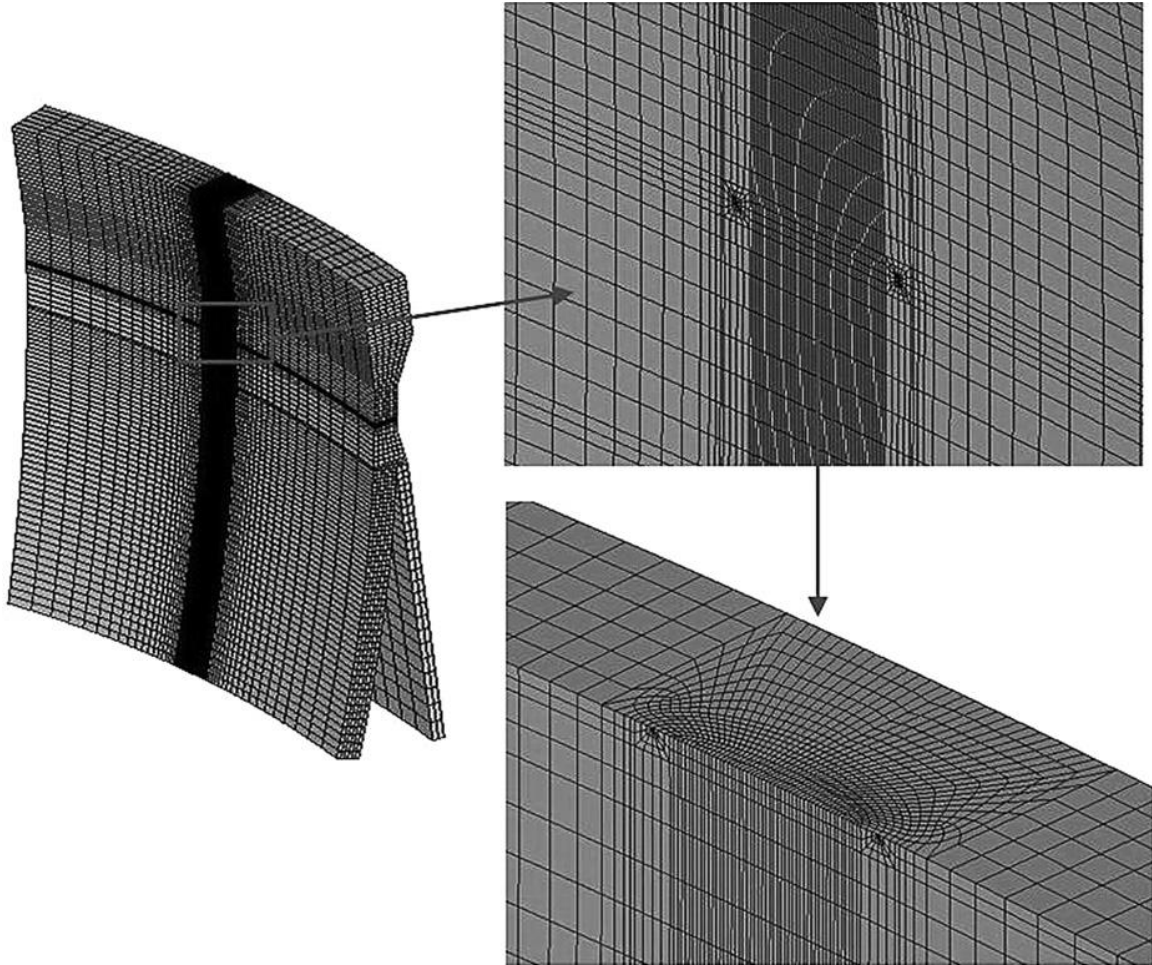


Figure 25: Course finite element sub-model meshing revealing center crack [28]

Although a worst case situation crack was revealed in the high strength steel pressure vessel, this did not endanger the safety of the pressure vessel during non-destructive experiments as it relates to fracture. This is because the stress factor maximum values were along the edge of the crack and were always lower than the toughness fracture of the material at room temperature circumstances.

2.5 Previous Research by Logan Garris

Prior research work was done by Garris at the University of North Carolina at Charlotte which involved the advanced manipulation using electric fields on electrospayed dielectric fluids [29]. Common commercially used 87 octane was the dielectric fluid which was charged as well as sprayed into a custom assembled chamber at atmospheric pressure and temperature. A Red Lake Motion XTRA HG-XR high speed camera capable of recording 1000 frames per second was used to capture the 87 octane which was triboelectrically charged and electrospayed after passing through 10kV. A compatible software referred to as Motion Studio was used to analyze the produced TIFF files. In order to measure the dispersion and droplet size of the fuel, a calibration of Motion Studio was first done by measuring the diameter of the test chamber and denoting this value in Motion Studio which was 118.3 mm. This measurement calibration is shown below in Figure 26.

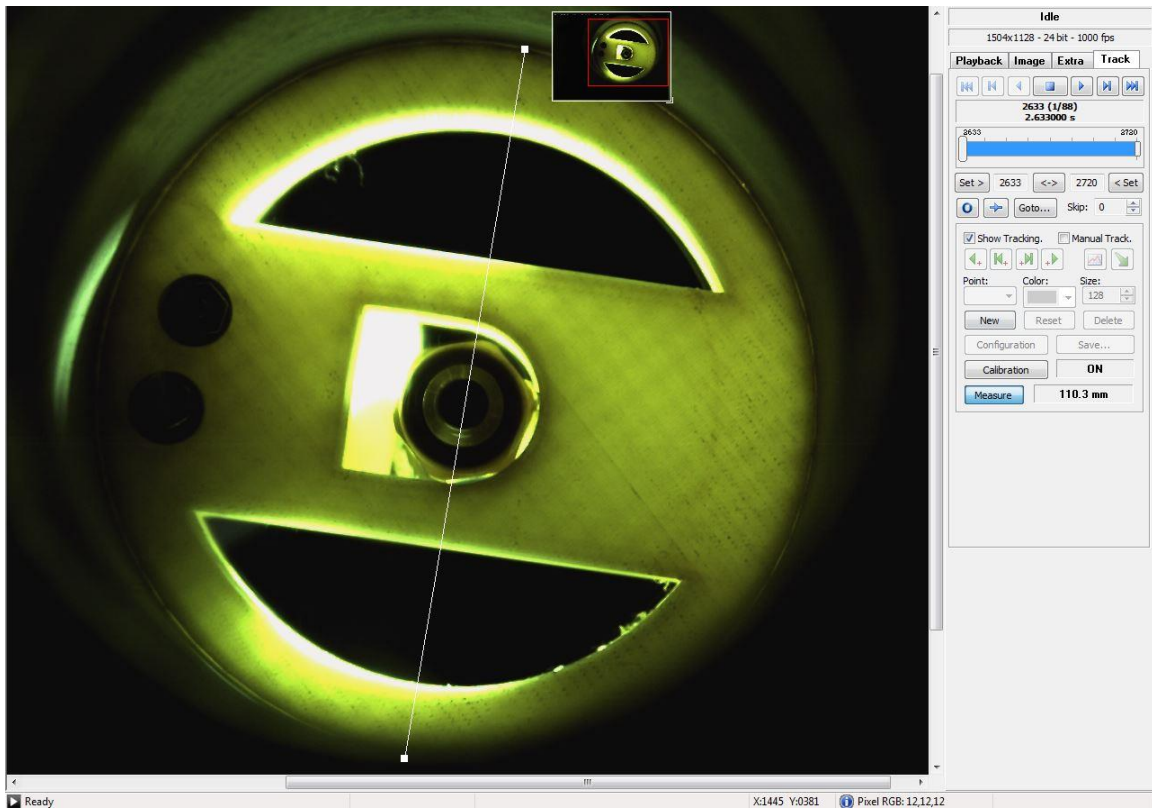


Figure 26: Image measurement calibration for fuel profile analysis [29]

After the calibration was completed and verified, the fuel dispersion for both the x and y directions were measured at eight equally spaced displacements away from the fuel nozzle as the 87 octane travelled downward. Test data was only recorded while the fuel was travelling in the top half of the chamber. This was because the top half of the chamber exhibited a negative charge while the bottom section of the chamber was grounded. This led to the determination that the 10kV applied electric field did not have an effect on the fuel dispersion or droplet size after the first segment of the experimental chamber. Figure 27 below displays the last measurement position taken for the experiments.

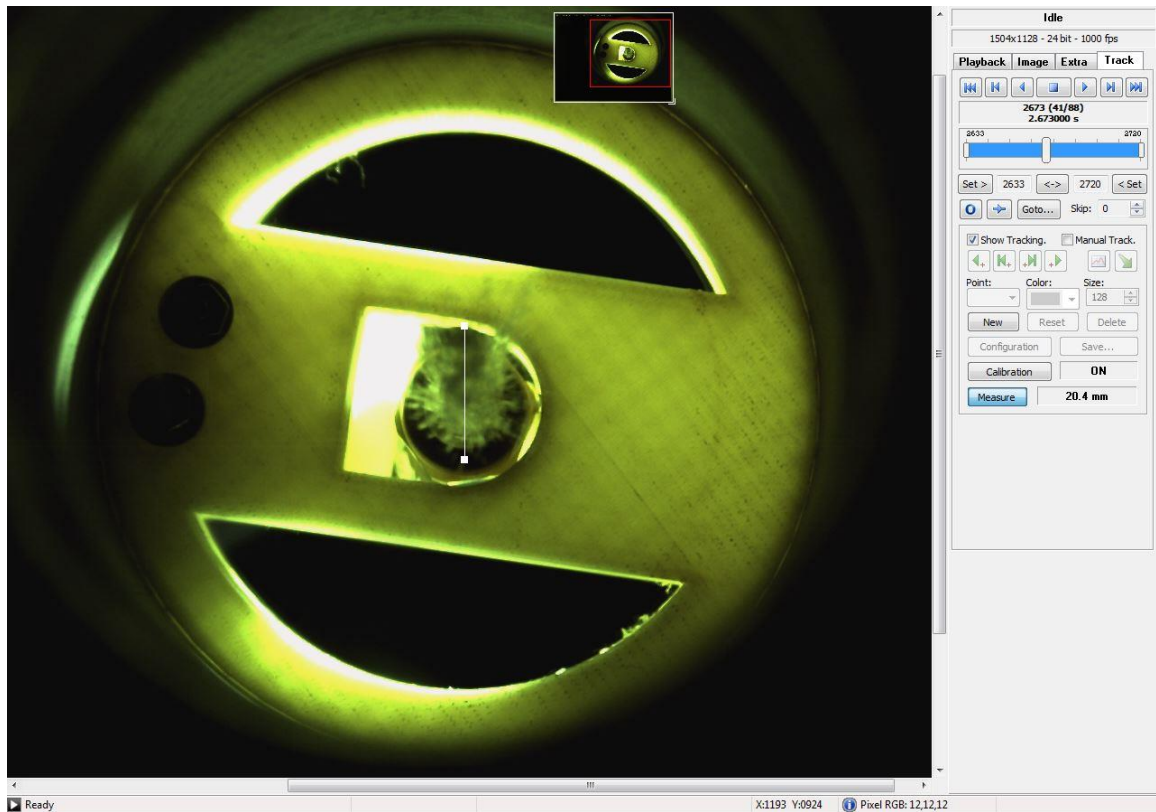


Figure 27: Y direction measure of fuel to determine the width [29]

This resulted in 16 data points for each of the four test experiments which were conducted. Two experiments were conducted with an electric field of 10kV being applied and the remaining two experiments were conducted with no electric field existing. Each applied electric field experiment immediately proceeded an experiment when no electric field was present. Figure 28 below illustrates a SolidWorks generated model for comparison of the fuel profiles between the non-electric field and applied electric field.

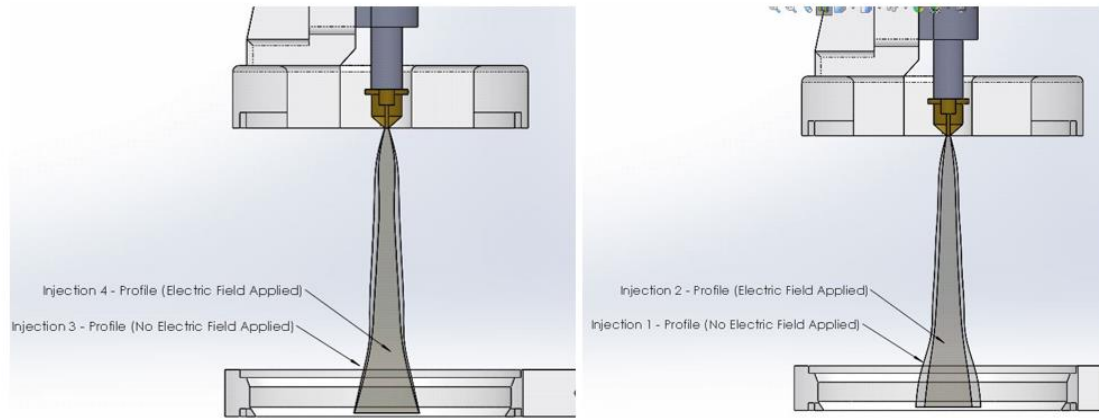


Figure 28: Fuel injection comparison with and without an Applied Electric Field [29]

A simulation investigation of the fuel profiles and the resulting particle trajectories was moreover conducted using COMSOL Multiphysics which is a 3-D modeling software capable of Finite Element Analysis (FEA). Simulations were directed using 50 randomly generated non-uniform droplet sizes with a confidence interval of 95% for the range of the deviated diameter related to the droplets. This was done to better resemble a real world arrangement of the droplet size and dispersion. The initial diameter sizes of the droplets were set to $5\mu\text{m}$ at atmospheric pressure. An electric field was generated in COMSOL Multiphysics by creating an alternating charge on the separated sections of the test chamber in order to repel the fuel droplets. The physics electrostatics functionality of COMSOL Multiphysics was employed to introduce an electrical charge to the cylinder wall. Based on the test data, injected fuel was simulated and tracing of fuel particles were conducted. The release point for the experiment when no electric field was applied was 0.25 meters which is illustrated in Figure 29 below.

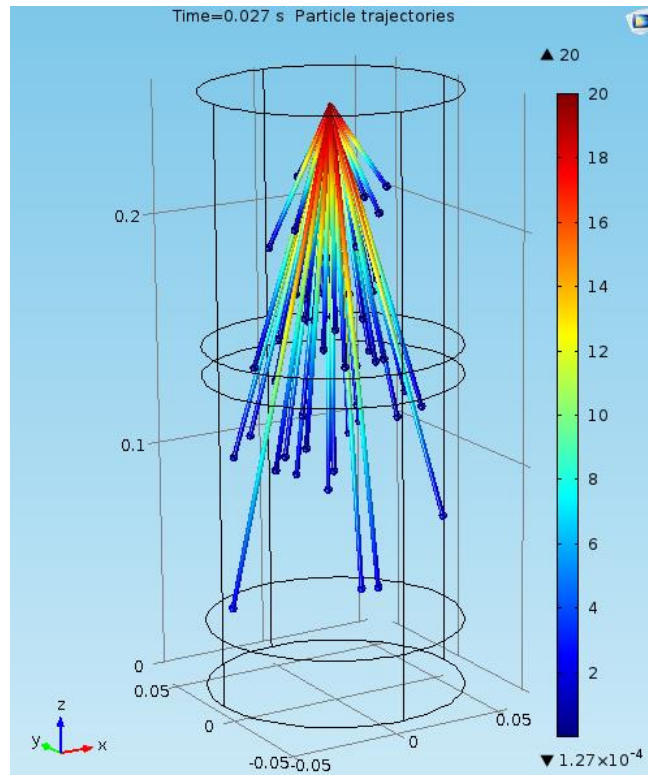


Figure 29: COMSOL model of fuel droplet particles without an Electrical Field Applied [29]

On the other hand, when an electrical potential difference of 10kV was applied a trajectory and penetration was observed after the same 27ms. The penetration increased from the previously observed release point of 0.25 meters to 0.15 meters. The result is demonstrated in Figure 30 below.

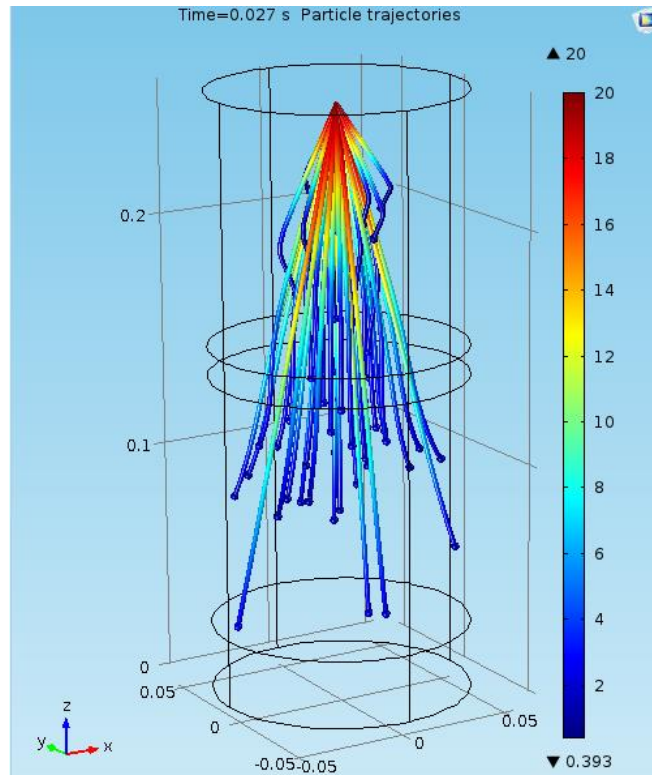


Figure 30: COMSOL model of fuel droplet particles with an Electrical Field Applied [29]

This simulation data illustrated the fuel droplet particles underwent some manipulation in both the x and y directions radially during the injection process due to the presence of the charge applied by the electric fields. These outcomes also conducted smaller fuel droplets were acted upon differently as compared to larger fuel droplets due to drag forces along with a depth change with and without an electric field applied. Penetration was increased and the fuel profiles were likewise narrowed when the 10kV was applied.

CHAPTER 3: METHODOLOGY

3.1 Entire System Overview

Previous experimental results concluded by Logan Garris from the prior test setup the largest charge value was achieved at 20 psi when experiments were conducted at 15, 20, 25 and 30 psi [29]. It was also determined between the two materials Teflon and Nylon, Teflon provided more electrical charge during tribocharging. Two experiments each with no electrical field and two with 10 kV applied were compared in Motion Studio. After the analysis of these four injections which occur under atmospheric conditions, the basic principles of fluid dynamics indicate the applied electric field had an effect on the droplets of the fuel in the horizontal direction. This affect was observed with minimal charge increase from tribocharging.

However, the conditions inside of a typical internal combustion engine are very different than the environment of the experiment research. Even though, the fuel particles adhered to some manipulation from the applied high voltage electric fields. The development of a system which more precisely replicates the environment experienced inside an internal combustion engine especially as it relates to higher pressure. This will allow for a better assessment of the technical efficacy for engine applications.

It was determined that the best way to examine whether electro spraying using tribocharging, similar research must be conducted with comparable parameters experienced inside an internal combustion engine. The most significant environmental change will have to be an increase in pressure. Figure 31 below illustrates a 2D drawing on the entire system overview which was done in Microsoft Visio.

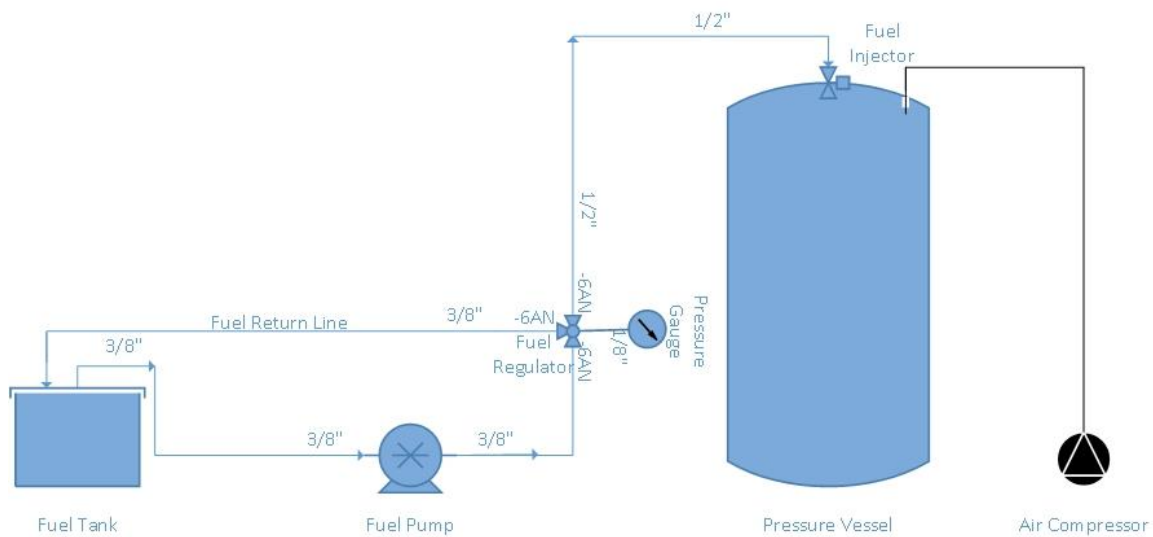


Figure 31: Entire System Overview

3.2 Pressure Chamber Design

In order to conduct further experiments at elevated pressures, a pressure chamber would be required or an enclosed vessel capable of controlling and maintaining high pressure with safety precautions. Although suitable for atmospheric research, the Logan Garris test setup was not adept to confining internal pressure. However, the general principles from the Logan Garris research were to be sustained for comparison of the droplet control due to the high voltage electric field between atmospheric pressure and elevated pressure. This would also mean the fuel delivery and fuel injection systems will have to be modified which will be detailed later in the methodology.

The procedure for constructing a pressure chamber was to begin with conceptual designs. Due to the fact that at this initial interim the design is fluid and changes are to be expected, a Computer Aided Design (CAD) software capable of 3D design and simulation analysis was to be employed. Based on the prior information from the literature review, numerous researchers used a program called ANSYS. However, due to familiarity and availability, the program SolidWorks is more than proficient in performing any required functions related to conceptually designing a pressure vessel. Simulations were executed on assembly files after all of the geometries for the component parts were constructed and mated. At this point, different stresses were evaluated and determined to ensure the structural integrity of the pressure vessel with all area on the assembly well below the failure criterion. A review of the most favorable simulation results were proceeded for cost and manufacturing consideration.

3.2.1 Parr Instruments Design

Multiple vendors were approached with conceptual designs for the construction of a pressure chamber. The first receptive companies which showed interest in the idea of designing a suitable pressure chamber for the experiment was Parr Instruments Company located in Moline, Illinois. Parr Instruments Company specializes in production and custom reactors. Correspondence was conducted with Donna Knouse at Parr Instruments Company [30]. The best design which was achieved by this approach was to modify an existing production line pressure reactor. This would save time in the construction on a verified and proven design. The N4666-T-SS would be modified to include two 0.62" by 3.5" fused silica windows rated at 1900 psi with 1/2" NPT fittings for viewing and the entrance of light 180° apart as well as two removable heads at either end for ease of access to the interior. This pressure reactor would be made out of T316 Stainless Steel and operate at a maximum work pressure of 1900 psi while at a maximum temperature of 225°C. The top head of the reactor would be fitted with a 1/4" NPT fitting and installed external nozzle to allow for fuel flow into the pressure reactor. This custom removable top head would also include a safety rupture disc rated for 2000 psi and a pressure gage which displays pressures from 0 to 2000 psi. A Type J Thermocouple would also be used to monitor the internal reactor temperature. Internal wetted parts would also be used to interface with both removable heads and the cylinder for all other pressure sensor components and potential direct contact surfaces. The bottom head of the reactor would contain a split ring closure for the housing of another fused silica window 4" in diameter for viewing and observation of the experiment. Typical gas inlet and outlet valves were intended to be used for the pressurization and depressurization of the custom reactor. The

final fixed cylinder internal dimensions are 6" in diameter and 36" in depth. All of these specifications except the removable bottom head with the 4" viewing fused silica window are displayed below in Figure 32.



**2000 mL Stirred Reactor with
Two Elliptical Quartz Windows**

Figure 32: Parr Instruments Custom Reactor Design [30]

In addition to the custom reactor, there would be a few suggested equipment. Due to the fact that the custom reactor would weigh over 150 lbs., it is advised to use a special fixed vessel floor stand to ensure the custom reactor is vertically upright positioned at all

times. This floor stand would contain a pneumatic lift to vary the height of the custom reactor at time. Another useful component which would aid in this setup is a 230 Volt flexible heater. This heater would wrap around the custom reactor leaving the windows exposed. This would help in maintaining a constant temperature for the entire reactor to prevent condensation on the fused silica windows for optimum viewing. In order to control the flexible heater, a ramp and soak programming Proportional Integral Derivative (PID) controller with a voltage rating of 230 volts was intended to be used. Spare and optional parts were also discussed and it concluded as a precaution, three extra PTFE flat gasket split ring closures should be considered for the top and bottom head openings on the custom reactor. All of the equipment resulted in a quote estimated total price of \$45,192 and a lead time of 7-8 weeks After Receipt of Order (ARO). For further information about the quote of the custom reactor from Parr Instrument Company refer to Figure 72 in Appendix A.

After careful consideration, it was determined that the possibility proposed by Parr Instrument Company exceeded the budget for the research project and did not give sufficient flexibility in relation to mounting of electrodes and possible future combustion and high pressure nozzle fuel injection. Based on the design requirements and the useful information acquired from Parr Instruments Company, a more custom design was developed as illustrated in Figure 33.

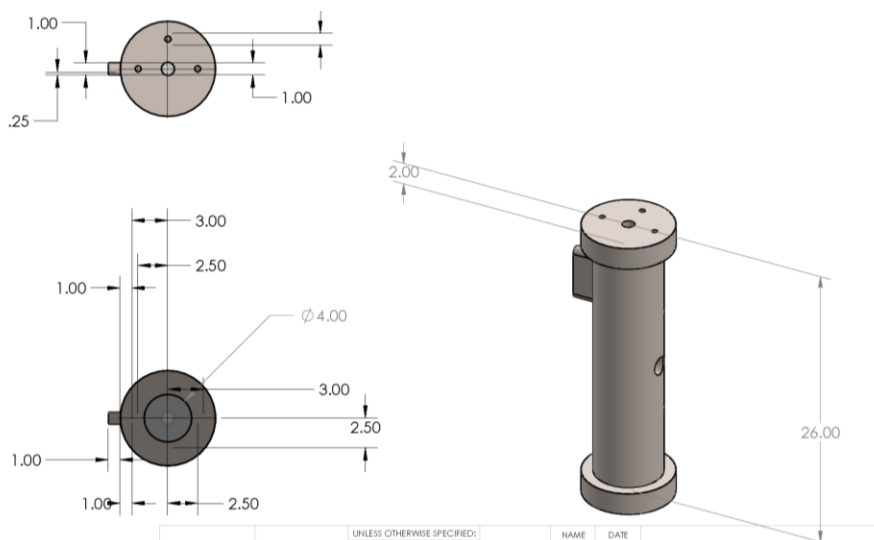


Figure 33: Initial Cylindrical Pressure Vessel Design

The above design includes a removable cylindrical top with three ports of access each $\frac{1}{4}$ " in diameter and 1" away from the center. One port was for the connection of high voltage to produce an electrical field inside the chamber. Another port would have been used for pressurization and depressurization of the pressure vessel. The final port was for the attachment of a pressure gauge to determine the pressure inside to vessel. The center open was for the installation of a nozzle to injection 87 octane in the chamber. The base of the chamber would not be removable but contain a 4" diameter fused silica window for viewing the fuel as it travels downwards after leaving the nozzle and conducting analysis. Another fused silica window was to be mounted on the side of the pressure chamber with a size of 0.62" by 3.5" to supply light inside for the accommodation of electrospraying investigation. Finally, there was an addition of a 0.55" diameter hole for the possibility of mounting a spark plug to manipulate ignition of fuel.

3.2.2 Australian Maritime College Design

As previously described in chapter two of the literature review above, Goldsworthy et al. of the Australian Maritime College in Launceston, Tasmania have executed diesel spraying in a high pressure chamber [17]. Based on this research, it was deemed a pressure chamber with similar accommodations would be applicable for the desired investigations. The pressure chamber design was then modified to be a 24" long by 6" inside diameter with thickness of 0.60" square. The large oblong windows were designed with a length of 18" and a half circle arc of 0.63" for the viewing area. All four corners chamfer of the pressure were chamfered with a radius of 0.91". These were designed to decrease the number of sharp edges and therefore, reduce the forces applied at these high stress positions. However, due to the chamfering of the inside bottom surface this resulted in shrinking the window length to 14". The removable top lid contains four ports each 0.25" in diameter as well as a center opening 0.55" in diameter for the installation of a fuel injection. Figure 34 below shows the representation of the positioning of a pressure gage and a rupture disc. The other two ports are for the installation of an air intake and outlet as well as an electrode placement. On the back of the pressure chamber there is a port for the connection of a spark plug.

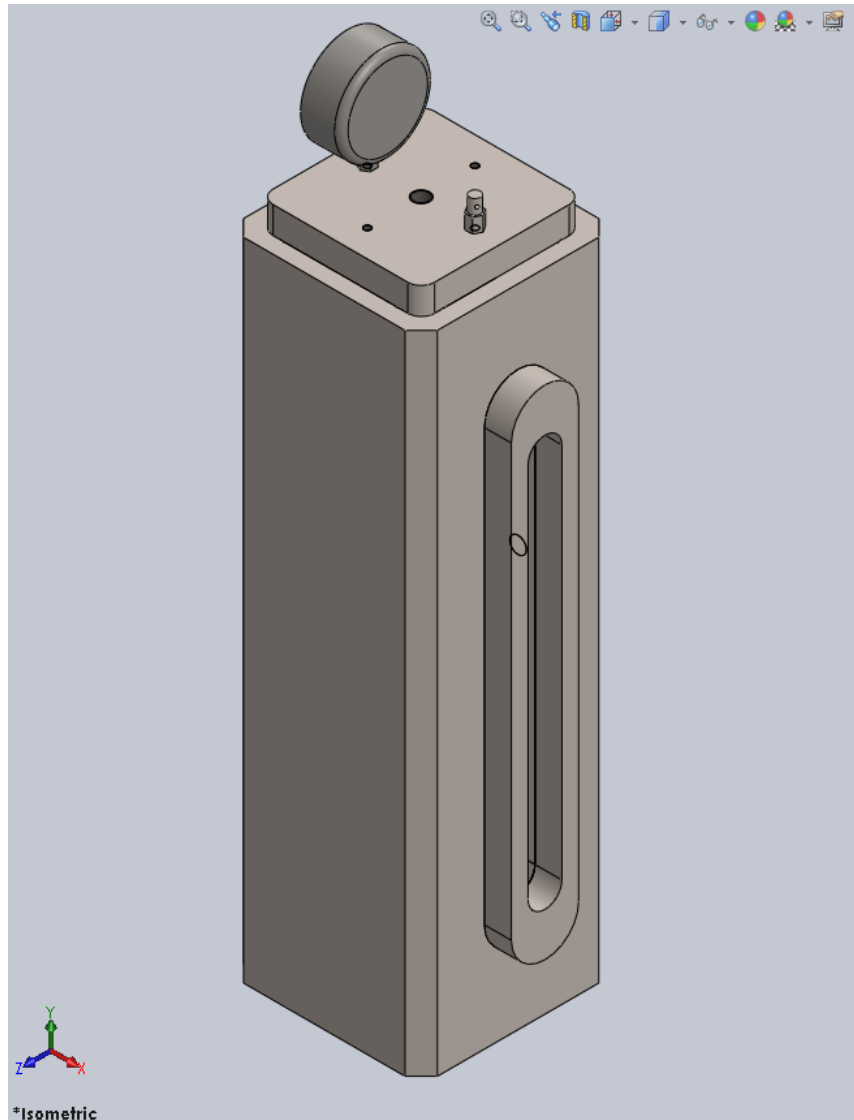


Figure 34: Pressure Chamber Design based on Research from The Australian Maritime College

A Finite Element Analysis (FEA) was simulated on the pressure chamber which resulted in the von Mises stresses. The bottom surface of the removable lid was attached to the top surface of the pressure vessel with a rigid connection. The window welds were to be rigidly connected to the body of the pressure chamber while the fused silica windows were simulated to be fixed inside the window welds. The bottom surface of the pressure vessel was edited to represent a fixed connected as if to be resting on a floor or

immovable surface. A pressure of 6 MPa was applied to all of the interior surfaces including the welded window housings, the fused silica windows as well as the bottom surface of the removable top lid. This resulted in a maximum and minimum von Mises stress of $4.851 \times 10^8 \text{ N/m}^2$ and $9.969 \times 10^1 \text{ N/m}^2$ respectively and a deformation scale of 87.8255 below in Figure 35.

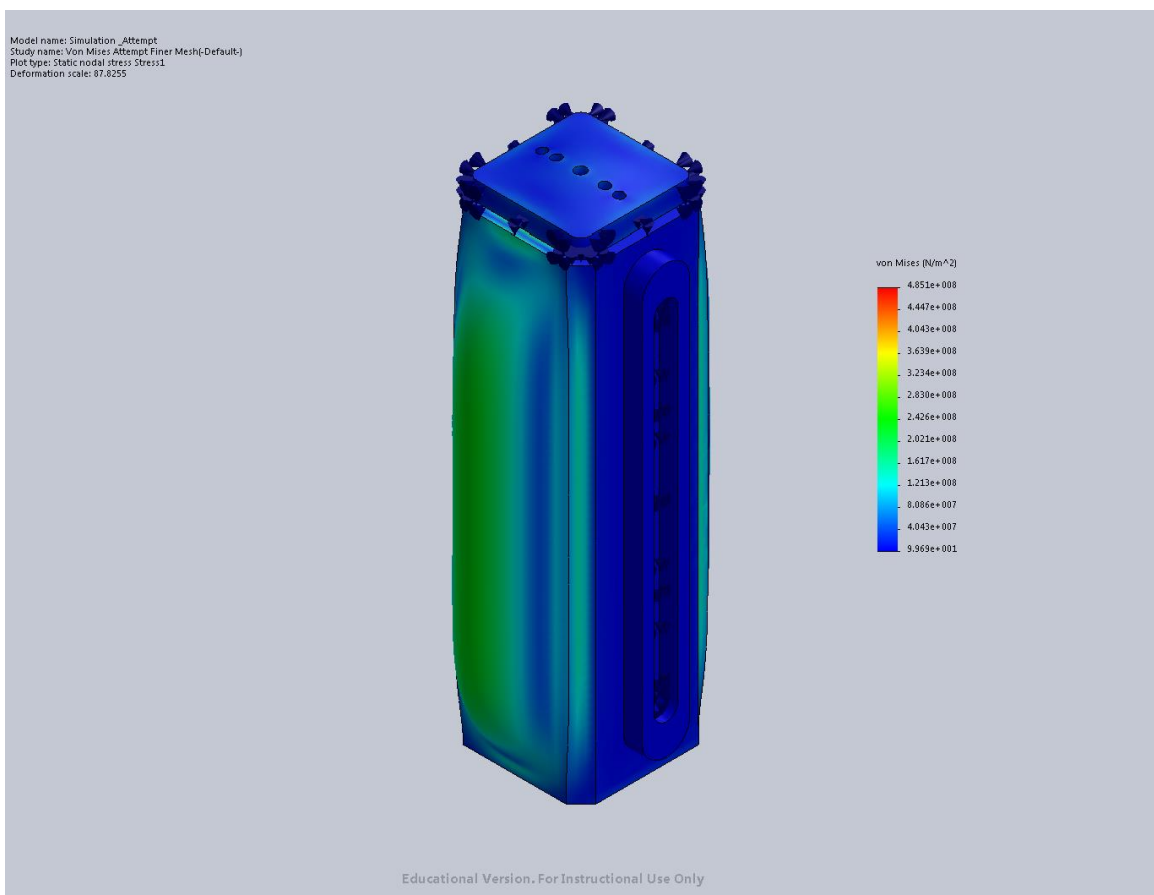


Figure 35: Von Mises Stress Simulation

However, there are some concerns with this approach of the pressure vessel design. There was an intent to use integral fused silica or sapphire windows which are both rated at 1900 psi while operating at a maximum temperature of 225°C. There was also a plan to construct the pressure vessel out of a solid block of AISI 316 Stainless

Steel. This would result in milling 24" in depth. Both of these concerns will severely increase the total cost of the final pressure vessel design. Due to these factors this approach was no longer pursued and further designs were explored.

3.2.3 Sight Glass Design

Due to the above concerns and budgetary restrictions, the design was modified to reduce the cost while maintaining the requirements of the pressure vessel. Instead of large oblong fused silica windows, there was a modification to instead install seven sight glasses. Three sight glasses on one face of the pressure vessel while, four sight glasses on the face which is 180° opposite. Even though this diminishes the visibility area inside the pressure chamber, this supplies a substantial reduction of cost because sight glasses are commercially available. The pressure chamber would be made out of three pieces instead of two with the material changed from AISI 316 Stainless Steel to Aluminum Alloy 6061-T6 which is less expensive. There was a manufacturing decision made to increase the internal size from 6.00" to 7.00" and decrease the thickness from 0.60" to 0.50". This was done because 7.00" inside diameter with an outer diameter of 8.00" is a standard commercially sold bar size which therefore avoids the cost of buying or manufacturing a custom aluminum bar. Due to the increase in bar size, the surface fillet radius was also increased from 0.91" to 1.00". The aluminum was to sit in a square base of 8.00" inside diameter and a 9.00" outside diameter. The removable top lid remained the same with the previously specified ports with overall length remaining unaltered. Figure 36 shows a visible depiction of the pressure vessel.

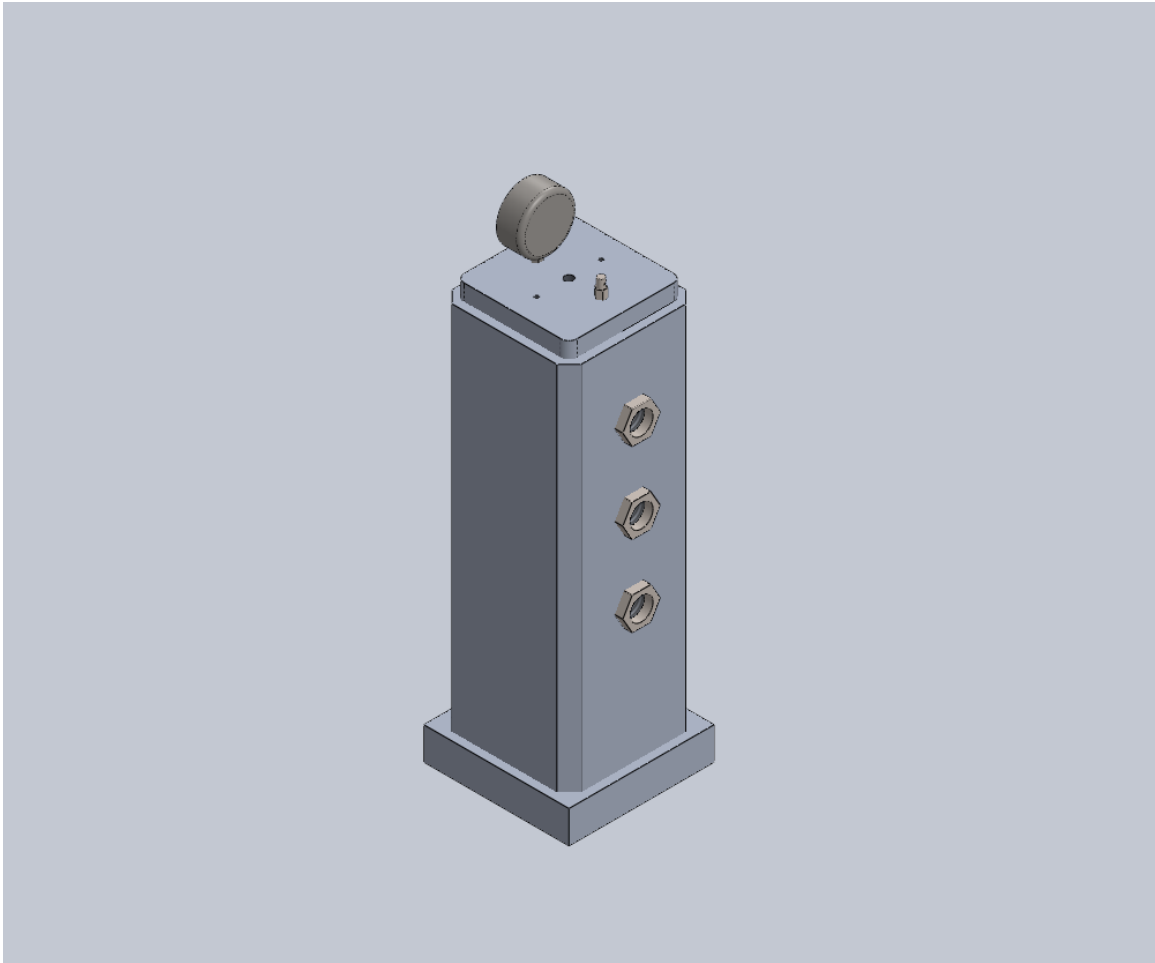


Figure 36: Aluminum Alloy Sight Glass Design

Even though Aluminum Alloy 6061-T6 has a lower tensile strength than AISI 316 Stainless Steel, it is still more than capable of operating a 6 MPa with the above specified design criterion. Figure 37 shows a SolidWorks simulation of a model assembly for the aluminum pressure chamber with sight glasses.

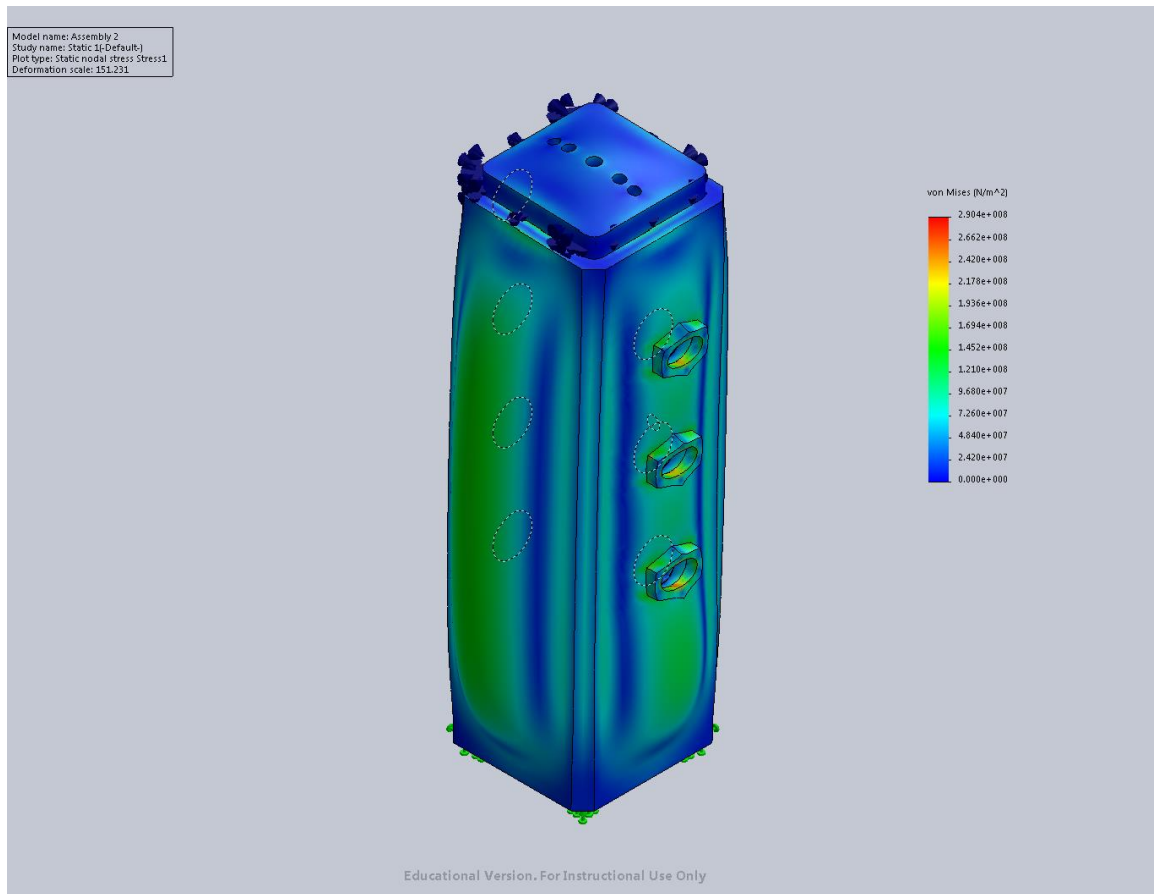


Figure 37: Aluminum Sight Glass Simulation

It is observed that the von Mises stresses are between 0 and $2.904 \times 10^8 \text{ N/m}^2$ on a deformation scale of 151.231 . These are lower than the von Mises stresses noted in the previous AISI 316 Stainless Steel design which are between $9.969 \times 10^1 \text{ N/m}^2$ and $4.851 \times 10^8 \text{ N/m}^2$. This is perhaps due to the configuration of the sight glasses and the decreased viewing surface area.

However, there are still some disadvantages to this pressure chamber design. One being since the pressure chamber has a non-removable base made out of a different piece of 6061-T6, this base will have to be welded to the body of the pressure chamber. Since

the material is Aluminum alloy, this requires a special welding process which will increase both the cost and lead time for the pressure chamber.

3.2.4 Cylindrical Design

After contacting numerous companies regarding the construction of the above pressure chamber design, there were no suitors. It was stated that most companies do not construct square or rectangular pressure vessels which operate at a working pressure as high as 6 MPa. Meanwhile, other companies do not build pressure vessels in any shape other than spherical or cylindrical. This was due to the fact that the forces experienced by a square pressure chamber would be higher than the forces experienced by cylindrical pressure chamber. This relates to the geometrical configuration of both designs. Even with filleted surfaces where edges of the corners interact the forces are still greater. Whereas, cylindrical pressure vessels have less flats surfaces and the forces tend to follow the spherical shape resulting in more evenly distributed forces which lower the stresses concentrations. This led to the design layout in Figure 38 below. The cylindrical designed was outlined to retain the same dimensions from the previous design. A constant overall length of 24" and an inside as well as outside diameter results in values of 7.00" and 8.00" respectively. The seven holes of 1.50" for the sight glasses remained unaltered with the existing 0.55" diameter hole for a spark plug. The removable top lid with a diameter of 7.00" and 1.00" thick still contained all four ports for electrodes, a pressure gage, a rupture disc and an air inlet and outlet which are 0.25" diameter. The 0.55" fuel injector slot remained unchanged. The body of the pressure chamber will sit in a base with an inside diameter of 8.00" and a thickness of 9.00". This spherical base will have a total length of 2.00" and a carved indentation at the 1.00" depth. The body of the pressure vessel will then be welded to the base to form a secure connection.



Figure 38: Plain Carbon Steel Pressure Chamber Model

The material for the pressure vessel was changed from the Aluminum Alloy 6061-T6 to Plain Carbon Steel. This was done to increase the strength but primarily to use a more commercially available material for the pressure. This was due to the fact that even though the SolidWorks models and simulations confirmed that the design was adherent to safety concerns, potentially manufacturing companies did not feel comfortable providing a quote for a pressure vessel of these dimensions at a pressure of 6 MPa made out of Aluminum Alloy. After these changes, the pressure vessel underwent another round of simulations and stress analysis as represented in Figure 39.

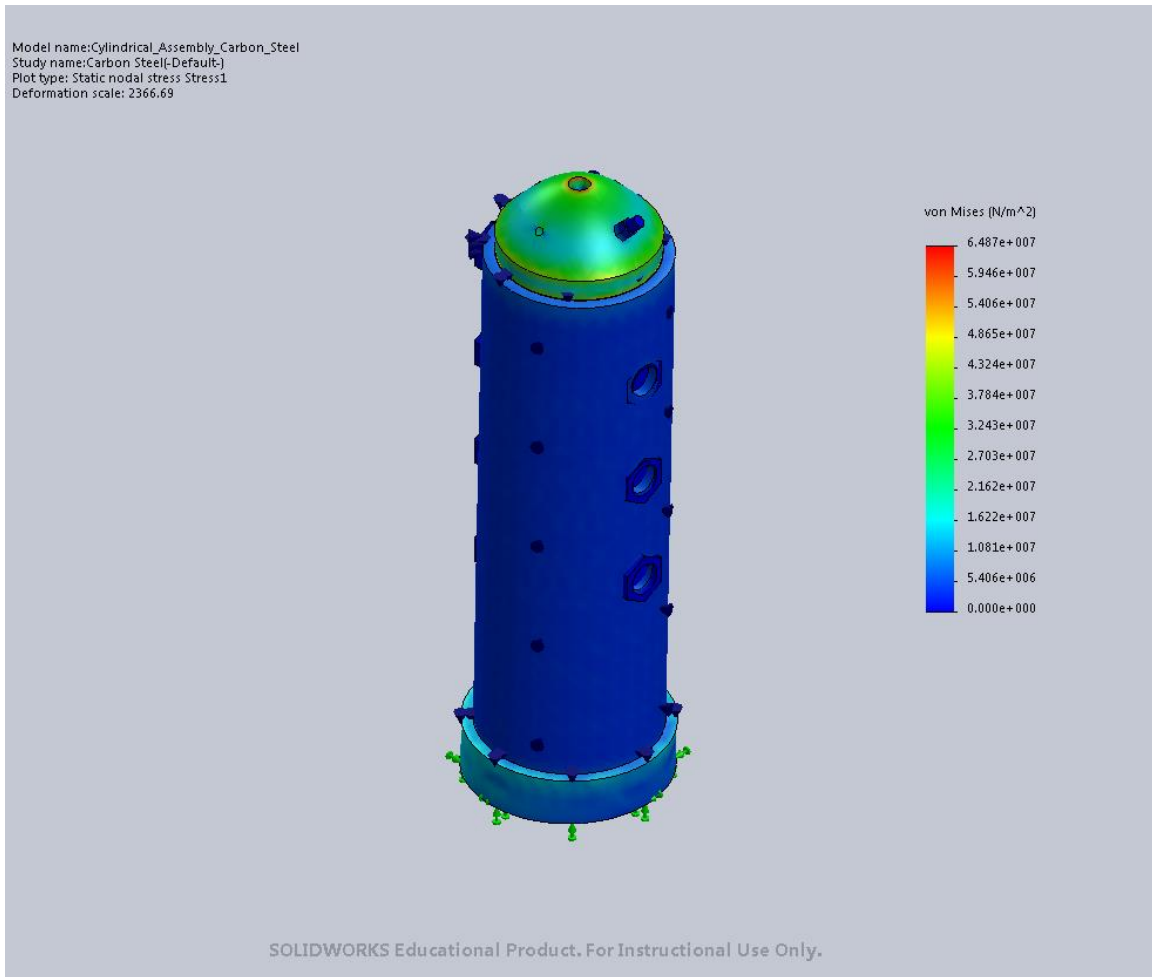


Figure 39: Plain Carbon Steel Pressure Chamber Simulation

Solid works simulations indicated the von Mises stresses were less than both the previous design iterations. The range of the von Mises stresses were between 0 and $6.487 \times 10^7 \text{ N/m}^2$ and is displayed on a deformation scale of 2366.69. The material selection of plain carbon steel definitely has an impact on the stresses but not as much as the change from a square to a cylindrical geometry. This is because there is a factor difference of about ten when comparing the von Mises stresses for both the Aluminum Alloy 6061-T6 and the AISI 316 Stainless Steel.

3.2.5 North Carolina Administrative Code

After communications with numerous companies regarding a quote for the modified cylindrical pressure vessel design, most companies were still hesitant in the design and were not willing to provide a quote. A few cited the administrative rules as it relates to the administrative codes in the state of North Carolina. The North Carolina Department of Labor list many General Statutes as it is associated to boilers, pressure vessel and safety while in operation. The Uniform Boiler and Pressure Vessel Act of North Carolina which is Chapter 95, Article 7A and 7B was referenced in regards to the pressure vessel design [31].

Due to the fact that the application of the pressure vessel is for research and experimentation, there was a consideration that these general statutes would not apply. However, since the manufacturing will be outsourced to an external company which is required to follow these general statutes, a pressure vessel must not be constructed outside of these administrative codes. Chapter 95-69.16 states these codes are enforced by Boiler and Pressure vessel commissioned inspectors, who determine the frequency and method of inspection. The commissioned inspectors have the discretion to determine whether hazard level and to ensure public safety will be adhered to at all times. At which point, a boiler or pressure vessel will be issued an inspection certificate and can be operated freely under safe and responsible conditions. Boilers and pressure vessels should only be operated under an owner-user provisions where safety and competency are met under the administrative procedures which are approved by the Board and Commissioner if the boiler or pressure vessel does not follow the inspection certificate. Based on Chapter 95-69.19 and Chapter 95-69.20 violations and civil penalties can range from a fine between

\$250 to \$500 all the way up to a Class 2 misdemeanor for willfully providing misrepresentation or knowingly making a false statement.

Chapter 13 NCAC 13.0504 in Article 7B states the guidelines for the Factor of Safety for both Boilers and Pressure vessels. The Factor of Safety is four and one-half for nonstandard boilers. However, there is an exception for boilers which are horizontal-return tubular and are more than twelve feet in length with a continuous longitudinal lap. In this case, the Factor of safety should be a minimum of eight. There is also a Factor of Safety of six established for lap-riveted longitudinal seamed nonstandard boilers with a length less than twelve feet. Butt and double-strapped longitudinal seams for a nonstandard boiler must have a Factor of Safety of five. A Factor of Safety of four is applied to nonstandard pressure vessels. The Factor of Safety of two is applied to non-ASME code storage hydro pneumatic tanks with water under ambient conditions.

Nevertheless, Chapter 95-69.10 in Article 7A does list exemptions to the article based on the application. Point eight of this article does contains some limitations based on the size of the pressure vessel and are not equipped with a quick actuating closure. The first limitation is the pressure vessel must contain five cubic feet in volume and 250 psig which is about 1.7 MPa. The second limitation is for a gage pressure of 350 psig which is approximately 2.4 MPa while the pressure vessel maintains a volumetric measurement of three cubic feet. Once the volume of the pressure chamber is less than one and one-half cubic feet with a gage pressure of 600 psig which is about 4.1 MPa the qualifications for limitation three will be achieved. The final limitation is on the size of the inside diameter which is six inches with no maximum sustained pressure.

3.2.6 Final Pressure Chamber Design

Once the Uniform Boiler and Pressure Vessel Acts of North Carolina were reviewed, the pressure vessel design was modified to represent the final iteration to be constructed. The two major changes which occurred was the editing of the dimensions of the entire pressure vessel as well as the reduction of functioning pressure. These key modifications were done primarily to accommodate the general statues listed above. This lead to the inside diameter being decreased from 7.00" to 5.50" to ensure that the inside diameter was less than six inches to comply with the fourth limitation above. Even though there are no pressure restrictions for this limitation, the maximum working pressure was still reduced from 6 MPa to 3 MPa. This was done to verify that the third limitation was also meet by operating at a pressure of approximately 435 psi. The design includes the change of material back to AISI 316 Stainless Steel from plain carbon steel. This was done because AISI 316 Stainless Steel is more readily available commercially and used more frequently by manufacturing companies which lowers the price.

Bosses were also added to the hole on the body of the pressure vessel. This was done to increase the thread count for the mating surface to provide a tighter seal when the sight glasses are installed. The sight glasses are high pressure fused pipe Thread, open view with a sight diameter of 1-7/16". The thread sizes are 1-1/2" with an overall length of 1.22 decimal inches. The sight glasses are also classified as a head type of two inches. Two flanges with eight holes of diameter 0.25" each were mounted to the top and bottom of the stainless steel bar. These flanges are attached together by connecting rods of the same size which travel down the length of the pressure vessel. The bottom attachment of a dome shape was butt welded to one end of the pressure vessel to form a base. An extra

port hole was added to the removable top lid. The configuration of the top lid now includes four holes with a 0.25" diameter thru and is threaded all the way thru with a size of 1/4-28 UNF – 2B thru. These ports support the connection for one pressure gage, the mounting of electrodes, air inlet and outlet and two rupture discs just in case one fails. There is also one unthreaded thru hole of the same of 0.25" diameter. Figure 40 shows an isometric model view for the design of the pressure vessel.



Figure 40: Final Design of Pressure Vessel Model

Initially, the top lid was designed as a dome shape to increase the manufacturability. However, this approach was not viable because of the mounting and installation of the fuel injector. Figure 41 shows a sectional view which is cut directly in the center from the right plane. The top lid sits inside the pressure chamber body 0.50"

below the surface of the bar for the body with a 5.45” diameter. The fuel injector rests inside a counter bore hole with diameter 0.52” thru \perp diameter of 0.60” and thru 0.58”.

This configuration allows for the very tip of the fuel injector to be approximately 0.2” above the first sight glass.

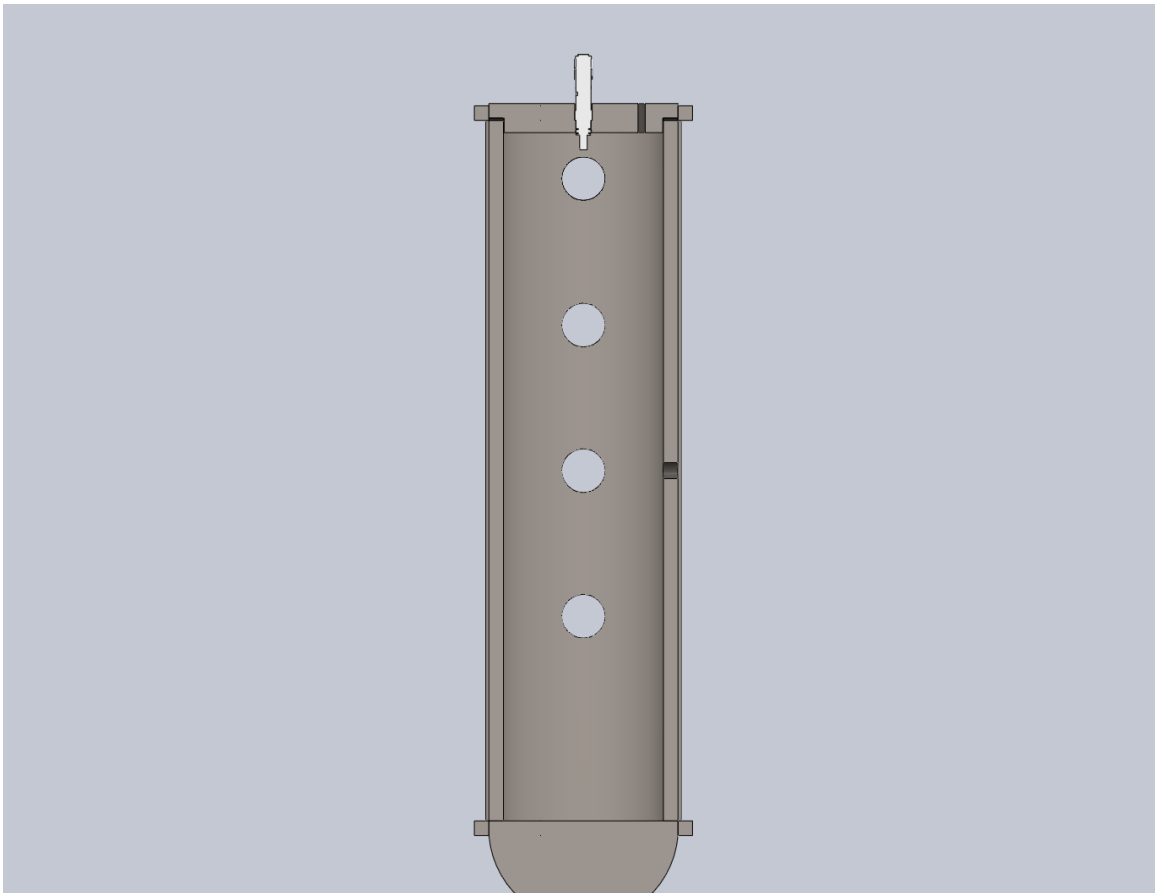


Figure 41: Cross Sectional View of Final Pressure Vessel Design

Even though the pressure was decreased to 3 MPa, the simulation studies in SolidWorks were still conducted at 6 MPa. This was done to increase the factor of safety for the pressure vessel. The von Mises stresses ranged between the values of 2.968×10^3 and $2.280 \times 10^7 \text{ N/m}^2$ on a deformation scale of 22108.9. The stress study in Figure 42 below was conducting at the default mesh setting which is approximately in the

middle between the coarse and finer indicator. For further information on the features on dimension of this pressure vessel refer to Figures 73 to 77 in Appendix B.

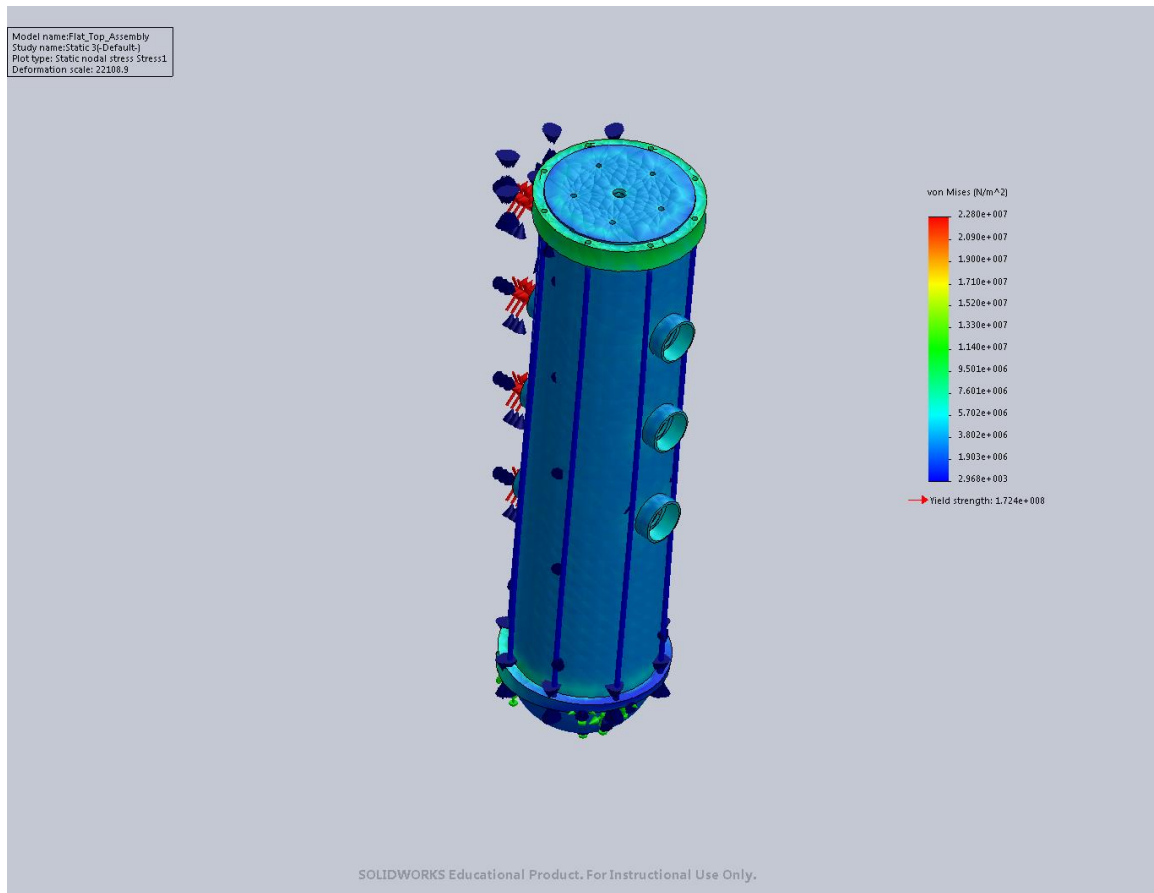


Figure 42: Final Design von Mises Stress Default Mesh

Figure 43 below shows the exact same von Mises stress simulation as above with the only difference being the mesh setting. The mesh setting was tuned to the finest possible value on the slide indicator. This resulted in von Mises stresses between

7.996×10^2 and $1.743 \times 10^7 \text{ N/m}^2$ on a smaller deformation scale of 15912.9.

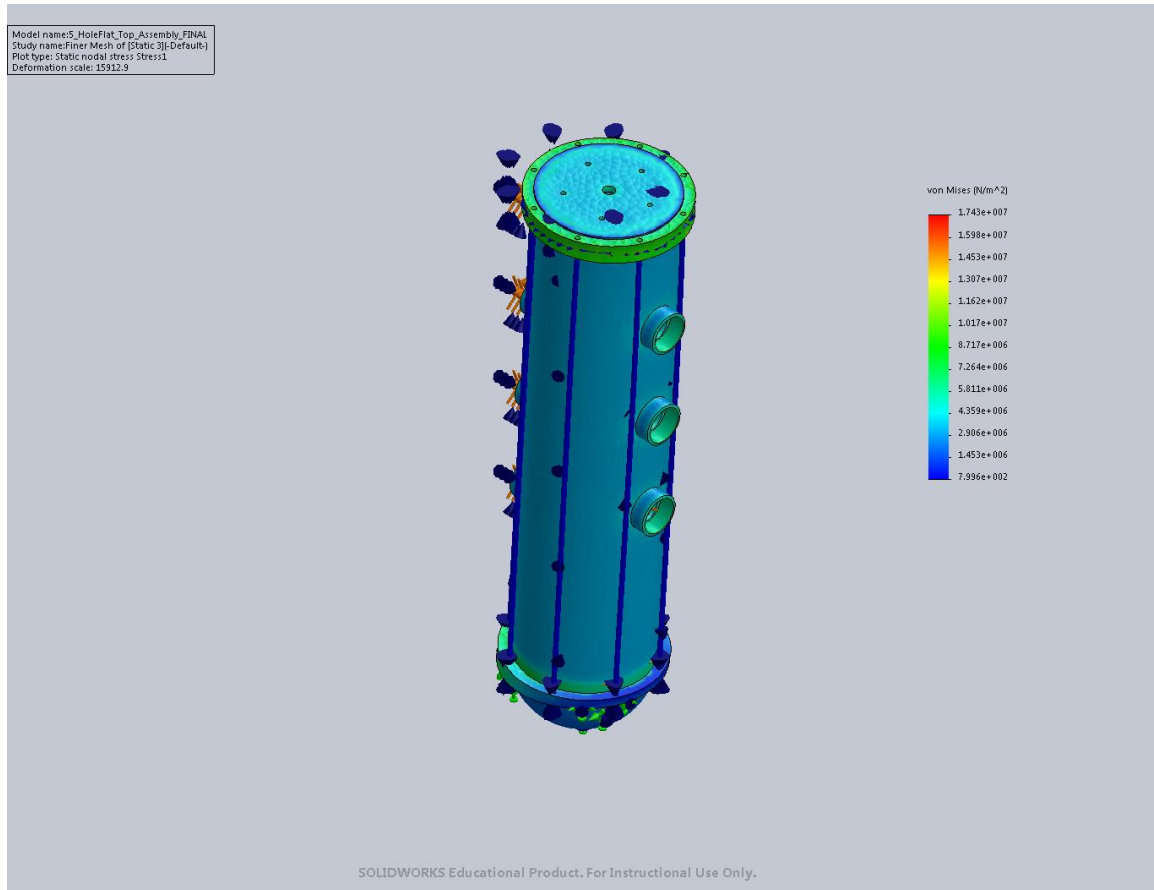


Figure 43: Final Design von Mises Stress Fine Mesh

Finer mesh setting tend to give more accurate results but also takes a longer time to simulation and use greater memory resources. Due to the fact that the study is divided into smaller pieces which therefore outcomes in more iterations and calculations to yield a final result. However, sometimes the finest settings are not required for the application.

For the simulation studies in Figures 44 to 46, the finest mesh setting was used. Figure 44 below shows the simulation for the Factor of Safety between 7.202 and 2.254×10^4 . It is also worth noting that there is a Factor of safety distribution at a minimum of 7.2.

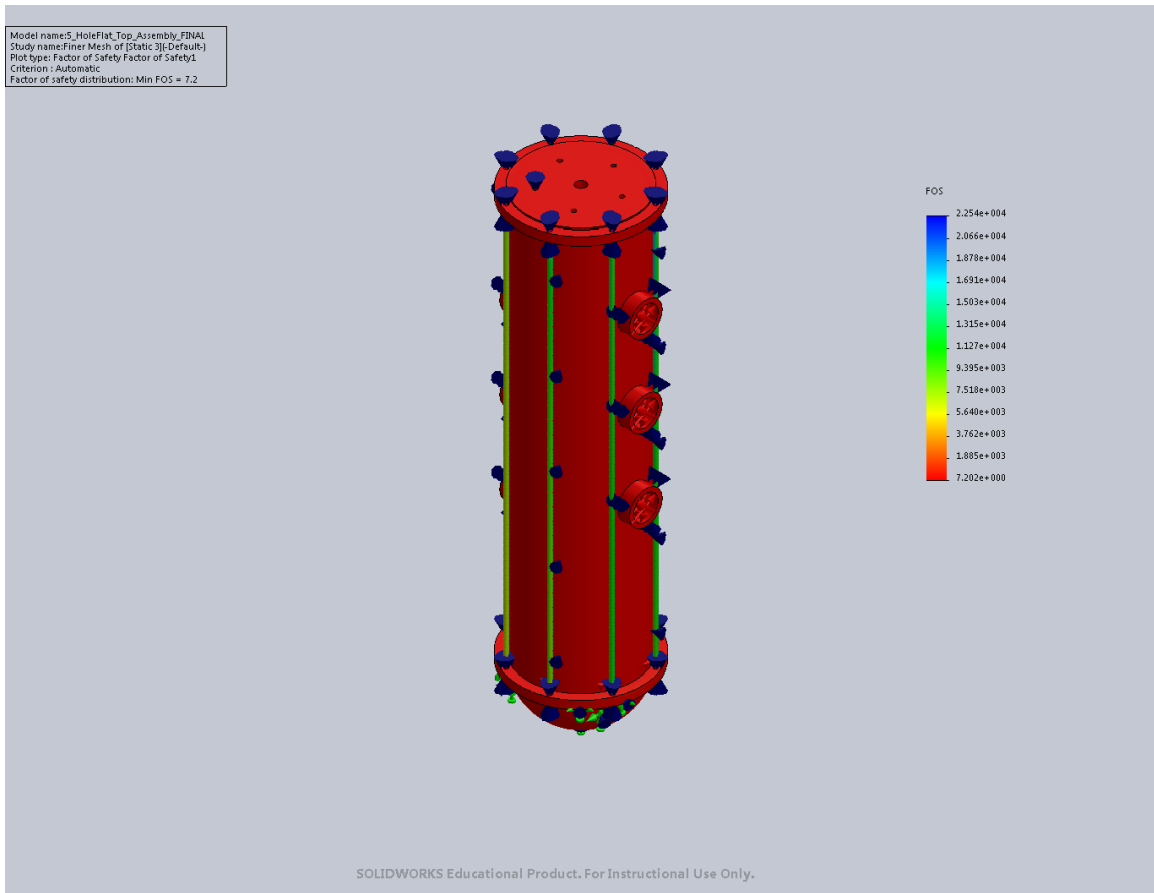


Figure 44: Factor of Safety Study for Final Design

Figure 45 shows a representation of the displacement which ranges between 1×10^{-30} to $4.553 \times 10^{-3} \text{ mm}$ and a deformation scale of 15912.9. Which is less than a millimeter of expansion during working pressure.

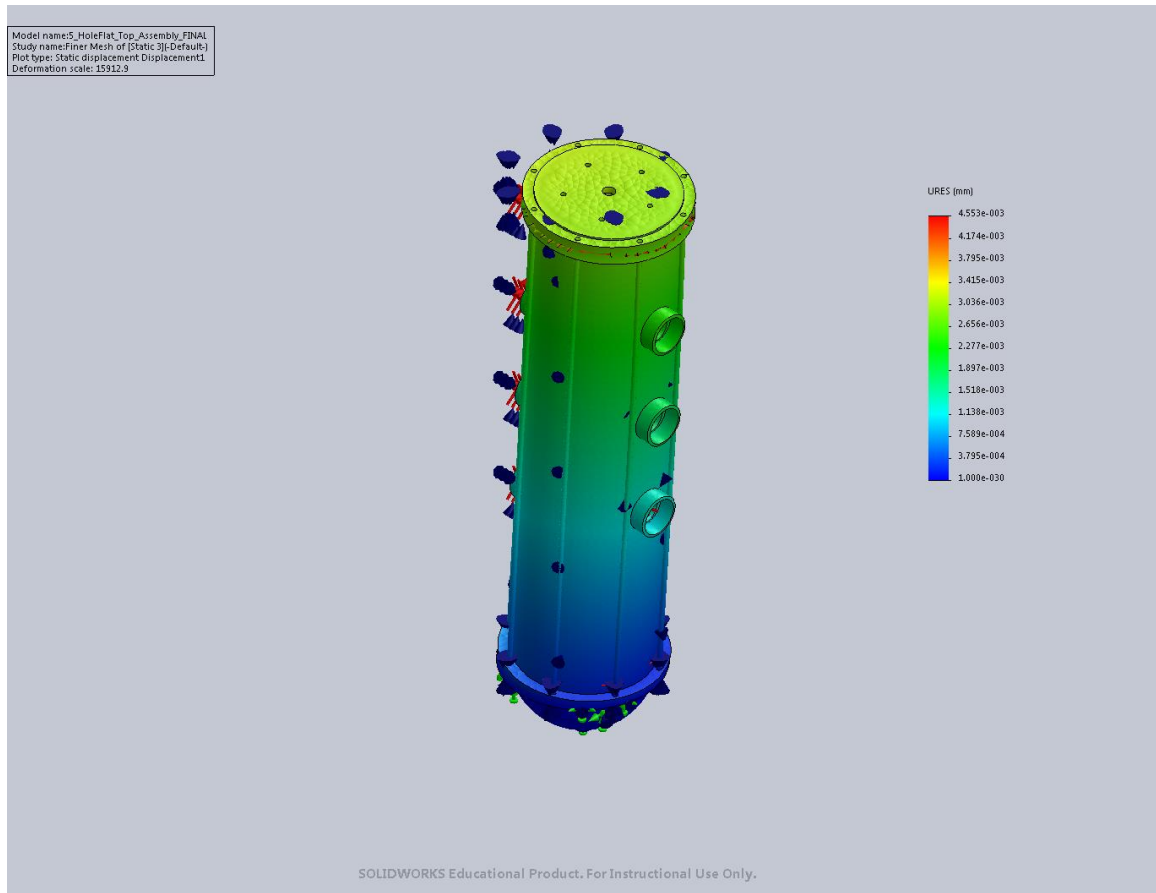


Figure 45: Displacement Study of Final Design

Figure 46 shows a representation of the Strain values which ranges between 3.278×10^{-8} to $7.639 \times 10^{-4} mm$ and on the same deformation scale of 15912.9 as both the von Mises and Displacement studies.

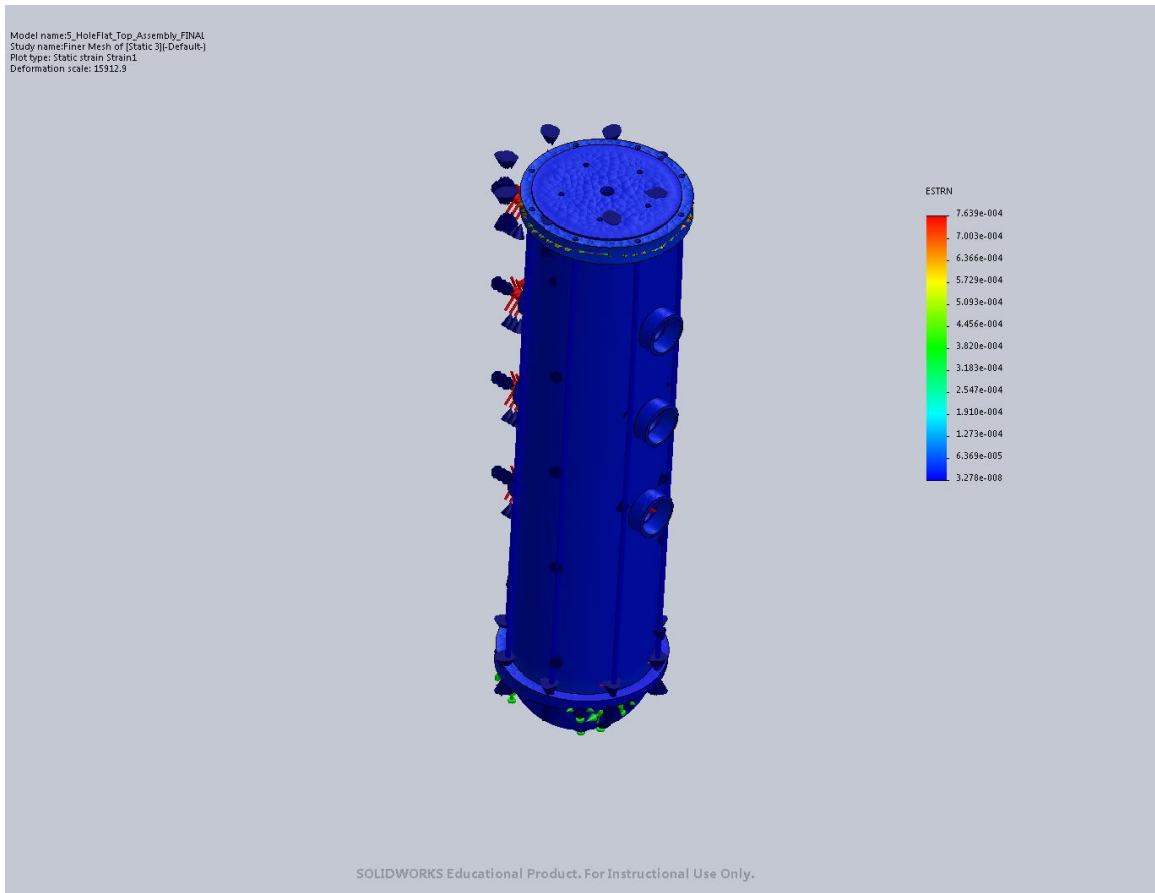


Figure 46: Strain study of Final Design

3.3 Fuel Injection System

The fuel delivery system consists of a fuel pump, a fuel injector, a pressure regulator, Teflon tubing and a fuel tank. The fuel pump is a high performance booster fuel pump capable of producing a maximum pressure of 125 psi. The pressure regulator is an AEM Electronics Billet Adjustable Fuel Pressure regulator which has a rated range of 20 to 150 psi. The Teflon tubing is a Tygon 2475 I.B. High-Purity Pressure Tubing in both the sizes of 1/2" inside diameter and 3/8" inside diameter. A previously used Diaphragm pump was incorporated as the fuel tank. Numerous hose fittings and adapters were combine to ensure the flow of 87-Octane. A full detailed list of the Bill of Material is displayed in Table 5 which is outlined in Appendix C.

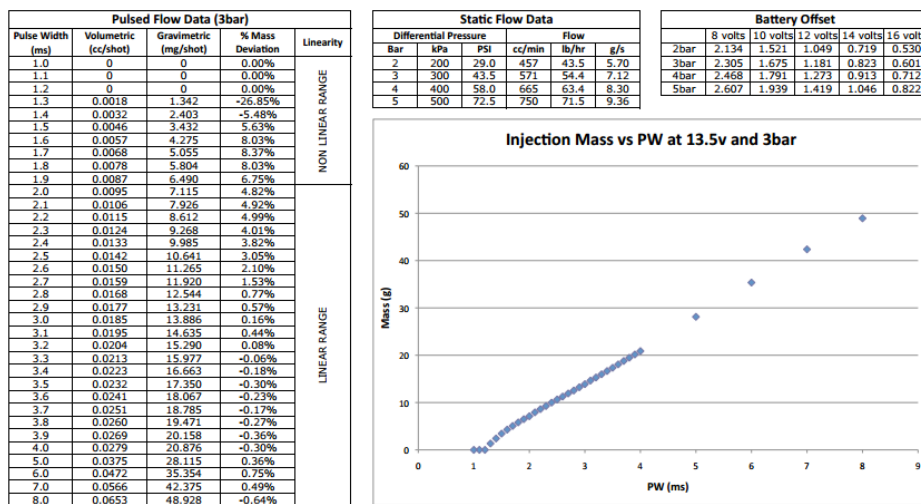
3.3.1 Fuel Injectors

The fuel injectors are a set of four Long 60mm EV14 manufactured by DeatschWerks. These fuel injectors are capable of supplying 550 cubic centimeters of fuel at 50 pounds. There are a 14mm fuel rail bore for the injectors and they are widely used in numerous universal applications and cost \$259.00. These fuel injections are also compatible with E85 and the data is shown in Figure 47.



Fuel Injector Characterization Summary

PN: 18u-XX-0050-X, 18u-XX-0550-X



NOTES
 All mass values (gravimetric) are calculated for pump gas using SG of 0.749
 Application specific calibration summaries are also available (visit website or inquire with tech support)
 Data on calibration summaries may vary slightly from data on this sheet due to in-car optimization

Figure 47: Fuel Injection Characterization Summary [32]

Figure 48 below shows the offset time in Milliseconds with (Pressure vs Voltage) for the battery offset.

Offset in Milliseconds (Pressure vs Voltage)

PSI > VOLTS v	43	58	70	80	90	100
8	2.27	2.47	2.58	2.67	2.81	2.90
9	1.94	2.11	2.23	2.31	2.43	2.52
10	1.64	1.79	1.91	1.99	2.10	2.18
11	1.38	1.51	1.63	1.71	1.81	1.89
12	1.15	1.27	1.39	1.46	1.55	1.63
13	0.96	1.07	1.19	1.26	1.34	1.41
14	0.80	0.91	1.02	1.09	1.17	1.23
15	0.68	0.79	0.89	1.95	1.03	1.09
16	0.59	0.71	0.80	0.86	0.93	0.99

Figure 48: Battery Offset in Milliseconds [32]

For more information about the dimensions of these injectors refer to Figure 78 in Appendix D.

3.3.2 SEL PLC

The SEL – 2411 in the Figure 49 below was used to control the fuel spray of the injector above. This Programmable Logic Controller (PLC) operates at a voltage of 250Vdc at 30 Amps. There is a continuous carry of 5Amps at 70°C and 4Amps at 85°C. The operating time for the coil energization to contact closure and register as a resistive load is typically less than or equal to 8ms [33].



Figure 49: Programmable Automation Controller SEL - 2411

The output 601 was used to engage the switch between the contact of 01 and 02. A three second delay was introduced when push button 3 is activated. The contacts for output 601 are then closed for 8 ms before reopening and shifting the LED for push button 3 to the on status. Finally, push button 4 is used to reset the LED for push button 3. This code is represented in graphical logic form from AcSELerator QuickSet in Figure 50 below.

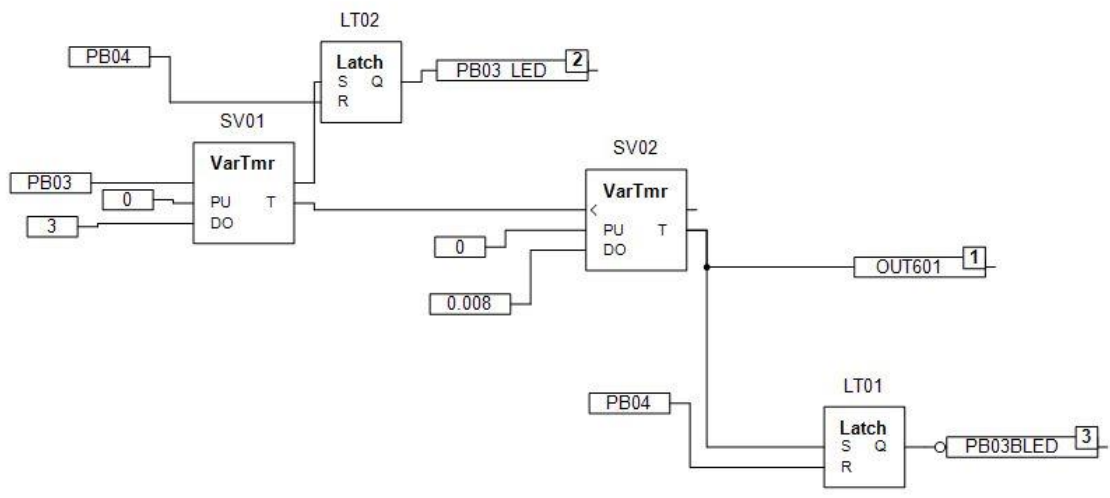


Figure 50: SEL PLC Code for activating the fuel injector

Based on the data above, the pickup time for this PLC was tested by conducting three tests and recording ten values each time. These results are shown in Table 1 below.

Table 1: SEL-2411 Pickup Time Results

Test 1 at 8 ms	Test 2 at 8 ms	Test 3 at 8 ms
11.0	11.2	11.2
11.2	11.2	11.2
11.2	11.2	11.2
11.2	11.2	11.2
11.2	11.0	11.2
11.2	11.2	11.2
11.4	11.0	11.2
11.2	11.0	11.2
11.2	11.2	11.2
11.2	11.2	11.2

These test were conducted with one minute intervals to ensure the contacts on the SEL-2411 did not increase in temperature due to the rapid opening and closing during a short time difference. The results conclude that the pickup time was constantly at a value of 11.2 with a maximum value of 11.4 and a minimum of 11.0.

3.4 Existing Pressure Vessel Assembled Test Setup

Correspondence was conducted with Mr. Cornell Constantinidis at Fabrication Associates, Inc. located in Charlotte, North Carolina in relation to the construction of a custom pressure [34]. Fabrication Associates, Inc. is a manufacturing company which specializes in machining and fabrication. After a few days of communications, a rough quote of \$4,600 was presented from Fabrication Associates, Inc. For further details on an itemization break down of all components included in the quote, refer to Figure 79 in Appendix E. Once University funds were secured by the engineering department, supplementary correspondence were conducted in order to achieve a mutually agreed upon custom pressure chamber design. For the specifications of the final certified pressure chamber, refer to the attached drawing in Figure 80 of Appendix F.

Subsequently to the arrival of the pressure chamber, steps were taken to ensure a secure and functional mounting of the roughly 130 lbs. pressure chamber. Due to the weight of the pressure chamber, a mobility option was to be employed in order to avoid the use of specialized apparatus or multiple people for adjustments. An 80/20 series of the aluminum bars were connected using T-slot fittings. The bolts for this assembly contain an Allen hex key for adjustments and were used to form a rectangular shaped cart. This setup allows for versatility with the addition of wheels and the ability to interchange existing configurations in moments. The 80/20 cart also provides high tensile strength which was required for mounting a pressure chamber of the specified weight. However, in order to not damage the surface of the aluminum with scrapes and gouges, two pieces of plywood each $\frac{3}{4}$ " in thickness were mounted between the pressure chamber

and the 80/20 cart. Figure 51 below shows the complete current test setup with all of the used components.



Figure 51: Existing Equipment and Test Setup

CHAPTER 4: RESULTS

4.1 Experimental Results

Experimental results include the accumulation mass as well as the electrical charge density for each of the 20 injector at the pressures of 40, 50 and 60 psi. Additionally, statistical analysis was conducted for further evaluation of the recorded information.

4.1.1 Dielectric Fluid Mass Evaluation

In order to determine the amount of liquid produced by the injector for each activation, experiments were investigated to measure the mass of the fluid. Once the fuel pump pressurized the fuel system to the desired pressure, the SEL 2411 was used to rapidly trigger the opening and closing of the fuel injector. The 87 octane gasoline was then ejected into a glass beaker which was on the top of a zeroed mass scale and the mass was recorded. This process was conducted 20 times for the pressures of 40, 50 and 60 psi. The fuel in the beaker was allowed to accumulate after each shot. The average mass for each shot spray was calculated and the results are shown in Table 2 below.

Table 2: Average Mass per injector shot for 40, 50 and 60 psi

Gage Pressure at Regulator (psi)	Average Mass per Spray (grams)
40	0.034
50	0.035
60	0.038

The average masses per spray for the experiments were 0.034, 0.035 and 0.038 grams which coincide with 40, 50 and 60 psi respectively. Figure 52 demonstrates a graphical plot of all of the values obtained during this experiment.

CUMULATIVE MASS FOR EACH SPRAY

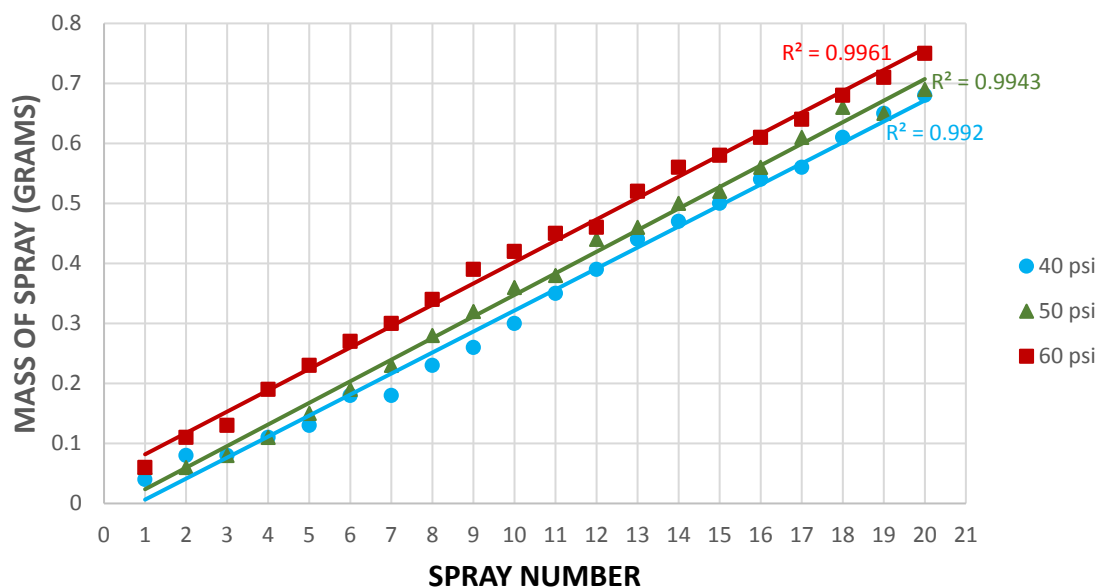


Figure 52: Graph of Cumulative Mass as a function of each Spray

It is worth noting that mass of the fuel discharged did not experience a continuous increase at each spray interval. In some cases, the mass value remained the same or encountered an exceptionally insignificant amplification of the previous assessment. Even in one condition during the examination at 50 psi, the mass value generated a loss in mass. For additional description on every data point which was documented, refer to Appendix G and Table 6.

Based on the values obtained for the mass during the experiments conducted at 40, 50 and 60 psi, an average volume per spray was computed and displayed in Table 3. The value used in the calculations for density was 719.7 kg/m^3 which is present in Fuels and Fuel-Additives Journal Article [2]. For details on the value of each individual point calculated, refer to Appendix H and Table 7.

Table 3: Calculated Average Volume per injector shot for 40, 50 and 60 psi

Gage Pressure at Regulator (psi)	Average Volume per Spray (kg/m ³)
40	4.724×10^{-8}
50	4.794×10^{-8}
60	5.211×10^{-8}

4.1.2 Dielectric Fluid Charge Spray Analysis

To determine the effect of tribocharging of a dielectric fluid and any charge differences produced by a typical fuel injector, electrical charge values were measured and documented. An exceedingly comparable technique was undertaken to emit electrical charge numerical evaluations. Again, with the fuel system pressurized to the preferred pressure, the 87 octane gasoline was released from the fuel injector, but instead of a beaker the fuel travelled into a faraday cup. This faraday cup was connected to an electrometer which exhibits a digital output of the difference in charge. Once more, 20 data points were collected and the mean as well as the standard deviation was computed for each of the three injection pressure intermissions which are represented in Table 4.

Table 4: Average Net Charge Density values per injector for 40, 50 and 60 psi

Gage Pressure at Regulator (psi)	Average Net Charge Density per spray (nC/g)	Standard Deviation
40	1.265	0.019
50	1.286	0.004
60	1.368	0.004

The mean net charge density per spray for the experiments were 1.265, 1.286 and 1.368 Coulombs per grams while the standard deviations were 0.019, 0.004 and 0.004 which both corresponds to 40, 50 and 60 psi respectively. Figure 53 reveals a graphical plot of all of the values ascertained throughout this experiment.

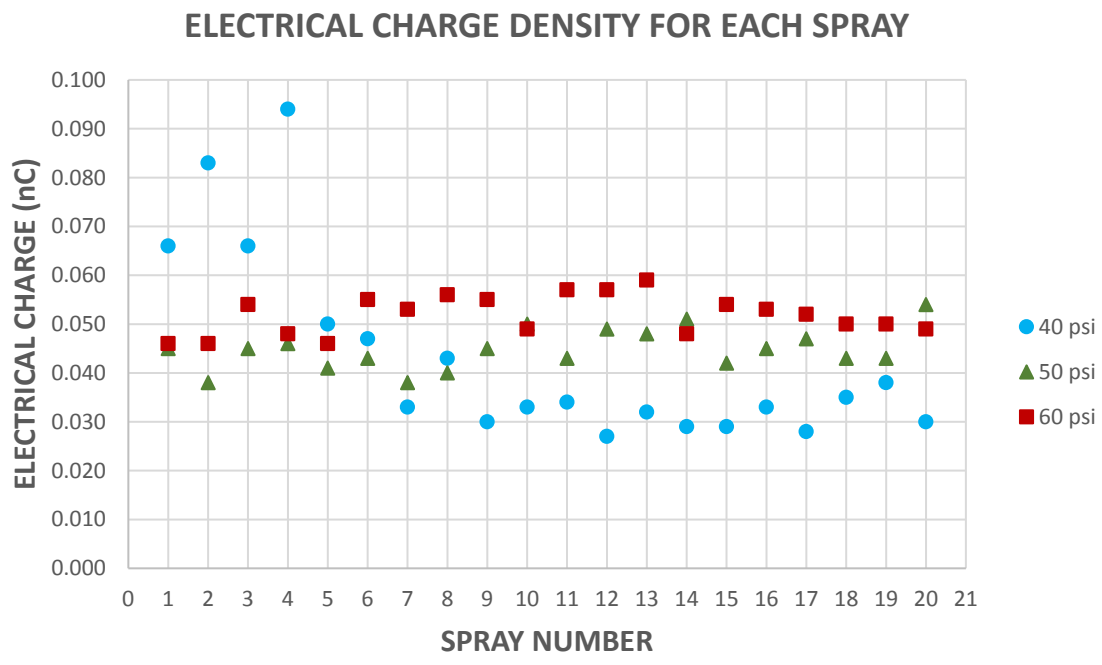


Figure 53: Graph of Electrical Charge for each Spray

The above figure indicates fairly large electrical values during the beginning of the data gathering process and seems to not adhere to the trend which is experienced during the remainder of the experiments at 40 psi or even at 50 and 60 psi. A Boxplot of the electrical charge data was constructed in Minitab and appears below in Figure 54.

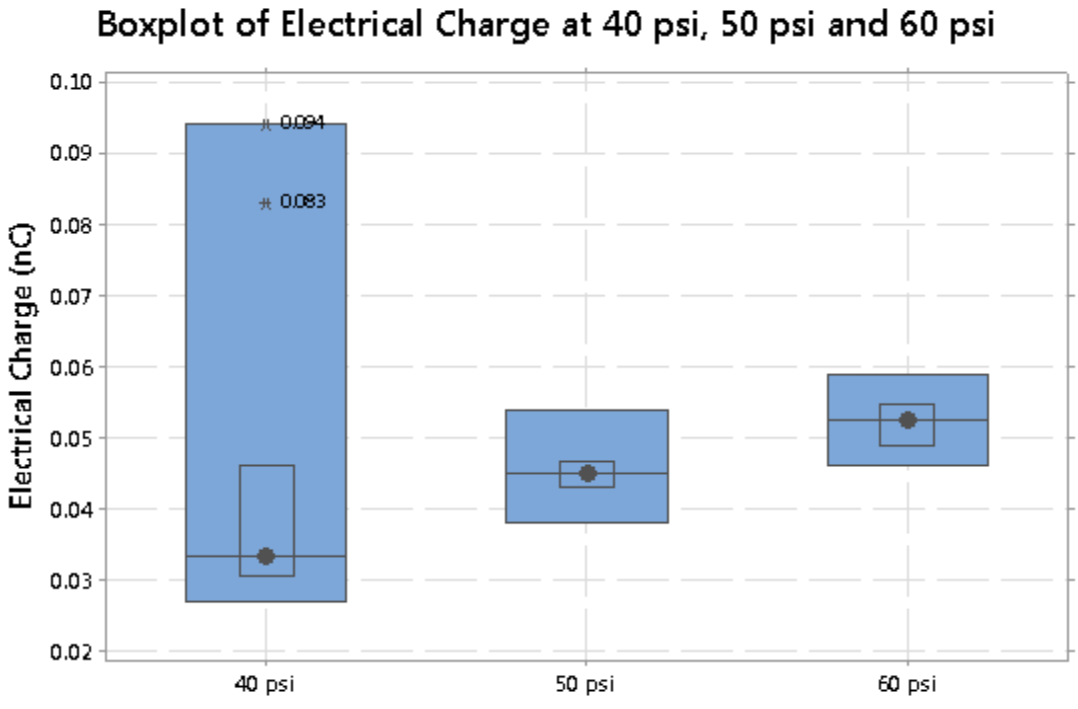


Figure 54: Boxplot graph of Electric Charge data distribution

As to be expected, the large charge values experienced during fuel injection at 40 psi were confirmed to be outliers when compare to the rest of the values at the same injection pressure. This may be because the system was not at equilibrium or a steady state due to the fact that these values were the first to be recorded for the day. It is also significant to mention that for both values for the average mass and mean net electric density charge an enhancement was underwent as the fuel injection pressure intensified. For further analysis of the data which produced this phenomenal, refer to Table 8 in Appendix I.

4.2 Simulation Results

Simulation results were evaluated with no electric field applied, with an electric field of 10kV and with an electric field of 20kV after a geometry model was imported in to COMSOL Multiphysics. The simulation calculations were contrasted and preliminary findings were interpreted.

4.2.1 COMSOL Multiphysics Simulations at 10kV

COMSOL Multiphysics is a simulation software which uses Finite Element Analysis (FEA) to solve complex mathematical and physics algorithms. The software allows for the construction or importation of 3-D models for analysis and simulations. In order to achieve the simulations and resulting data, two additional COMSOL products were employed which were the CAD Import Module and the Particle Tracing Module. Parameters for the investigation simulations were outlined for the test model geometry as well as the surrounding assessed conditions. The simulation model geometry was 10 cm in diameter while the height was 20 cm and separated at the center. The top of the model was exposed to +10 kV while the bottom section experienced a potential difference of -10kV as represented by Figure 55 below. In order for the simulation to begin, the test model was first meshed with an average element quality of 0.7132 while using both tetrahedral elements and triangular elements with values of 3177 and 584 respectively. The mesh size yielded a curvature factor of 0.6 and a resolution of narrow regions resulting in 0.5 at a maximum element growth rate of 1.5. The meshing indicated a corresponding maximum of 0.02 and a minimum of 0.0036 for the element size. An illustration of the meshed model is shown in Figure 56. Subsequently, the edge and

vertex elements were 88 and 12 respectively. For all of the defining parameters used in the initial definition of the model, refer to Table 9 which is a part of Appendix J.

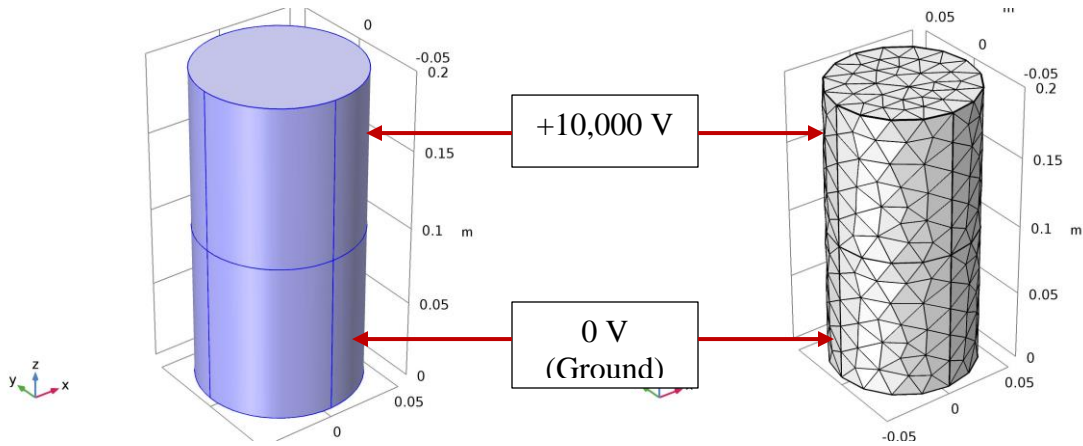


Figure 55: Defined cylindrical geometry with global and model parameters

Figure 56: Mesh representation of defined parameters for simulations

Simulations were conducted in order to replicate the release of 20 fuel droplets from an injector or nozzle every 0.8 ms. The result means 100 fuel droplets were released (0 to 8 ms) which resulted in a total of 2000 fuel droplets. This was done to determine a non-uniform distribution for both the particle diameters as well as the charge on a droplet. There was a 95% confidence interval implemented for the statistical analysis. Histograms from COMSOL were created for both the particle diameters which were measured in micrometers and the charge on a droplet in coulombs. Both histograms are displayed below in Figure 57 and 58 respectively. However, it is worth noting the Rayleigh limit was applied to the distribution for the charge on a droplet. A large number of values were observed to be between 9.5 and 11 μm for the particle diameters and for the charge on a droplet, a considerable amount of data points were between 1.2 and 1.6×10^{-13} C.

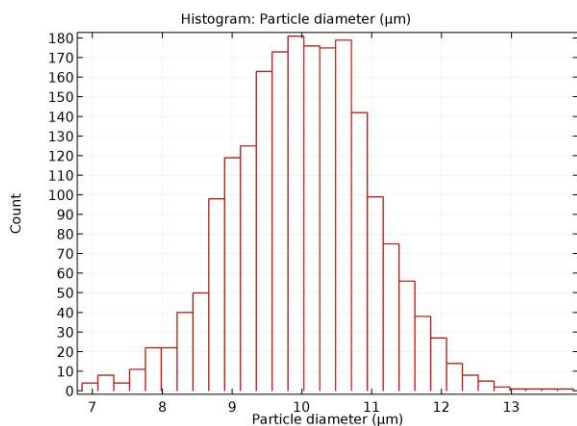


Figure 57: Distribution of particle diameters

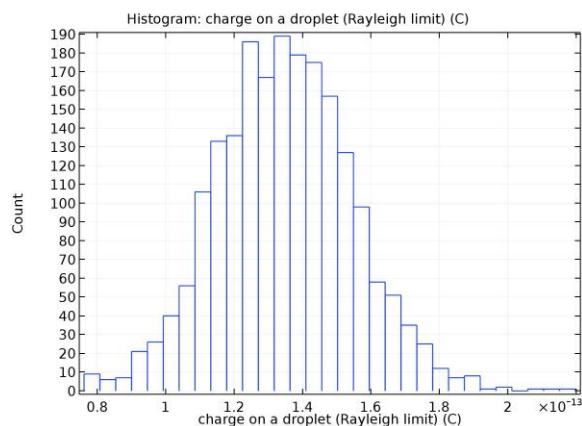


Figure 58: Rayleigh limit distribution of charge

Experimental simulations were conducted for the pressures inside the modeled cylinder of 40, 50 and 60 psi. The initial droplet velocity after dispersion for the nozzle was set to 200 m/s with the duration of the injection occurring for 50 ms. Different replications were also directed with and without the application of a 10kV electric field. Figures 59 and 60 below demonstrates the comparison of the computer-generated fuel droplets without an applied electric field and when a 10kV electric field is applied. Figure 59 shows the continual widening of the dispersed fuel towards the modeled walls of the cylinder. Whereas, Figure 60 expresses a conversion of the fuel droplets before continuing to expand after the center feature of the cylinder when the effects of the electric field is not present.

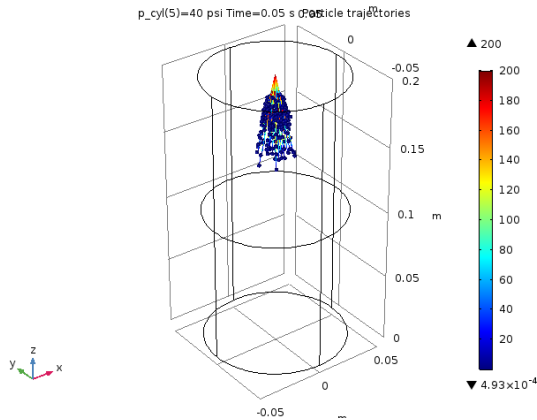


Figure 59: Particle Trajectories at 40 psi with no electric field applied

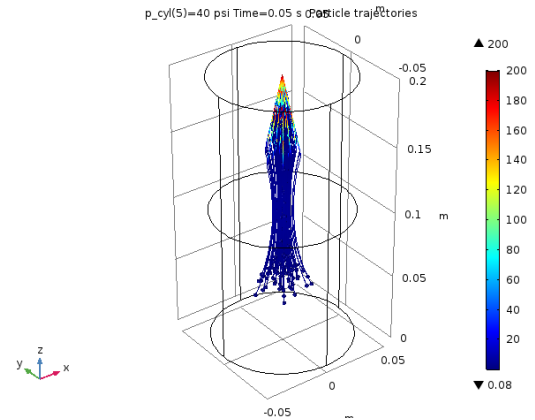


Figure 60: Particle Trajectories at 40 psi with an electric field of 10kV applied

The internal pressure of the cylinder was increased from 40 to 50 psi and further recreation evaluation was performed for both scenarios with and without an applied electric field with all other parameters remaining identical. The particle trajectories with no electric field applied is displayed in Figure 61 while the particle trajectories with an electric field of 10kV applied is represented in Figure 62. Even with the increase in pressure, the comparison for the relationship between both the non-electric and electric field was constant. However, an increase on the minimum value for the applied electric field of 40 and 50 psi was observed from 0.08 to 0.11.

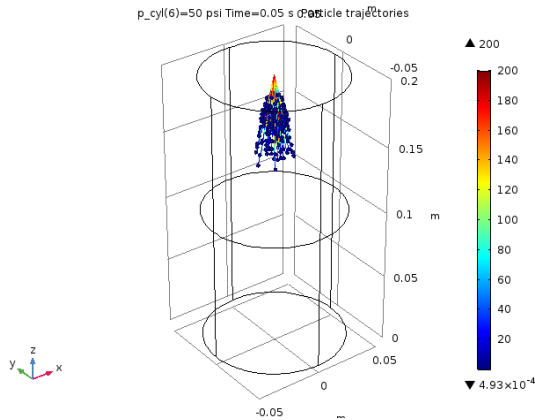


Figure 61: Particle Trajectories at 50 psi with no electric field applied

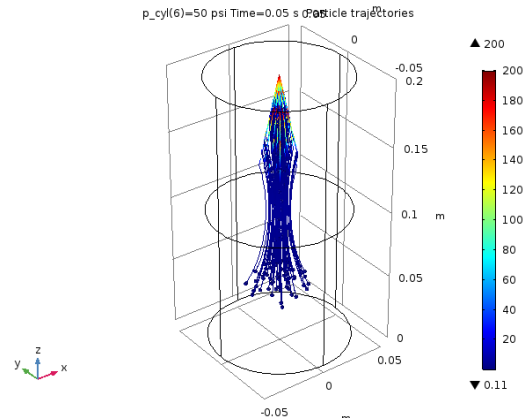


Figure 62: Particle Trajectories at 50 psi with an electric field of 10kV applied

The next evaluation entailed pressurizing the cylindrical simulation model to 60 psi. As with the previous simulations at 40 and 50 psi, the results indicate a similar phenomenon for both the electric and non-electric field assessments. Figure 63 below and on the left shows the particle trajectories with no electric field at 60 psi while Figure 64 shows the particle trajectories for the droplets exposed to the 10kV electric field. There was a very small value change on the scale for the non-electric field calculations at 40 and 50 psi which was 4.93×10^{-4} to a 4.94×10^{-4} for the experiment operated at 60 psi.

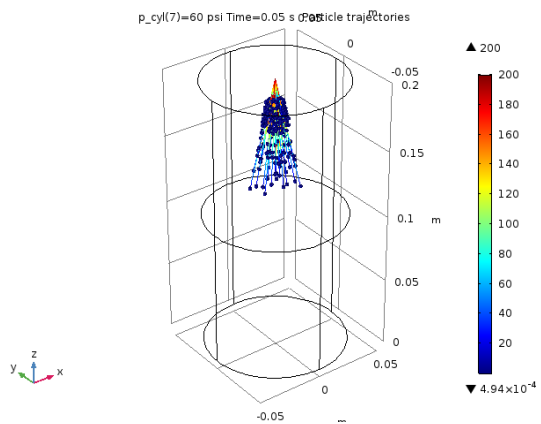


Figure 63: Particle Trajectories at 60 psi with no electric field applied

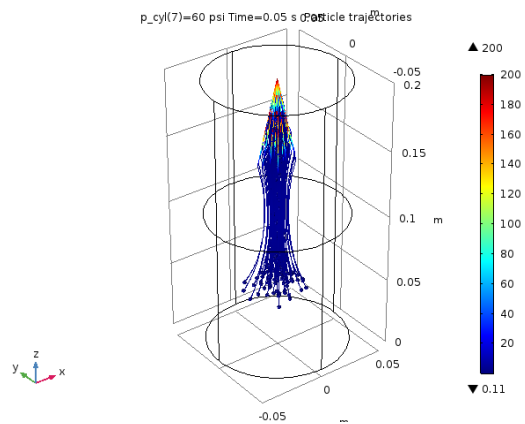


Figure 64: Particle Trajectories at 60 psi with an electric field of 10kV applied

4.2.2 COMSOL Multiphysics Simulations at 20kV

Based on the results achieved from the experimentations without the presents of an electric field and with an applied electric field of 10kV, subsequent evaluations were conducted with an electric field which was produced at a potential difference of 20kV. This was done because the preliminary data achieved while operating at an applied electrical field of 10kV did not reveal much deviation between the internal model cylindrical geometry at the pressures of 40, 50 and 60 psi. Figure 65 below demonstrates a multislice of the electric potential difference at 20kV for a time of 0.0195 seconds. All other defined parameters remained the same to determine the effect of increasing the force of the applied electric field.

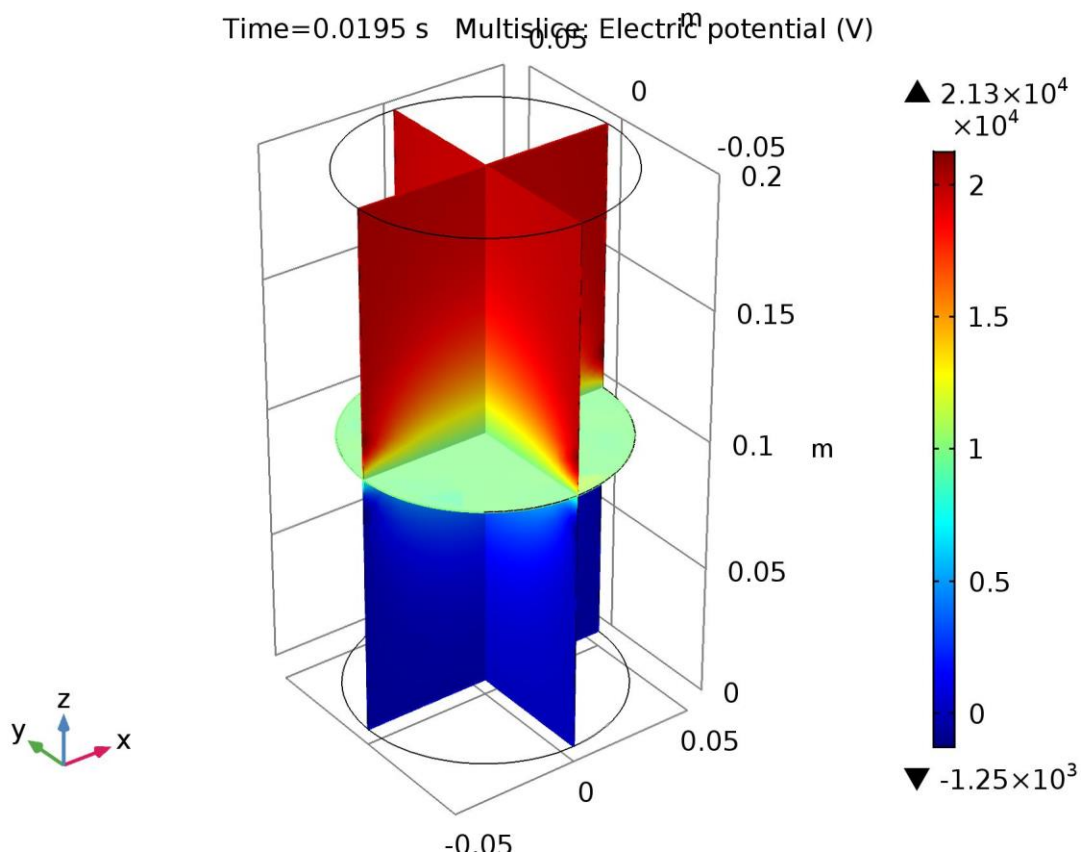


Figure 65: Electric potential for 20kV when time = 0.0195

As with the experiments conducted at an applied electric field on 10kV the first evaluation consideration occurred at 40 psi. Figure 66 below shows the particle trajectories while the fuel droplets were subjected to 20kV of applied electric field. The result from this evaluation indicates a more visible constriction for a longer duration when compared to the 40 psi investigation conducted under a potential difference of 10kV. Figure 67 indicates the deflection as a function of time when the Z-axis is used for symmetry. From this graph at a time of 0.04 seconds with a deflection of roughly 0.0225 meters can be observed.

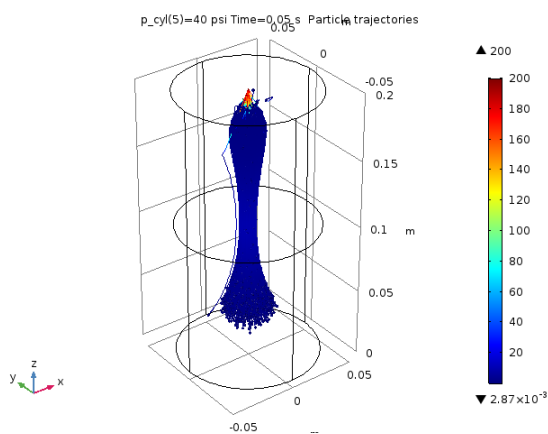


Figure 66: Particle Trajectories at 40 psi with an electric field of 20kV applied

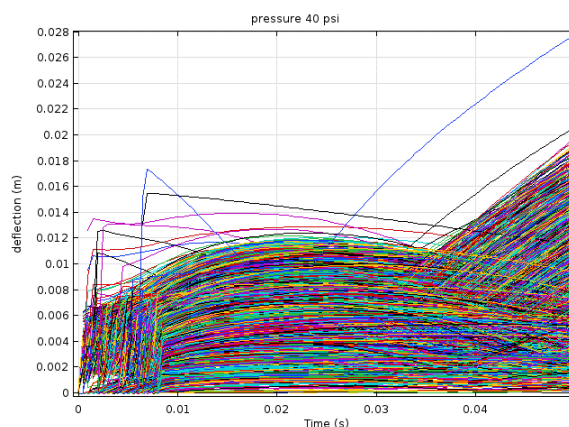


Figure 67: Z-axis of symmetry for deflection of droplets with an electric field of 20kV applied at 40 psi

The next particle trajectories display is shown in Figure 68 at the intermediary point of 50 psi with an electric field of 20 kV applied. The results exhibit similarity to the prior test conducted at 40 psi and also the same distinction description when compared to the experiment conducted at the same pressure with the presence of a 10kV applied electric field. Figure 69 shows the evaluation of the deflection with respect to time as it relates to the Z-axis of symmetry. A deflection of about 0.0305 meters was detected at a

time of 0.01 seconds. Larger overall displacements were observed when it compared to the results achieved at 40 psi. It was likewise viewed there was a change from 2.87×10^{-3} to 3.16×10^{-3} between the pressures of 40 and 50 psi respectively.

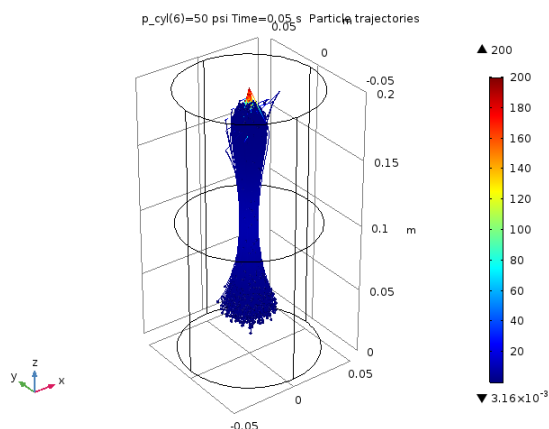


Figure 68: Particle Trajectories at 50 psi with an electric field of 20kV applied

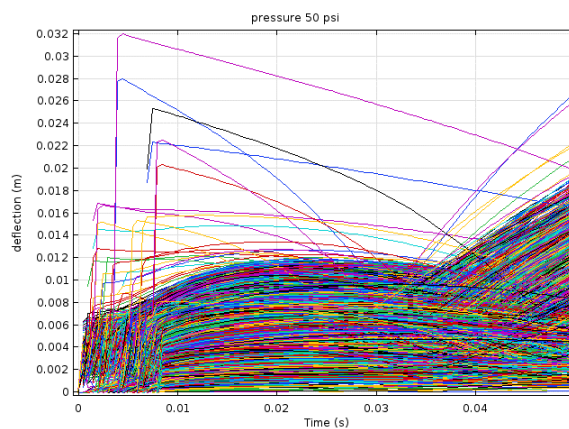


Figure 69: Z-axis of symmetry for deflection of droplets with an electric field of 20kV applied at 50 psi

A final investigation was done at the last cylindrical model pressure of 60 psi. As with the previous results at 40 and 50 psi, an identical phenomenon was illustrated where all three pressures exhibited a parallel pictorial interpretation of a restriction when compared to the results ascertained at 10kV. The minimum on the scale for the particle trajectories once again was altered slightly from 3.16×10^{-3} for 50 psi to 5.98×10^{-3} for the 60 psi experiment which is represented in Figure 70. There was a deflection of approximately 0.025 meter and a time of 0.01 seconds for the Z-axis of symmetry for the deflection of droplets with an electric field of 20kV applied at 60 psi which is in Figure 71.

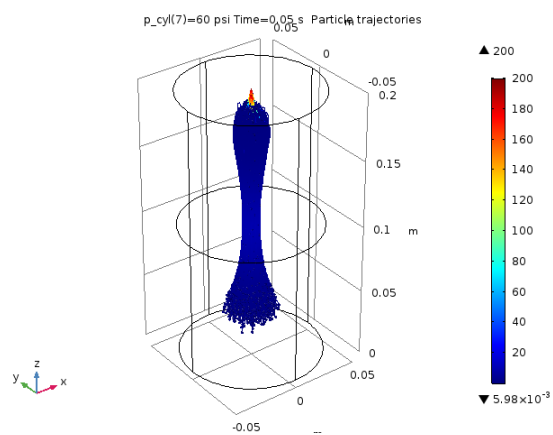


Figure 70: Particle Trajectories at 60 psi with an electric field of 20kV applied

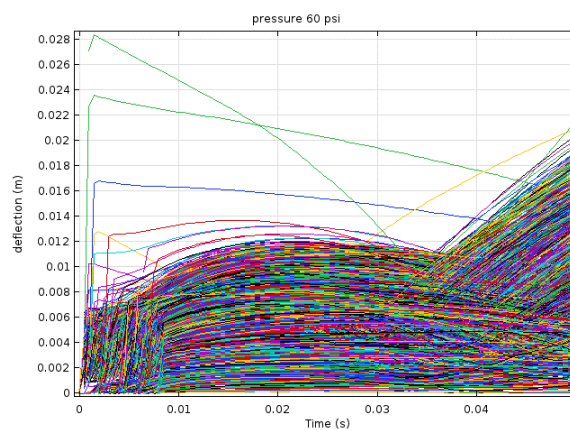


Figure 71: Z-axis of symmetry for deflection of droplets with an electric field of 20kV applied at 60 psi

CHAPTER 5: CONCLUSIONS

5.1 Discussion

The experimental results for the dielectric fluid mass evaluation indicated a linear relationship at the pressures of 40, 50 and 60 psi. The average mass per spray was calculated for all three pressures and as anticipated, the experiment established at 60 psi was the largest resulting value of 0.038 grams. On the other hand, the values for 40 and 50 psi which are 0.034 and 0.035 grams respectively were significantly close and were nevertheless still in close proximity to the calculated value achieved for 60 psi investigation. After evaluating the cumulative mass for each spray at each of the three pressures, it was determined the pressure was directly proportional to the R-squared value which is the measurement of the regression line fit to the related data points. The R-squared values were 0.992, 0.9943 and 0.9961 for the corresponding pressures of 40, 50 and 60 psi. All of these experimental R-squared values are exceedingly close to the ideal R-squared value of 1 or 100%.

As a part of the experimental results, the average electrical charge density values and standard deviations for each spray were additionally computed for the unchanged three pressures of 40, 50 and 60 psi. The values for the average net charge densities were 1.265, 1.286 and 1.368 while the standard deviations were 0.019, 0.004 and 0.004 for the corresponding respective pressures. Once again, it was predictable due to the higher pressure at 60 psi a higher electrical net charge density would be present. Further statistical analysis was executed and it was verified that two of the values obtained during the experiment conducted at 40 psi were outliers.

Simulation and analysis were done in COMSOL Multiphysics using FEA for experiments conducted at 40, 50 and 60 psi inside the cylindrical model chamber. Test parameters were defined and simulations were meshed as well as executed. A total of 2000 fuel droplets were simulated to be release into the cylindrical geometry model. A statistical distribution was developed in the form of histograms with a 95% confidence interval for both the fuel particle diameters and the electrical charge of the droplets. A sizable quantity of the fuel particle diameters were amongst 9.5 and 11 μ m while a substantial segment of the charge on a droplet was between 1.2 and 1.6 $\times 10^{-13}$ C.

Initial tests were conducted to simulate injecting fuel in the model geometry at the specified pressures of 40, 50 and 60 psi. Consecutively, identical assessments were performed with the introduction of a 10kV applied electric field for comparison to determine the effects. The results indicated the existence of the applied 10kV electric field condensed and narrowed the fuel particle trajectories when compared to the control experiment of no electric field at each of the three pressures. However, preliminary outcomes appear to designate no distinctive alterations between atmospheric pressure and elevating the internal pressure of the cylindrical geometry to 40, 50 and 60 psi. On the other hand, supplementary examinations were accompanied with the same parameters except for the elevation of the potential difference from 10kV to 20kV for the applied electric field. These preliminary results similarly reveal further compression and contraction of the particle trajectories when compared to the experiments at 10kV for the three equivalent pressures.

5.2 Potential Future Work

Further research can be conducted in a wide range of areas as it relates to the controlling and manipulation of dielectric fluids using electric fields. With the prior research along with this research, it appears electric fields can be used to control the particle trajectories of dielectric fluids. Nonetheless, some of the preliminary discoveries were not as anticipated. For example, the particle trajectories did not demonstrate any variations when there was an escalation in pressure inside the cylindrical model. Below is a list of potential research development which can be considered for future work:

- Continue the assembly of the pressure vessel system in order to interface with the existing fuel injection system. This will entail the procurement of additional equipment. For a complete list of the remaining bill of materials, refer to Table 10 in Appendix K.
- Conduct mass accumulation and electric charge testing with higher Octane Number rated fuels and different fuels with different properties such as diesel, ethanol and methanol.
- Conduct experimental evaluations at 40, 50 and 60 psi without the application of an electric field and with an applied electric field of 10kV. Verify the preliminary COMSOL model and determine whether the increase in pressure has an effect on the particle trajectories of the fuel droplets.
- Confirm experimentally the effects of increasing the electric field from 10kV to 20kV on the particle trajectories of the fuel droplets.
- Conduct investigations simulation and experimentally at higher fuel injection pressures.

- Investigate the effects of electric fields during the process of combustion.
Conduct experimental combustion testing inside existing pressure chamber.
- Investigate the effects of fuel distribution and mixing during electro spraying for droplet consistency
- Compare the effects of electro sprayed fuel dispersion and turbulent air flow fuel dispersion
- Investigate the uniformity and dispersion of fuel concentration as it relates to the applied charge
- Determine whether fuel droplets with an increase in electrical charge is beneficial for the combustion process
- Optimize the electrical droplet charge for maximum efficiency over different ranges during distinctive scenarios of the ICE process
- Investigate the potential different locations for the application of the electric fields such as electrifying the injector nozzle instead of the cylindrical walls

BIBLIOGRAPHY

- [1] G. Fiengo, "Common rail system for GDI engines : modelling, identification, and control," 2013.
- [2] J. Hancsók and S. P. Srivastava, "Fuels and fuel-additives," 2013.
- [3] A. K. Agarwal, D. K. Srivastava, A. Dhar, R. K. Maurya, P. C. Shukla, and A. P. Singh, "Effect of fuel injection timing and pressure on combustion, emissions and performance characteristics of a single cylinder diesel engine," *JFUE Fuel*, vol. 111, pp. 374-383, 2013.
- [4] H. P. Wang, D. Zheng, and Y. Tian, "High pressure common rail injection system modeling and control," *ISA Transactions*, vol. 63, pp. 265-273, 7// 2016.
- [5] C. Yao, P. Geng, Z. Yin, J. Hu, D. Chen, and Y. Ju, "Impacts of nozzle geometry on spray combustion of high pressure common rail injectors in a constant volume combustion chamber," *Fuel*, vol. 179, pp. 235-245, 9/1/ 2016.
- [6] P. Dong, T. Inaba, K. Nishida, and D. Shimo, "Characteristics of the internal flow and the near-field spray of a single-hole injector and a multi-hole injector for diesel engines," *Proc. Inst. Mech. Eng. Part D J. Automob. Eng. Proceedings of the Institution of Mechanical Engineers, Part D: Journal of Automobile Engineering*, vol. 230, pp. 632-649, 2016.
- [7] F. A. International Colloquium in Textile Engineering, Design, M. R. Ahmad, and M. F. Yahya, "Proceedings of the International Colloquium in Textile Engineering, Fashion, Apparel and Design 2014 (ICTEFAD 2014)," 2014.
- [8] A. Gomez and K. Tang, "Charge and fission of droplets in electrostatic sprays," *Physics of Fluids*, vol. 6, 1994.
- [9] J. Shrimpton, *Charge injection systems : physical principles, experimental and theoretical work*. Berlin: Springer Verlag, 2009.
- [10] J. M. López-Herrera, A. Barrero, A. Boucard, I. G. Loscertales, and M. Márquez, "An experimental study of the electrospraying of water in air at atmospheric pressure," *Journal of the American Society for Mass Spectrometry*, vol. 15, pp. 253-259, 2// 2004.
- [11] H. M. A. Elghazaly and G. S. P. Castle, "Experimental study on the breakup of charged liquid droplets," *IEEE Trans. on Ind. Applicat. IEEE Transactions on Industry Applications*, vol. 25, pp. 48-53, 1989.
- [12] H. Baharvand and N. Aghdami, "Stem cell nanoengineering," 2014.
- [13] T. Paillat, E. Moreau, and G. Touchard, "Space charge density at the wall in the case of heptane flowing through an insulating pipe," *Journal of Electrostatics*, vol. 53, pp. 171-182, 8// 2001.
- [14] E. Németh, V. Albrecht, G. Schubert, and F. Simon, "Polymer tribo-electric charging: dependence on thermodynamic surface properties and relative humidity," *Journal of Electrostatics*, vol. 58, pp. 3-16, 5// 2003.
- [15] A. G. Bailey, "The science and technology of electrostatic powder spraying, transport and coating1," *Journal of Electrostatics*, vol. 45, pp. 85-120, 12/10/ 1998.

- [16] M. B. Mayr and S. A. Barringer, "Corona Compared with Triboelectric Charging for Electrostatic Powder Coating," *JFDS Journal of Food Science*, vol. 71, pp. E171-E177, 2006.
- [17] L. Goldsworthy, N. Ashraf, and P. A. Brandner, "Development of a high pressure chamber for research into diesel spray dynamics," *Australian Journal of Mechanical Engineering*, vol. 7, pp. 137-156, 2009/01/01 2009.
- [18] K. B. Doyle and M. A. Kahan, "Design strength of optical glass [5176-03]," *PROCEEDINGS- SPIE THE INTERNATIONAL SOCIETY FOR OPTICAL ENGINEERING*, pp. 14-25, 2003.
- [19] B. Cai, Y. Liu, Z. Liu, X. Tian, C. Ren, and A. Abulimiti, "Exploratory study on load and resistance factor design of pressure vessel for subsea blowout preventers," *Engineering Failure Analysis*, vol. 27, pp. 119-129, 1// 2013.
- [20] C. Kuo, "Load and Resistance Factor Design LRFD for Deep Foundations," 2004.
- [21] D.-S. Son, J.-H. Hong, and S.-H. Chang, "Determination of the autofrettage pressure and estimation of material failures of a Type III hydrogen pressure vessel by using finite element analysis," *International Journal of Hydrogen Energy*, vol. 37, pp. 12771-12781, 9// 2012.
- [22] P. Xu, J. Y. Zheng, and P. F. Liu, "Finite element analysis of burst pressure of composite hydrogen storage vessels," *Materials & Design*, vol. 30, pp. 2295-2301, 8// 2009.
- [23] A. M. P. De Jesus, A. S. Ribeiro, and A. A. Fernandes, "Validation of procedures for fatigue life assessment of a steel pressure vessel," *Fatigue & Fracture of Engineering Materials & Structures*, vol. 27, pp. 799-810, 2004.
- [24] N. Soga, D. Holcomb, and H. Spetzler, "Determination of strains in optical windows of a highpressure chamber by holographic interferometry and finite element analysis," *Review of Scientific Instruments Review of Scientific Instruments*, vol. 47, pp. 1453-1456, 1976.
- [25] J. E. Field and W. F. Kirkwood, "Stress concentrations around multiple windows in a high-pressure vessel," *Experimental Mechanics*, vol. 17, pp. 223-227, 1977// 1977.
- [26] B. Ihracska, R. J. Crookes, D. Montalvão, M. R. Herfatmanesh, Z. Peng, S. Imran, *et al.*, "Opto-mechanical design for sight windows under high loads," *Materials & Design*, vol. 117, pp. 430-444, 3/5/ 2017.
- [27] Z. Chen, "Nonlinear stress analysis and design optimization of ultra-high pressure composite vessels," MQ92465 M.A.Sc., University of Windsor (Canada), Ann Arbor, 2004.
- [28] M. A. Guerrero, C. Betegón, and J. Belzunce, "Fracture analysis of a pressure vessel made of high strength steel (HSS)," *Engineering Failure Analysis*, vol. 15, pp. 208-219, 4// 2008.
- [29] R. L. Garris, "THE ADVANCED MANIPULATION OF AN ELECTROSPRAYED DIELECTRIC FLUID USING ELECTRIC FIELDS," Master of Science in Applied Energy and Electromechanical Systems, Engineering Technology, The University of North Carolina at Charlotte, The William States Lee College of Engineering, 2016.
- [30] D. Knouse, "Custom Reactor Quote," ed: Parr Instrument Company, 2016, p. 1.

- [31] C. North and B. Boiler Safety, "Uniform Boiler and Pressure Vessel Act of North Carolina, North Carolina General Statutes Chapter 95, Article 7A and administrative rules, North Carolina Administrative Code Title 13, Chapter 13," *Uniform Boiler and Pressure Vessel Act of North Carolina, North Carolina General Statutes Chapter 95, Article 7A and administrative rules, North Carolina Administrative Code Title 13, Chapter 13.*, vol. Chapter 95, p. 52, March 1, 2015 2015.
- [32] DEATSCHWERKS. (2016, September 24, 2016). *50lb (550cc) Fuel Injectors*. Available: <http://www.deatschwerks.com/products/fuel-injectors/bosch-ev14-universal-line/4-cylinders-ev14/long-60mm-ev14-4-cylinders/18u-00-0050-4-detail>
- [33] I. S. Schweitzer Engineering Laboratories. (2016, February 2, 2017). *Complete System for Control and Monitoring*. Available: https://cdn.selinc.com/assets/Literature/Product%20Literature/Data%20Sheets/2411_DS_20161205.pdf?v=20170111-083546
- [34] C. Constantinidis, "Custom Pressure Chamber," ed. Fabrication Associates, Inc., 2017.
- [35] B. Motorsport. (2016, December 2, 2016). *Injection Valve EV 14*. Available: http://www.bosch-motorsport.com/media/catalog_resources/Injection_Valve_EV_14_Datasheet_51_en_2775993867pdf.pdf

APPENDIX A: PARR INSTRUMENT COMPANY QUOTE

**QUOTATION**

No.: 6609271602

Page 1 of 1

University of North Carolina, Charlotte

Attn: Alzarrio Rolle

Phone:

Email: arolle1@uncc.edu

September 27, 2016

Shipping Terms: TBD	Ship: Prepaid & Add or Collect
Payment Terms: Net 30 Days with approved credit	Lead Time: 7 - 8 Weeks ARO

Please reference the quotation number on purchase orders and communication about this configuration.

Qty	Description	List Price (USD)
1	<p>N4666-T-SS-2000-ModifiedWindows</p> <p>Series N4666 Modified General Purpose Vessel with the following specifications:</p> <p>A) Two headed vessel</p> <p>B) Vessel MAWP Rating: 1900 psi at up to 225 °C</p> <p>C) Heads, cylinder, and internal wetted parts constructed of T316 Stainless Steel</p> <p>D) External valves and fittings constructed of Stainless Steel</p> <p>E) PTFE flat gasket split ring closures</p> <p>F) Top head to include:</p> <ol style="list-style-type: none"> 1) Gas inlet valve 2) Pressure gage, 0-2000 psi 3) Safety rupture disc of Inconel, rated to 2000 psi 4) Thermocouple, Type J 5) Gas release valve 6) 1/4"NPT ball valve with spray nozzle underneath head (Reference 912224) 7) 1/2"NPT Fused Silica window for added light source (Reference P09125-01) <p>G) Fixed cylinder with 6" ID and 36" inside depth (Reference 916109)</p> <p>H) Bottom Head with split ring closure and window housing. 4" viewing fused silica window.</p>	\$32,460.00
1	<p>N4972EE Fixed Vessel Floor Stand (Vessel to sit vertically.)</p> <p>A) Flexible heater included, 230 Volts</p>	\$10,600.00
1	<p>4838EE Temperature Controller with the following specifications:</p> <p>A) PID temperature control with ramp and soak programming</p> <p>B) 230V</p>	\$2,090.00
Spare Optional Parts:		
1	<p>655HC PTFE Spare Gasket (3 per package)</p>	\$42.00

Parr Instrument Company

Senior Technical Sales Manager

donna.knouse@parrinst.com

PRICES QUOTED ARE VALID FOR 60 DAYS211 Fifty-Third Street, Moline, IL 61265 | 800-872-7720 | 309-762-7716 | Fax: 309-762-9453 | parr@parrinst.com | www.parrinst.com

Figure 72: Initial Quote from Parr Instrument Company [30]

APPENDIX B: SOLIDWORKS DRAWINGS FOR PRESSURE CHAMBER DESIGN

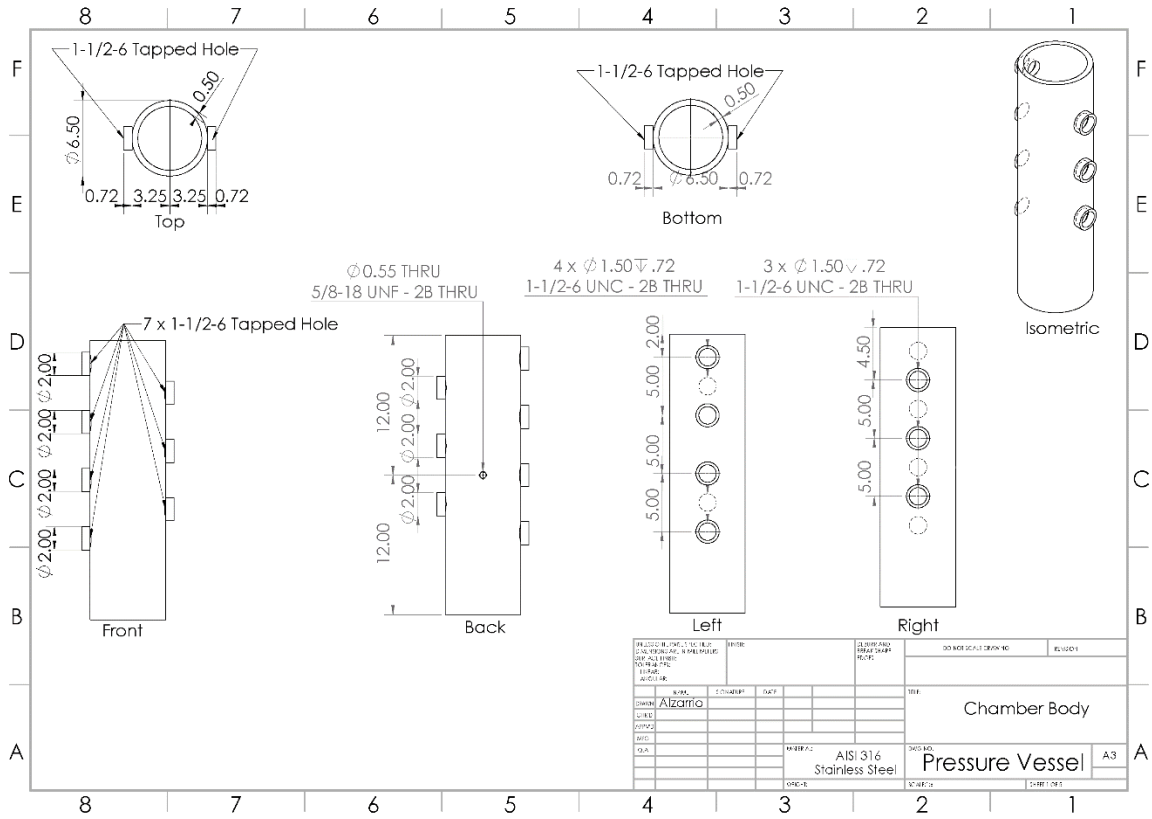


Figure 73: SolidWorks drawing for the body for the pressure chamber

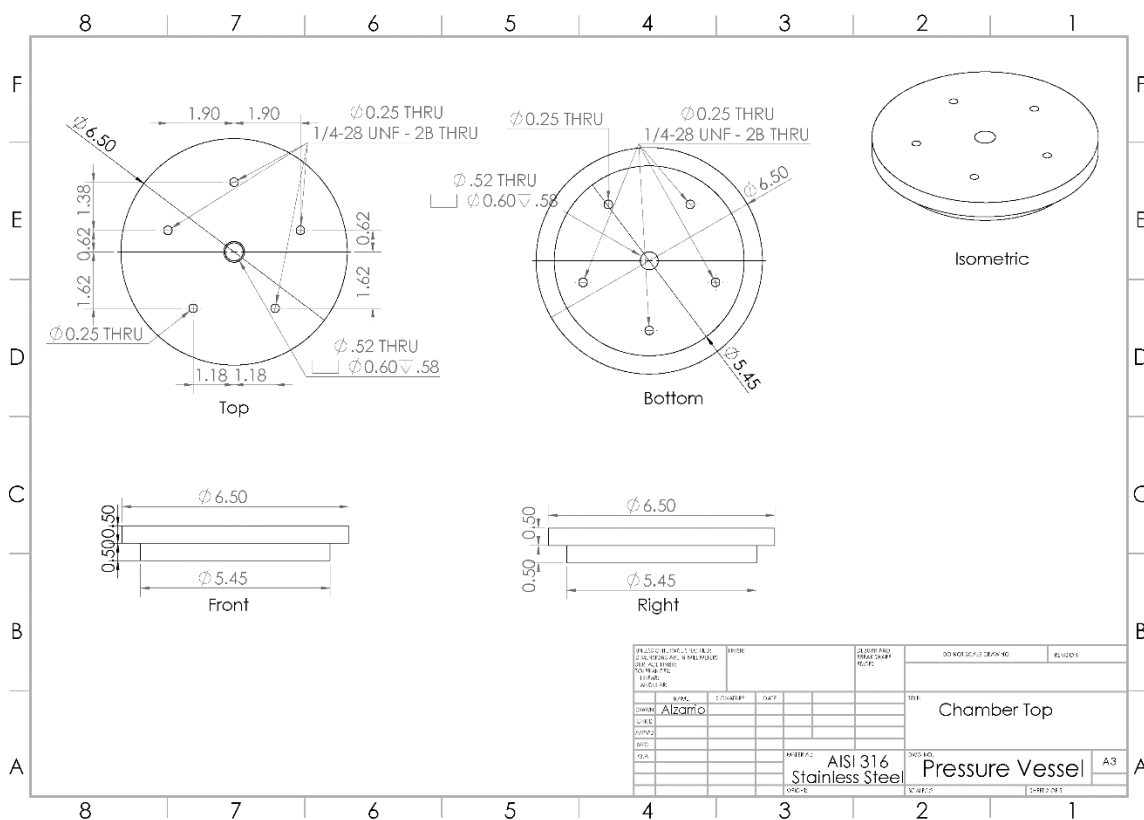


Figure 74: SolidWorks drawing for the top lid of the pressure chamber

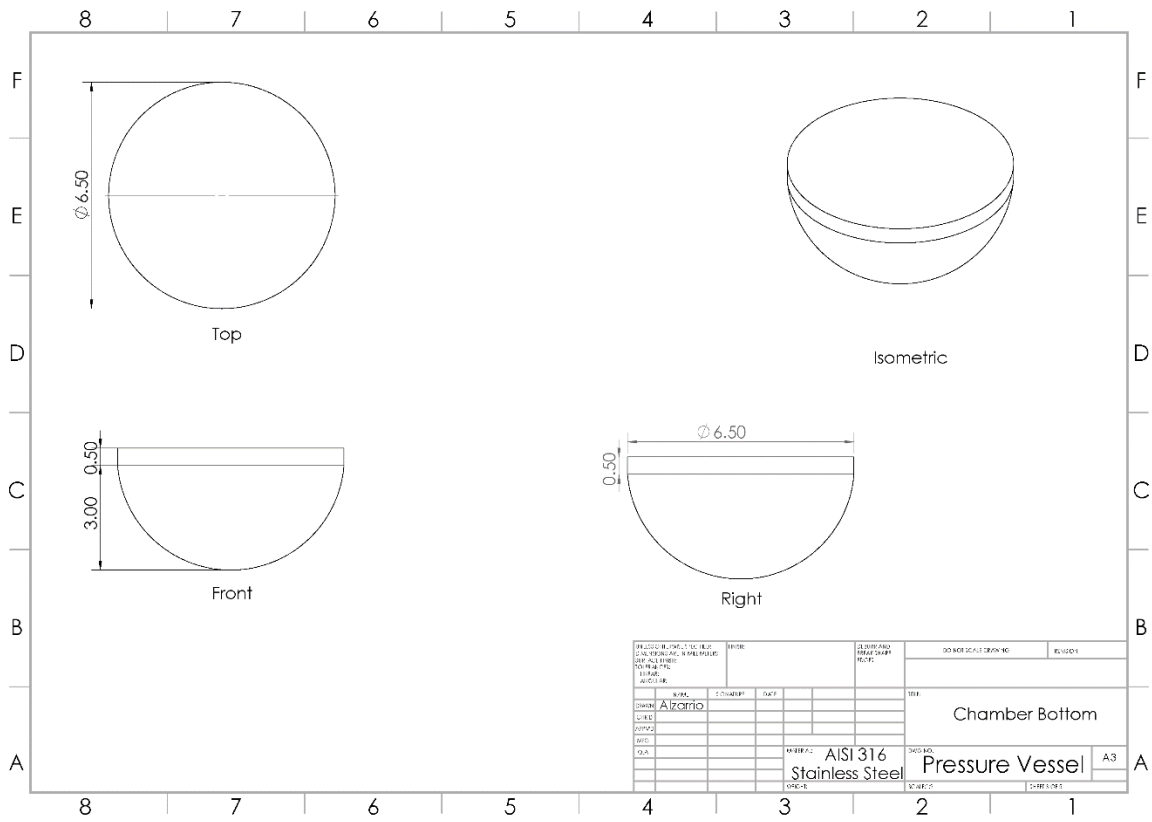


Figure 75: SolidWorks drawing for the bottom of the pressure chamber

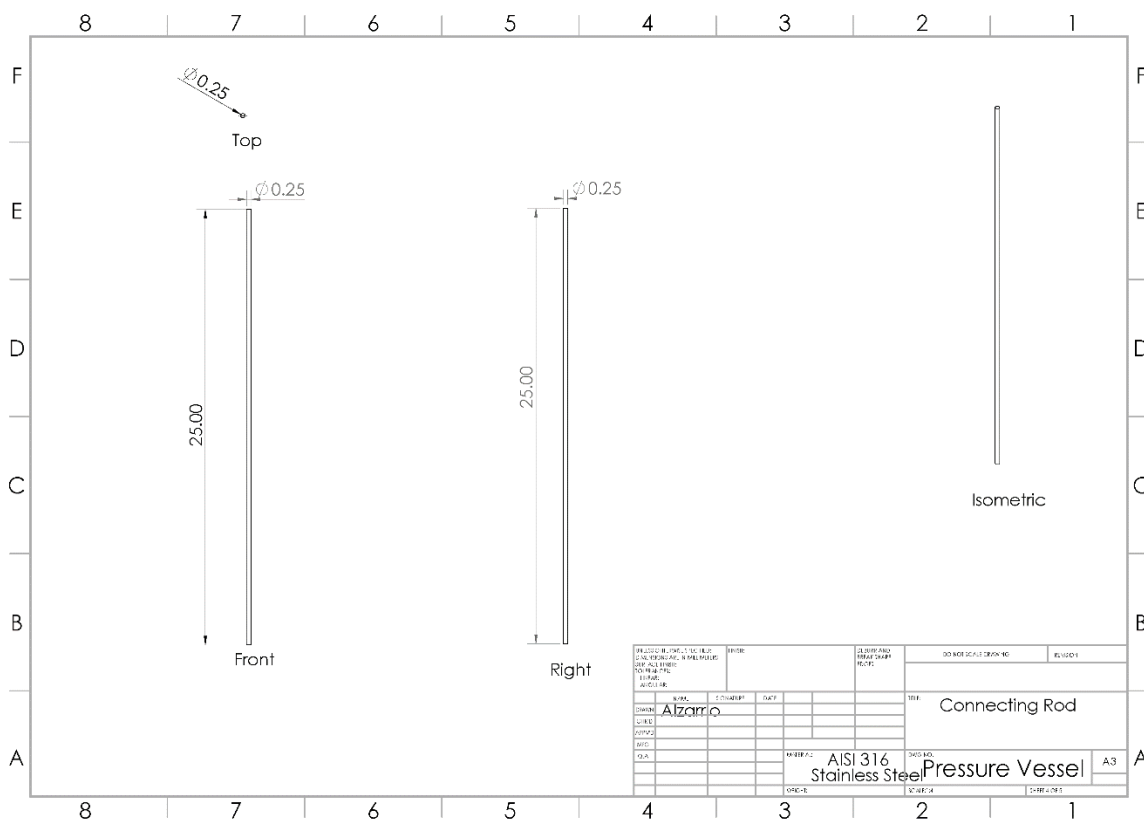


Figure 76: SolidWorks drawing for connecting rods of the pressure chamber

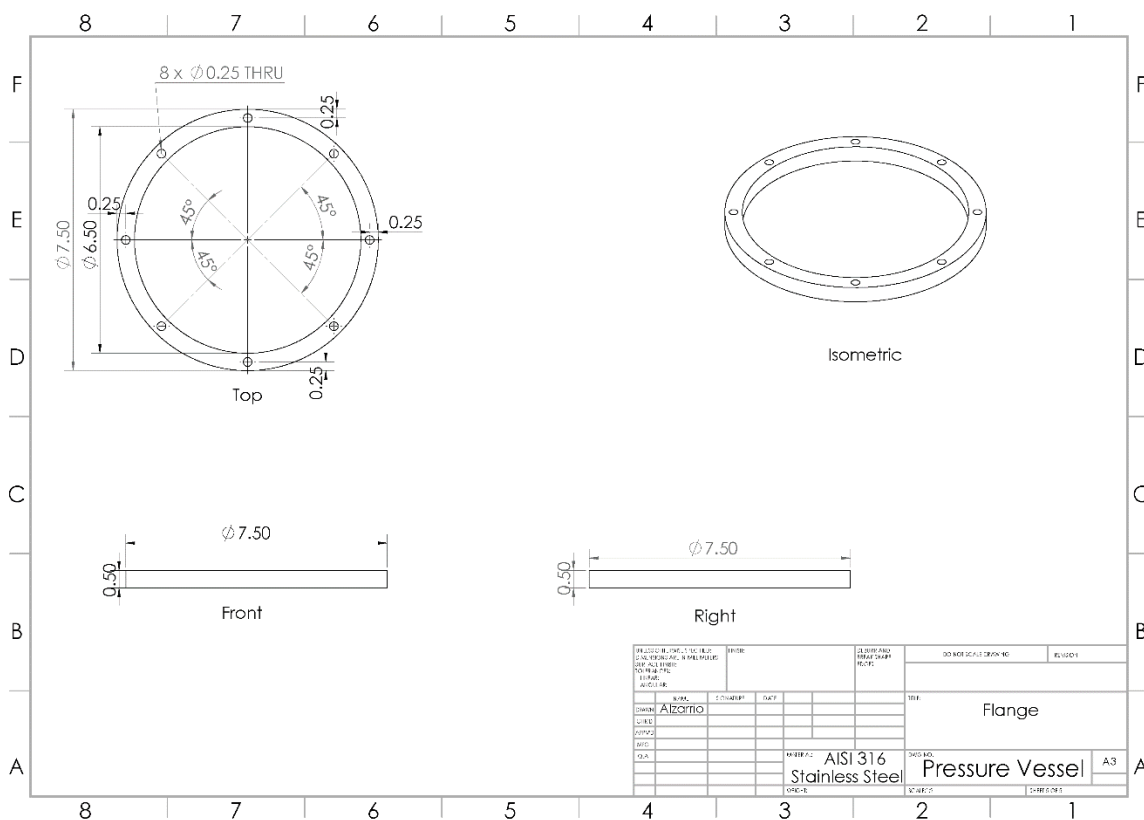


Figure 77: SolidWorks drawing for the flange of the pressure chamber

APPENDIX C: FUEL SYSTEM BILL OF MATERIALS

Table 5: List of Bill of Materials for the fuel injection system

Required Equipment	Price	Vendor
DeatschWerks 18U- 50lb (550cc) Fuel Injectors [4]	\$259.00	DeatschWerks
AEM Electronics Billet Adjustable Fuel Pressure Regulators 25-302BK	\$125.76	Amazon
Hypertech Power Pumps 4018	\$142.59	Amazon
Worm-Drive Clamp for Firm Hose and Tube 316 Stainless Steel, 5/16" Band Width, 7/32"- 5/8" Clamp ID Range	\$10.53	McMaster-Carr
5-Gallon Plastic Gasoline Can	\$33.43	MSC Industrial Direct
5 Gallons of 87-Octane	\$10.50	Gas Station
Brass Hose Barb with Straight Fitting Style, 1/2" Thread Size	\$12.96	GRAINGER
Earl's 981668 Blue Anodized Aluminum -6AN Male to 1/2" NPT Straight Adapter	\$9.18	Amazon
Earl's 981668 Blue Anodized Aluminum -6AN Male to 1/2" NPT Straight Adapter	\$9.18	Amazon
Extreme-Pressure 316 Stainless Steel Pipe Fitting Straight Connector with Hex Body 1/8 NPTF Female	\$12.23	McMaster-Carr
Brass Cap, FNPT, 1/2" Pipe Size - Pipe Fitting	\$39.95	GRAINGER
Derale 98204 -6AN male x 3/8" AN Hose Barb Fitting	\$11.02	Amazon
Derale 98204 -6AN male x 3/8" AN Hose Barb Fitting	\$11.02	Amazon
Stainless Steel Gauge Stainless Steel Case, Liquid, 1-1/2" Dial, 1/8 Bottom Connection	\$87.62	McMaster-Carr
Smooth-Flow Tygon Tubing for Food & Beverage 1/2" ID, 3/4" OD, 1-1/4" Bend Radius 5624K53 (20 Feet)	\$153.60	McMaster-Carr
Smooth-Flow Tygon Tubing for Food & Beverage 3/8" ID, 5/8" OD 5624K52 (25 Feet)	\$158.25	McMaster-Carr
Total	\$1086.82	

APPENDIX D: DIMENSIONED DRAWING FOR EV 14 LONG FUEL INJECTOR

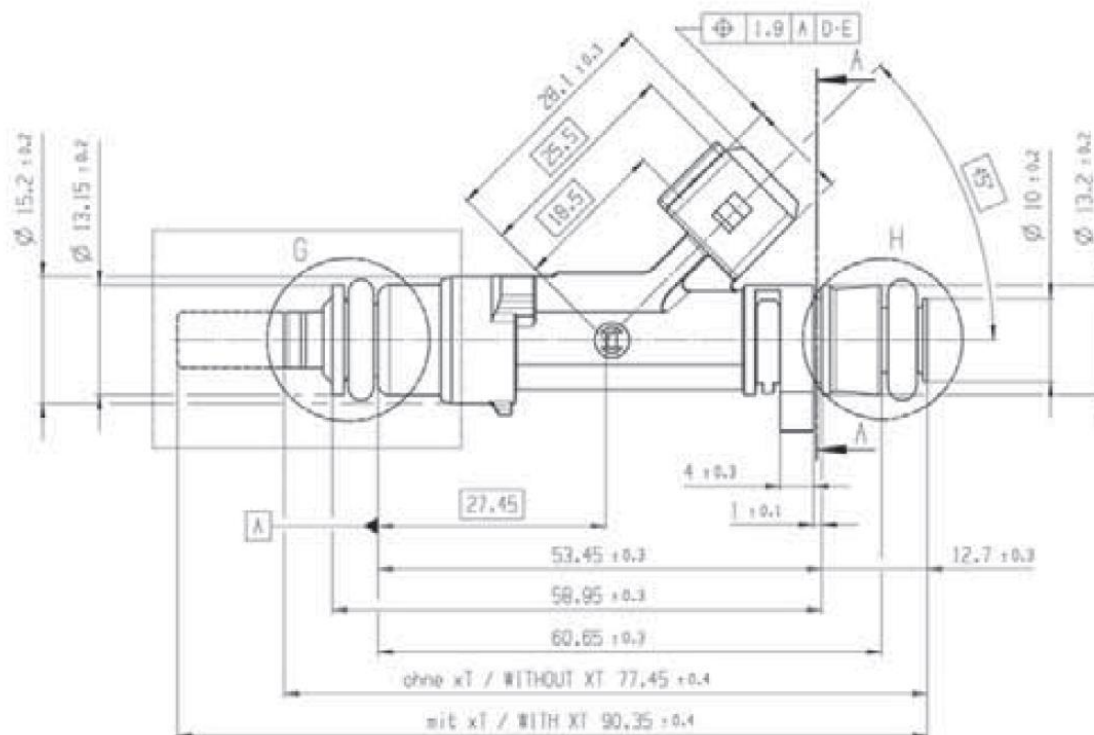
**EV 14 Long**

Figure 78: Dimensions of EV 14 Long fuel injector from Bosch Engineering [35]

APPENDIX E: FINANCIAL QUOTE FROM FABRICATION ASSOCIATES INC.



Fabrication Associates, Inc.
 7950 Pence Rd
 Charlotte, NC 28215
 United States of America

Ph: (704) 535-8050

Fax: (704) 531-6145

Quote

Number: 2964 Date: 28-Feb-17

To

University of North Carolina Charlotte
 United States of America

Quote To

Alzarrio Rolle
 University of North Carolina Charlotte
 United States of America

Terms		Ship Via		Salesperson
Quantity	Description	Unit Price	Amount	
	Price does NOT include sales tax.			
1	Line: 001 Expiration Date: 28-Mar-17 Part: FUEL INJECTOR TESTING CHAMBER Rev: ea 6" NPS x 24" OAH, T-316/316L construction, per your drawings, description and comments, and as follows: Vessel bottom head will be 6" Sch. 80S pipe cap, SA-403 WP 316/316L. Vessel shell will be 6" Sch. 80S pipe, SA-312 TP 316/316L. Vessel top head will be flat, approximately 1.25" thick SA-240 316/316L plate, attached to a body flange with (8) 0.5"-unc studs with nuts. Top head will be sealed by means of an 1/8" O-Ring installed into the body flange. Top head will have (6) drilled and tapped tapered pipe threaded holes of various sizes for attachment of fuel injector and instrumentation. Recommend using reducing threaded bushings for connections that will be accessed regularly in order to protect threads in top cover. Vessel shell will have (7) 1.5" class 3000 threaded half couplings to accommodate threaded sight-glasses. Sight-glasses purchased and installed by others. Vessel bottom head will have (1) 0.5" class 3000 threaded coupling with plug for draining. Vessel will have one side mounting bracket perpendicular to centerline of sight glasses. Vessel will be designed, fabricated and tested for 450 psig @ 300° F. A pressure relief device may be required for safe operation of testing chamber, purchased and installed by others.	\$4,600.00	\$4,600.00	
	Drawings: 2 weeks after receipt of order Material: 2 weeks after release to purchase Delivery: 2 weeks after receipt of approved drawings and material Terms: 20% with purchase order 20% upon receipt of major material Balance upon completion. All invoices net 30 days.	Total:	\$4,600.00	

Figure 79: Fabrication Associates Inc. financial quote for custom pressure chamber [34]

APPENDIX F: CERTIFIED DRAWING OF THE PRESSURE CHAMBER

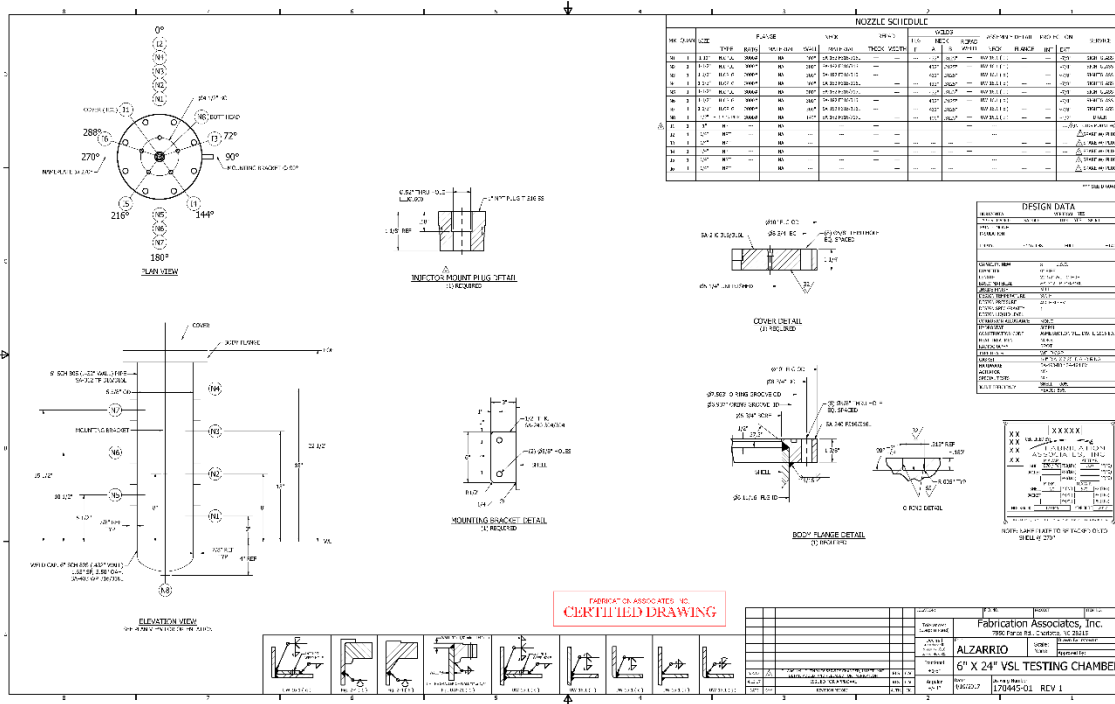


Figure 80: Certified Drawing from FAB Inc. of constructed Pressure Vessel [34]

APPENDIX G: RAW MASS DATA FOR SPRAYING EXPERIMENTS IN GRAMS

Table 6: Spray Mass for 40, 50 and 60 psi

Spray Number	Spray at 40 psi	Spray at 50 psi	Spray at 60 psi
	Mass in grams	Mass in grams	Mass in grams
1	0.04	0.06	0.06
2	0.08	0.06	0.11
3	0.08	0.08	0.13
4	0.11	0.11	0.19
5	0.13	0.15	0.23
6	0.18	0.19	0.27
7	0.18	0.23	0.30
8	0.23	0.28	0.34
9	0.26	0.32	0.39
10	0.30	0.36	0.42
11	0.35	0.38	0.45
12	0.39	0.44	0.46
13	0.44	0.46	0.52
14	0.47	0.50	0.56
15	0.50	0.52	0.58
16	0.54	0.56	0.61
17	0.56	0.61	0.64
18	0.61	0.66	0.68
19	0.65	0.65	0.71
20	0.68	0.69	0.75

APPENDIX H: CALCULATED VOLUME DATA FOR SPRAYING EXPERIMENTS
IN KILOGRAM PER CUBIC METER

Table 7: Calculated Spray Volume for 40, 50 and 60 psi

Spray Number	Spray at 40 psi Volume in [m ³]	Spray at 50 psi Volume in [m ³]	Spray at 60 psi Volume in [m ³]
1	5.56E-08	8.34E-08	8.34E-08
2	1.11E-07	8.34E-08	1.53E-07
3	1.11E-07	1.11E-07	1.81E-07
4	1.53E-07	1.53E-07	2.64E-07
5	1.81E-07	2.08E-07	3.20E-07
6	2.50E-07	2.64E-07	3.75E-07
7	2.50E-07	3.20E-07	4.17E-07
8	3.20E-07	3.89E-07	4.72E-07
9	3.61E-07	4.45E-07	5.42E-07
10	4.17E-07	5.00E-07	5.84E-07
11	4.86E-07	5.28E-07	6.25E-07
12	5.42E-07	6.11E-07	6.39E-07
13	6.11E-07	6.39E-07	7.23E-07
14	6.53E-07	6.95E-07	7.78E-07
15	6.95E-07	7.23E-07	8.06E-07
16	7.50E-07	7.78E-07	8.48E-07
17	7.78E-07	8.48E-07	8.89E-07
18	8.48E-07	9.17E-07	9.45E-07
19	9.03E-07	9.03E-07	9.87E-07
20	9.45E-07	9.59E-07	1.04E-06

APPENDIX I: RAW ELECTRICAL CHARGE DATA FOR EACH SPRAY IN [nC]

Table 8: Electric Charge Values for 40, 50 and 60 psi

Spray Number	Spray at 40 psi Charge Density [nC]	Spray at 50 psi Charge Density [nC]	Spray at 60 psi Charge Density [nC]
1	0.066	0.045	0.046
2	0.083	0.038	0.046
3	0.066	0.045	0.054
4	0.094	0.046	0.048
5	0.050	0.041	0.046
6	0.047	0.043	0.055
7	0.033	0.038	0.053
8	0.043	0.040	0.056
9	0.030	0.045	0.055
10	0.033	0.050	0.049
11	0.034	0.043	0.057
12	0.027	0.049	0.057
13	0.032	0.048	0.059
14	0.029	0.051	0.048
15	0.029	0.042	0.054
16	0.033	0.045	0.053
17	0.028	0.047	0.052
18	0.035	0.043	0.050
19	0.038	0.043	0.050
20	0.030	0.054	0.049

APPENDIX J: COMSOL MULTIPHYSICS PARAMETERS FOR MODEL
DISTRIBUTIONS AND PARTICLE TRAJECTIONS

Table 9: COMSOL Multiphysics model parameter definitions

Name	Expression	Value	Description
D	10[cm]	0.1 m	cylinder diameter
H	20[cm]	0.2 m	cylinder height
eta_gas	0.0258[N/m]	0.0258 N/m	surface tension of gasoline
eps_0	8.85e-12[F/m]	8.85E-12 F/m	dielectric permittivity of air
q_electron	1.6e-19[C]	1.6E-19 C	charge of an electron
gas_density	750[kg/m^3]	750 kg/m ³	density of gasoline
dyn_viscosity_air	43.7e-6[Pa*s]	4.37E-5 Pa·s	dynamic viscosity of air
T_cyl	20[degC]	293.15 K	temperature in cylinder
p_cyl	40[psi]	2.7579E5 Pa	pressure in cylinder
p_speed	200[m/s]	200 m/s	initial droplet velocity
V_el	1e4	10000	potential applied to cylinder
t_lim	50[ms]	0.05 s	length of the injection process
p_number	2e1	20	number of released droplets
Inj_volume	0.94[ml]	9.4E-7 m ³	volume of injected fuel
psd	10[um]	1E-5 m	droplet mean diameter
drop_volume	$4/3 \cdot \pi \cdot (\text{psd}/2)^3$	5.236E-16 m ³	droplet mean volume
p_number_calc	Inj_volume/drop_volume	1.7953E9	alt. number of droplets
Voltage	1e4[V]	10000 V	applied voltage
t_injection	8[ms]	0.008 s	injection time
Diff_pressure	29[psi]	1.9995E5 Pa	injector pressure differential
Flow	5.7[g/s]	0.0057 kg/s	fuel flow for Diff_pressure

APPENDIX K: PRESSURE CHAMBER AND RELATED EQUIPMENT BILL OF MATERIALS

Table 10: List of Remaining Bill of Materials for the Pressure Chamber

Required Equipment	Quantity	Vendor	Price
Threaded Pressure-Relief Disc 316 Stainless Steel Disc, 700 PSI Burst Pressure 1/4" NPT Male	2	McMaster-Carr	\$269.50
Leak-Resistant Liquid-Filled Gauge	1	McMaster-Carr	\$131.71
LDI Industries - 1-7/16 Inch Sight Diameter, 1-1/2 Inch Thread, 1.22 Inch Long, High Pressure Fused Pipe Thread and Open View, Sight Glass and Flow Sight – 2 Head, 750 Max psi, 1-1/2 to 11-1/2	7	MSC Industrial Direct	\$264.11
Brass Air Fill Valve Straight, 1/4 NPT, 1-5/16" Overall Length	2	McMaster-Carr	\$7.88
Total	12		\$673.20